Excited-state dynamics for spin-flip process in purely organic charge-transfer type molecules

野田, 大貴

2019

Doctor thesis

Excited-state dynamics for spin-flip process in purely organic charge-transfer type molecules

Hiroki Noda

Department of Chemistry and Biochemistry
Graduate School of Engineering
Kyushu University

Contents

Chapter 1

Introduction

1-1. Background and motivation

1-1-1. Spin-flip process in purely aromatic molecules

When purely aromatic molecules are excited by optically, they have possibilities to form two excited spin-states, *i.e.*, the singlet excited-state (S) and the triplet excited-state (T). Since an electron transition process between pure S and T states needs a spin-flip process, the electron transition process is a strictly spin-forbidden because, based on the quantum chemical theory, the overlap integral of the wavefunction between pure S and T states vanishes. However, as a matter of fact, spin-flip processes such as intersystem crossing (ISC) are widely observed even in purely aromatic molecules and play critical role for chemical reactions (*1*), electroluminescence (EL) (*2-4*), room-temperature phosphorescence (RTP) (*5*), bio-imaging (*6,7*), chemical compasses (*8*), photon up-conversion systems (*9*), photodynamic therapy (*10*) and singlet fission (*11*) because spin-flip process are indispensable for utilizing triplet excitons.

According to perturbation theory, the observation of ISC in aromatic molecules can be ascribed to the fact that the spin forbidden process is 'partially' allowed as a result of the mixing of wavefunctions between the pure S and T states. If a zero-order wavefunction (ψ_0) is a reasonable approximation to the true wavefunction (ψ), perturbation theory can be employed to "distort" ψ_0 in the direction of ψ. In aromatic molecules, the internal conversion from a higher excited state to the lowest S (S_1) or T (T_1) states is much faster than spin-flip processes. Therefore, we can assume that ψ_0 corresponds to S_1 or T_1 and the observed excited-states in real aromatic molecules possess the mixed wavefunction of pure S_1 and pure T_1 states. Here, the wavefunction of the real T_1 state ($\psi_{T_1}{}'$) can be described by the linear combination of the wavefunctions of pure S and pure T_1 as below (*12*)

$$\psi_{T_1}{}' = \psi_{T_1} + \lambda\psi_{S_1} \quad (1)$$

where ψ_S and ψ_T is the wavefunction of pure S and T states, respectively, and λ is the first-order mixing coefficient which can be descried as below,

$$\lambda \approx \frac{H_{SOC}}{|\Delta E_{S-T}|} \quad (2)$$

where $\Delta E_{S\text{-}T}$ is the energy splitting between the S and T states, and H_{SOC} is the spin-orbit coupling

(SOC) element value.

According to the equation (2), it can be expected that the mixing between S and T states increases in proportion to the magnitude of the H_{SOC} and inversely proportion to $\Delta E_{S\text{-}T}$. Indeed, the magnitude of the H_{SOC} is an essential factor. Generally, H_{SOC} is proportional to the fourth power of nuclear charge (Z) because a magnetic field produced by the atom should increase with an increasing of atomic number. Thus, H_{SOC} of organic molecules increases by utilizing the atoms with large atomic number. For example, the forward ISC (S $\rightarrow$ T) rate (k_{ISC}) of 1-iodonaphthalene is approximately 10^{10} s^{-1}, which is four order magnitude larger than that of an unsubstituted naphthalene, indicating that the k_{ISC} is accelerated by the heavy atom effect (*13*). In contrast, for aromatic compounds that contain no heavy atoms such as halogens, the spin-flip rate constant is generally very small. For example, pyrene has k_{ISC} of about 10^6 s^{-1} in benzene solution (*14*). However, k_{ISC} of benzophenone reaches the order of 10^{11} s^{-1} in cis- and trans-piperylene solution, even though benzophenone contains no heavy atoms (*15*). This large difference of k_{ISC} can be understood by El-Sayed rule (*16*). As an example, the spin-flip processes of carbonyl group can be illustrated as shown in **Fig. 1-1**. In this picture, the ISC process from ^{1}(n, π*) to ^{3}(π, π*) is a spin-allowed transition because the total angular momentum is preserved by the electron transition between p_x and p_y orbitals with the change of spin orientation on the oxygen atom. This electron transition causes magnetic momentum originated from orbital angular momentum (μ_L). In addition, now we focus on the transition from S to T, so magnetic momentum originated from spin (μ_S) is interacted with the generated μ_L, leading to the large H_{SOC}. However, in case of the transition between ^{1}(n, π*) to ^{3}(n, π*), since the electron transition occurs from n (↑) to n (↓), *i.e.*, $p_y \rightarrow p_y$, no μ_L is generated. Thus, this transition does not

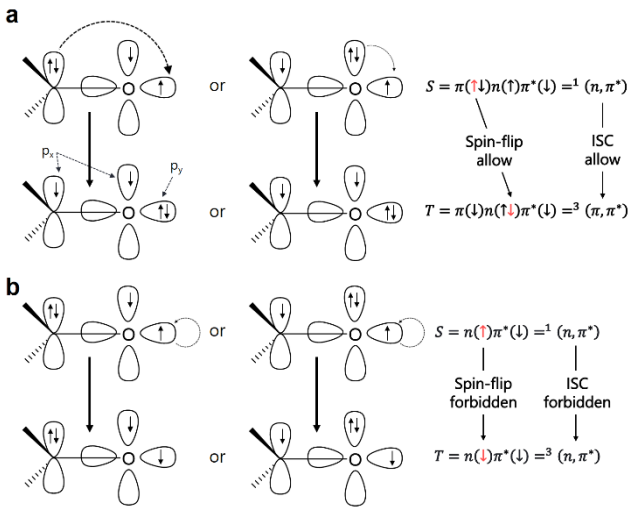

Figure 1-1 Illustration of ISC process of carbonyl group. (**a**) Spin-allowed transition from ^{1}(n, π*) to ^{3}(π, π*). (**b**) Spin-forbidden transition from ^{1}(n, π*) to ^{3}(n, π*)

satisfy the law of conservation of angular momentum, resulting in the vanishing H_{SOC}. This spin selection rule is well known as El-Sayed rule, and the spin-flip process efficiently proceeds when the nature of initial and final states are largely different.

1-1-2. Room temperature phosphorescence

The radiative decay process from the T_1 state is usually forbidden, but some purely aromatic molecules can show RTP by suppression of a nonradiative decay process from the T_1 state. A number of such cases have been reported in a host-guest system and inclusion complexes (*17,18*). Since such a RTP system show long duration lifetime of emission (second order scale), *i.e.*, long-lived RTP (LL-RTP), LL-RTP system is expected to be applied to glow-in-the-dark paints for watches, indicators, emergency lights and afterglow safety lamps (*5*). However, the radiative decay from the T_1 state is strictly forbidden because of the small H_{SOC}, resulted in significantly low PLQY.

On the other hand, according to equation (2), since the utilization of heavy atom effect increases H_{SOC}, it is possible to observe RTP efficiently, while it is usually difficult to observe in purely aromatic molecules (**Fig. 1-2a**). As an example, in case of an organometallic complex containing iridium (Ir, Z = 77), the radiative decay rate from T_1 (k_r^T) is greatly accelerated by its heavy atom effect. k_r^T of tri(2-phenylpryidinato)iridium(III) ($Ir(ppy)_3$), a representative RTP molecule, is 10^4 times larger than that of conventional aromatic molecule, pyrene (*19*). The photoluminescence (PL) quantum yield (PLQY) of $Ir(ppy)_3$ reaches nearly 100%, indicating that the ISC yield also reaches 100% by its heavy atom effect. Thus, when we use these organometallic complexes as an emitter in organic light-emitting diodes (OLEDs), the theoretical maximum value of an internal EL quantum efficiency (IQE) can be achieved (*2,20*). This is because 75% of electrically generated excitons are directly formed in the T state after carrier recombination events and not only the $T_1 \rightarrow$ ground state (S_0) transition but also the indirect exciton harvesting through the forward ISC of the S_1 state $\rightarrow T_1$ becomes spin allowed transition due to the heavy atom effect.

1-1-3. Thermally Activated Delayed Fluorescence

According to the equation (2), it is also possible to induce an intense mixing between S and T states by the vanishing $\Delta E_{S\text{-}T}$ even when a molecule has a small H_{SOC}. When $\Delta E_{S1\text{-}T1}$ decreases until the λ becomes sufficiently large, the both forward and reverse ISC (T→S) processes between S_1 and T_1 becomes allowed transition because the electron transition from T_1 to S_0 is still slow. In this situation, the triplet excitons can be harvested as delayed fluorescence (DF) from S_1 during multiple forward/reverse ISC cycles (**Fig. 1-2b**). Such fluorescence phenomenon is called as *E*-type DF or thermally activated DF (TADF) (*21,22*).

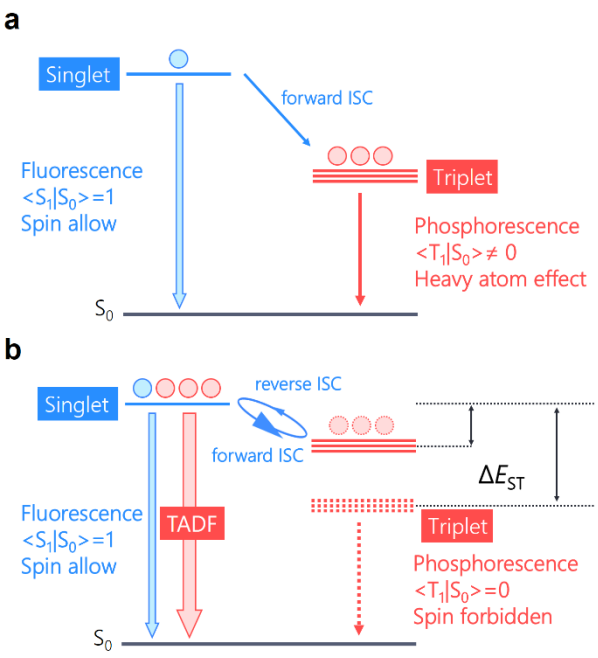

Figure 1-2 Emission mechanism of fluorescence and phosphorescence (**a**) and TADF (**b**)

The discovery of TADF dates back to 1930. S. Boudin observed a weak long-lived luminescence from 0.005% w/v Eosin Y (**Fig. 1-3**) in glycerol solution at room temperature (*23*), and she concluded that the emission was corresponding to the phosphorescence of Eosin Y because the emission lifetime was long decay time of about 1 ms. About ten years later, G. N. Lewis et al. tried to reproduce S. Boudin's work, and they measured the emission of fluorescein in boric acid glass (*24*). They observed an increase in emission intensity that corresponding to the fluorescence of fluorescein with the expense of phosphorescence intensity during an increasing temperature from -40 °C to 20 °C. This thermally enhanced emission can be attributed to the DF from the S_1 state populated by thermal upconversion from the T state. In 1961, Parker et al. re-examined Boudin's work by measuring its emission properties in glycerol and ethanol in various temperature, and he observed another emission in the longer wavelength attributed to the real phosphorescence of Eosin Y (*21,22*). This results clearly means that a weak long-lived luminescence from Eosin Y is not phosphorescence but TADF. Thus, since TADF properties first discovered in Eosin Y, TADF is called *E*-type DF. After

investigation of TADF for Eosin Y, several types of TADF molecules have been reported (**Fig. 1-3**); benzophenone and its derivatives with the n-π* excited-state in carbon tetrachloride (*25*), Cu(I) $(dmphen)_2^+$, (dmphen: dimethylphenanthridine), with metal to ligand charge transfer (MLCT) excited-state in dichloromethane (*26,27*), C70 (*28*) and donor-acceptor CT type molecules (*29*). The detail of TADF mechanisms discussed in **section 1-1-5**.

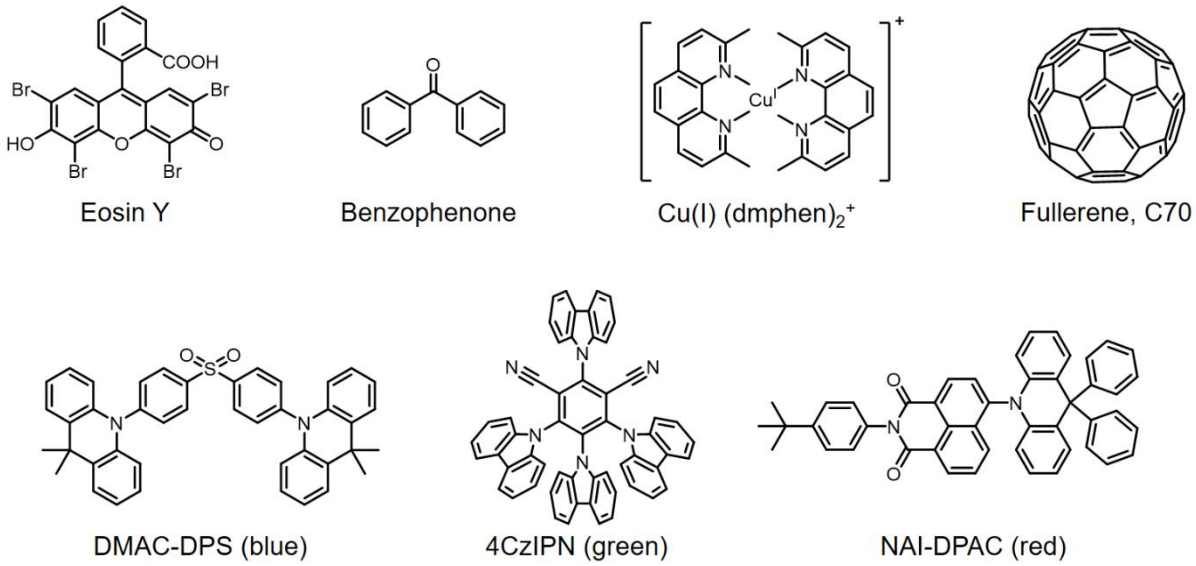

Figure 1-3 Molecular structures of typical TADF molecules

1-1-4. Organic light-emitting diodes

The organic compounds exhibiting RTP or TADF are useful as an OLEDs' emitter. **Figure 1-4** illustrates the basic structure of an OLED containing three organic layers sandwiched between a cathode and an anode under electrical operation. Generally, organic layers are formed of several materials with different functions such as a hole-transport layer (HTL), an emitting layer (EML) and an electron-

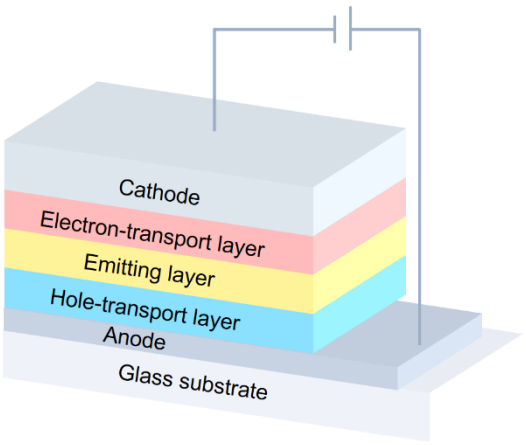

Figure 1-4 Schematic illustration of an OLED structure.

transport layer (ETL). When electric field is applied to two electrodes, holes and electrons injected into the HTL and the ETL from the anode and the cathode, respectively, and repeat the oxidation-reduction reaction between adjacent molecules by the electric field gradient as a driving force and move through each transport layer. The holes and electrons injected from each electrode recombine in the EML to form a hole-electron pair (exciton). In this case, it is considered that the electron configuration of the generated one-electron excited-state takes four states depending on the intrinsic state of the electron spin as shown below.

$$\psi_{1,2} = \frac{1}{2}[\phi_1(1)\cdot\phi_2(2) + \phi_1(2)\cdot\phi_2(1)]\cdot[\alpha(1)\cdot\beta(2) - \alpha(2)\cdot\beta(1)] \quad (3)$$

$$\psi_{1,2} = \frac{1}{\sqrt{2}}[\phi_1(1)\cdot\phi_2(2) - \phi_1(2)\cdot\phi_2(1)]\cdot[\alpha(1)\cdot\alpha(2)] \quad (4)$$

$$\psi_{1,2} = \frac{1}{\sqrt{2}}[\phi_1(1)\cdot\phi_2(2) - \phi_1(2)\cdot\phi_2(1)]\cdot[\alpha(1)\cdot\beta(2) + \alpha(2)\cdot\beta(1)] \quad (5)$$

$$\psi_{1,2} = \frac{1}{\sqrt{2}}[\phi_1(1)\cdot\phi_2(2) - \phi_1(2)\cdot\phi_2(1)]\cdot[\beta(1)\cdot\beta(2)] \quad (6)$$

where ϕ_1 and ϕ_2 are wavefunction of electron 1 or 2 and α (upward) and β (downward) are spin function. The energy of a molecule is determined by the orbital motion of electrons. In other words, the three states of formula (4) - (6) where the wavefunctions of the orbital part are the same have the same energy and are referred to as T states because they degenerate triple in terms of energy. On the other hand, the state of formula (3) is called as a S state. When the injected holes and electrons have spins of α and β, respectively, 25 % of singlets and 75% of triplets are statistically formed electrically (*30,31*). Therefore, the harvesting the all electrically generated triplet excitons is crucial to achieve an ideal IQE in OLEDs.

As mentioned above, phosphorescence-based OLEDs (phos-OLEDs) can realize nearly 100% IQE but since it contains rare metal elements such as Pt and Ir, material costs are generally high and there are major problems in resource strategy such as regional ubiquity of resources. Moreover, phos-OLEDs typically suffer from rapid decrease of external EL quantum efficiency (EQE) with increasing an injected current density, *i.e.*, EL efficiency rolloff, because of the influence of triplet-triplet annihilation (TTA) and singlet-triplet annihilation (STA) processes (*32,33*). Furthermore, it is noted that the device operational stability in blue phos-OLEDs is still insufficient for display and lighting applications (*34,35*).

Adachi's group established the fundamental molecular design for an efficient TADF process and applied them to OLEDs (*4*,*36*). Their molecular design mainly focused on minimizing the $\Delta E_{S1\text{-}T1}$ to induce an efficient reverse ISC in purely organic aromatic systems. $\Delta E_{S1\text{-}T1}$ can be described by formula (7),

$$\Delta E_{S1-T1} = 2\iint \phi_{HOMO}(1)\phi_{LUMO}(2)\frac{1}{r_{12}}\phi_{HOMO}(2)\phi_{LUMO}(1)d\tau_1\tau_2 \quad (7)$$

where ϕ_{HOMO} and ϕ_{LUMO} is the wavefunction of the highest occupied molecular orbital (HOMO) and the lowest unoccupied molecular orbital (LUMO), respectively and r_{12} is the distance between the electrons 1 and 2. According to the equation (7), a small $\Delta E_{S1\text{-}T1}$ can be realized when there is small spatial overlap between the HOMO and LUMO (*4*).

To realize an efficient TADF, a small $\Delta E_{S1\text{-}T1}$ is one of the critical factors. The spatially separation of HOMO and LUMO is easily provided by intermolecular charge-transfer (CT) excited-state. The CT-state then has a chance to form an exciplex ($[D]^{\delta+}$:$[A]^{\delta-}$) state between electron donating (D) and accepting (A) molecules under photo- and electrical excitations (*37,38*). Since the exciplex emission occurs as a result of electron transition from the LUMO of $[D]^{\delta+}$:$[A]^{\delta-}$ to the HOMO of $[D]^{\delta+}$:$[A]^{\delta-}$ and the HOMO and LUMO are strongly localized on D and A molecules, respectively, the electron-hole separation distance should be corresponds to the distance D and A molecules, *i.e.*, almost zero overlap between HOMO and LUMO, leading to remarkably small $\Delta E_{S1\text{-}T1}$. Therefore, the utilization of exciplex states is one of the promising ways to realize efficient TADF property. Goushi et al. firstly reported TADF-based OLEDs (TADF-OLEDs) with exciplex as an emissive state by the combination of 4,4',4''-tris[phenyl(m-tolyl)amino]triphenylamine (*m*-MTDATA) as a D molecule and tris-[3-(3-pyridyl)mesityl]borane (3TPYMB) as an A molecule (*39*). After this report, exciplexes based OLEDs with a wide variety of D and A molecules have been reported (*40*). However, the PLQY of exciplex emission is generally low. This is because almost zero overlap between HOMO and LUMO reduce not only $\Delta E_{S1\text{-}T1}$ but also oscillator strength (*f*), which is an important factor related to the transition probability between S_0 to S_1 (the intensity of absorption and emission) as shown in equation (8).

$$f \propto \mu_{10} = \int \rho_{10}(x)(-ex)dx \quad (8)$$

where μ_{10} is transition dipole moment, ρ_{10} is the overlap integral between S_0 and excited-state (basically HOMO and LUMO). Since the overlap between HOMO and LUMO is spatially separated in each molecule, the radiative decay process from a S_1 state in exciplexes should not be efficient, leading to the deactivation of the exciton by nonradiative decay processes from S_1 or T_1 during multiple forward/reverse ISC cycles.

In contrast to intermolecular TADF system, the intramolecular TADF process is more promising and the theoretical maximum value of IQE has been realized in blue (*41*), red (*42*) and green (*4*) EL, leading to full-color display and lighting applications (**Fig. 1-3**). The basic molecular design to demonstrate intramolecular TADF materials is the formation of an intramolecular CT-state by the introduction of D and A units, which have a high triplet localized excited (LE) state (^{3}LE) energy than these of the CT excited-states. An efficient HOMO-LUMO separation can be obtained by a molecule with a large dihedral angle between each unit. In an intramolecular TADF system, by the precise control of dihedral angle and D and A abilities, both $\Delta E_{S1\text{-}T1}$ and f can be finely tuned (*43,44*). Since molecules exhibiting TADF can be designed without using expensive rare-metal elements such as Ir, the development of intramolecular TADF system is becoming main stream for the development of OLEDs' emitters (*29*). However, since TADF-OLEDs utilize triplet excitons, there are several crucial problems that should be overcame. The accumulation of triplet excitons, as in case of phos-OLEDs, induces an EL efficiency rolloff and a short device operational stability.

1-1-5. Forward and reverse ISC rate in TADF molecules

As described above, an organic molecule exhibiting TADF is one of the promising materials in order to utilize the triplet excitons as light energy and expected to contribute to the development of a wide variety of optoelectronic applications. Since, in a TADF process, the triplet excitons can be harvested as DF from S_1 during multiple forward/reverse ISC cycles, the management of both a k_{ISC} and a reverse ISC rate (k_{RISC}) is crucial. For example, very fast k_{RISC} promises the improvement of

OLEDs performance because the reduction of triplets density in the device during electrical excitation prevents detrimental exciton annihilation and/or chemical reactions, resulting in the suppression of exciton quenching and long operational lifetime (*45,46*). On the other hand, a controlling of k_{RISC} for a slow reverse ISC can be applied to different applications. For examples, since the long lifetime of a T state is suitable for spatiotemporal imaging of oxygen distribution with high sensitivity (*47*) because a triplet exciton is efficiently quenched by a presence of oxygen (*48*), TADF molecules with small k_{RISC} should be one of the desirable materials in the field of bio-imaging at the cellular and tissue level. In addition, to demonstrate a lasing action and/or an amplified spontaneous emission (ASE) optically from organic gain medias, an organic molecule which has a limited k_{ISC} is desirable because the suppression of the forward ISC process can lead the utilization of all of the excitons as emission from a S_1 state. In contrast, for a photon upconversion system, since a long exciton lifetime of triplet exciton is preferred to improve the triplet migration possibility, an organic molecule having a large k_{ISC} with the suppression of a nonradiative decay process from a T_1 state should be considered as active molecules (*49*).

Since the proper management of spin-flip rate constants is crucial, the leading research topic in this thesis is that how should we control the both the forward and the reverse ISC process in purely aromatic molecules, especially, in intramolecular CT-type compounds exhibiting TADF? According to a classical model, k_{RISC} is expressed by Arrhenius equation,

$$k_{RISC} \approx A \times exp(-\Delta E_{S1-T1}/k_B T) \quad (9)$$

where A is the pre-factor including H_{SOC}, k_B is Boltzmann constant and T is temperature. Therefore, k_{RISC} depends on the $\Delta E_{S1\text{-}T1}$. As expected, TADF molecules with small $\Delta E_{S1\text{-}T1}$ show relatively high k_{RISC} value. However, although this concept has been widely supported by many researchers, there are several irregular points; the high k_{RISC} (~10^5 s^{-1}) value even for relatively large $\Delta E_{S1\text{-}T1}$ of ~0.2 eV as summarized in **Fig. 1-5**. This result clearly indicates that not only $\Delta E_{S1\text{-}T1}$ but also some factors influence on reverse ISC processes.

Recently, the importance of the intense interaction between the T_1 and higher triplet excited-

state (T_n) is suggested theoretically or experimentally for the ISC process in the molecule showing TADF properties (*50-54*). In particular, several groups propose the influence of second-order spin-vibronic coupling between CT and LE states, because the electron transition from a pure triplet CT (^{3}CT) to a pure singlet CT (^{1}CT) states, this case is a common transition in many TADF molecules because TADF molecules naturally formed CT states, is generally prohibited because of vanishing the H_{SOC} (*55*). These theoretical and experimental conclusions indicate that for efficient reverse ISC processes the mixing of LE character to a ^{3}CT state is required, and this efficient mixing can be achieved by small energy gap between ^{3}LE and ^{3}CT states ($|\Delta E_{3LE\text{-}3CT}|$). Based on these results, the understanding of spin-flip process in TADF molecules is in progress. However, there are a wide variety of CT-type molecular systems to which this mechanism cannot be applied. Thus, the exact spin-flip mechanisms in CT-type molecular systems remain under the veil of mysteries. In contrast to reverse ISC process, although a forward ISC process is a competing process for a reverse ISC process, there are few detailed studies of forward ISC processes. In particular, the transition state of the spin-flip process is under the mystery, and comprehensive understanding of the spin-flip process in CT type organic molecule contributes to an improvement of the performance of TADF molecules.

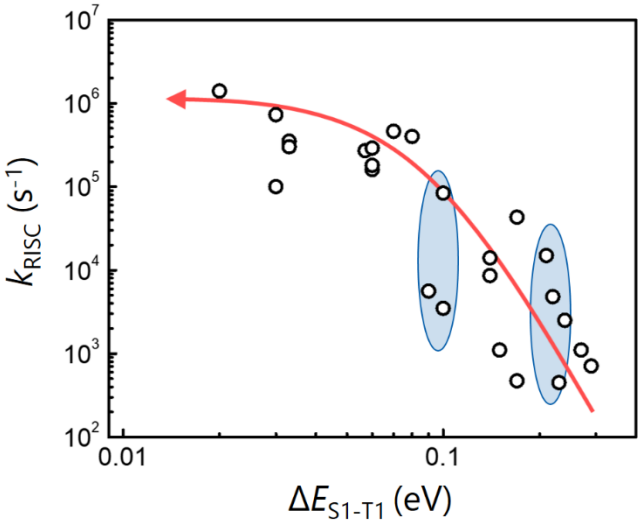

Figure 1-5 Relationship between k_{RISC} and $\Delta E_{S1\text{-}T1}$.

1-2. Purpose and outline

The purpose of this thesis is comprehensive understanding of spin-flip processes in purely CT-type aromatic molecules, and the establishment of material design rules to manage the spin-flip rate constants. This thesis is organized as follows.

In **Chapter 2**, in order to suppress an EL efficiency rolloff and an improve device operational

lifetime, I established novel molecular design for the enhancing not only the k_{RISC} but also the device operational stability under electrical excitation. I revealed that the excited-state alignment of ^{1}CT, ^{3}CT and ^{3}LE states is critical point to accelerate the k_{RISC} of an organic molecule exhibiting TADF. The excited-state alignment of ^{1}CT, ^{3}CT and ^{3}LE states can be achieved by introduction of the 'second' type of D unit in an initially D-A system while at the same time weakly pinning the ^{1}CT and ^{3}CT energy levels to those of the original D-A system, resulting in an effective mixing between CT and LE states and acceleration of the k_{RISC} while maintaining high PLQY. In particularly, the designed molecule 3Cz2DPhCzBN possesses a k_{RISC} (7.2×10^5 s^{-1}) that is more than three times larger than that of template molecule, 2,3,4,5,6-penta(9H-carbazol-9-yl)benzonitrile (5CzBN). In addition, operational stability of 3Cz2DPhCzBN-based OLED shows over 30 times longer than that of 5CzBN-based OLED.

In **Chapter 3**, in order to build our molecular design further strictly, I developed highly emissive TADF molecules, *p*-2Cz2BMe which shows high PLQY with long DF lifetime (millisecond order), by the excited-state energy level alignment. By selecting appropriate D and A units and utilize the charge-resonance (CR) effect, which is useful for stabilization of CT energy, the $|\Delta E_{3LE\text{-}3CT}|$ enlarges, resulting in a weak mixing of states between ^{3}CT and ^{3}LE states. In addition, the rigid and crowded structure prevents the nonradiative decay from the T_1 state, leading to efficient reverse ISC process although k_{RISC} (2.1×10^3 s^{-1}) is one of the smallest value compared to the k_{RISC} of the reported compounds, and PLQY of 89% is achieved.

In **Chapter 4**, I investigated spin-flip process of carbazole-cyano (CzCN) derivatives, which cannot be explained by the mechanism considering only a simple LE state. I show that efficient spin-flip in CT-type purely molecular systems involves the critical role of an intermediate triplet excited-state. The proposed mechanism can be applied to other multi-D-A CT-type molecules and I have succeeded in developing molecules that show the strict spin-flip process by using our proposed mechanism.

Finally, **Chapter 5** concludes and summarizes these studies. Based on unraveled spin-flip

mechanisms in purely organic CT-type molecules, I outlook future prospect of TADF technologies.

References

1. Lamola, A. A., Hammond, G. S., Mechanisms of Photochemical Reactions in Solution. XXXIII. Intersystem Crossing Efficiencies. *J. Chem. Phys.*, **43**, 2129-2135 (1965).

2. Baldo, M. A., O'Brien, D. F., You, Y., Shoustikov, A., Sibley, S., Thompson, M. E., Forrest, S. R., Highly efficient phosphorescent emission from organic electroluminescent devices. *Nature*, **395**, 151-154 (1998).

3. Reineke, S., Lindner, F., Schwartz, G., Seidler, N., Walzer, K., Lüssem, B., Leo, K., White organic light-emitting diodes with fluorescent tube efficiency. *Nature*, **459**, 234-238 (2009).

4. Uoyama, H., Goushi, K., Shizu, K., Nomura, H., Adachi, C., Highly efficient organic light-emitting diodes from delayed fluorescence. *Nature*, **492**, 234-238 (2012).

5. Hirata, S., Recent Advances in Materials with Room-Temperature Phosphorescence: Photophysics for Triplet Exciton Stabilization. *Adv. Opt. Mater.*, **5**, 1700116 (2017).

6. Zhao, Q., Huang, C., Li, F., Phosphorescent heavy-metal complexes for bioimaging. *Chem. Soc. Rev.*, **40**, 2508-2524 (2011).

7. Xiong, X., Song, F., Wang, J., Zhang, Y., Xue, Y., Sun, L., Jiang, N., Gao, P., Tian, L., Peng, X., Thermally Activated Delayed Fluorescence of Fluorescein Derivative for Time-Resolved and Confocal Fluorescence Imaging. *J. Am. Chem. Soc.*, **136**, 9590-9597 (2014).

8. Maeda, K., Henbest, K. B., Cintolesi, F., Kuprov, I., Rodgers, C. T., Liddell, P. A., Gust, D., Timmel, C. R., Hore, P. J., Chemical compass model of avian magnetoreception. *Nature*, **453**, 387-390 (2008).

9. Baluschev, S., Miteva, T., Yakutkin, V., Nelles, G., Yasuda, A., Wegner, G., Up-Conversion Fluorescence: Noncoherent Excitation by Sunlight. *Phys. Rev. Lett.*, **97**, 143903 (2006).

10. Castano, P., Mroz, P., Hamblim, M. R., Photodynamic therapy and anti-tumourimmunity. *Nat. Rev. Cancer*, **6**, 535-545 (2006).

11. Smith, M. B., Michi, J., Singlet Fission. *Chem. Rev.*, **110**, 6891-6936 (2010)

12. Turro, N. J., Ramamurthy, V., Scaiano, J. C., Principle of Molecular Photochemistry: An Introduction. Chapter **3**, p.113–118 (University Science Books, 2009).

13. Lower, S. K., El-Sayed, M. A., The Triplet State and Molecular Electronic Processes in Organic Molecules. *Chem. Rev.*, **66**, 199-241 (1966).

14. Dreeskamp, H., Koch, E., Zander, M., Fluorescence of bromoperylenes and the requirements of heavy-atom quenching. *Chem. Phys. Lett.*, **31**, 251-253 (1975).

15. Anderson, R. W., Hochstrasser, R. M., Lutz, H., Scott, G. W., Direct measurements of energy transfer between triplet states of molecules in liquids using picosecond pulses. *J. Chem. Phys.*, **61**, 2500-2506 (1974).

16. El-Sayed, M. A., The Radiationless Processes Involving Change of Multiplicity in the Diazenes. *J. Chem. Phys.*, **36**, 573-574 (1962).

17. Noutsuka, N., Kabe, R., Goushi, K., Adachi, C., Confinement of Long-Lived Triplet Excitons in Organic Semiconducting Host–Guest Systems. *Adv. Funct. Mater.*, **27**, 1703902 (2017).

18. Mieno, H., Kabe, R., Notsuka, N., Allendorf, M. D., Adachi, C., Long-lived Room-Temperature Phosphorescence of Coronene in Zeolitic Imidazolate Framework ZIF-8. *Adv. Opt. Mater.*, **4**, 1015-1021 (2016).

19. Kawamura, Y., Sasabe, H., Adachi, C., Simple Accurate System for Measuring Absolute Photoluminescence Quantum Efficiency in Organic Solid-State Thin Films. *Jpn. J. Appl. Phys*, **43**, 7729-7730 (2004).

20. Adachi, C., Baldo, M. A., Thompson, M. E., Forrest, S. R., Nearly 100% internal phosphorescence efficiency in an organic light-emitting device. *J. Appl. Phys.*, **90**, 5048-5050 (2001).

21. Parker, C. A., Hatchard, C. G., Triplet-singlet emission in fluid solutions. Phosphorescence of eosin. *Trans. Faraday Soc.*, **57**, 1894-1904 (1961).

22. Parker, C. A., Phosphorescence and Delayed Fluorescence from Solutions. Advances in Photochemistry, Vol. 2, Noyes, W. A., Hammond, G. S., Pitts J. N., Eds., pp. 305–383, John Wiley and Sons, New York (1964).

23. Boudin, S., Phosphorescence des solutions glycériques d'éosine influence des iodures. *J. Chim. Phys.*, **27**, 285–290 (1930).

24. Lewis, G. N., Lipkin, D., Magel, T. T., Reversible photochemical processes in rigid media. A study of the phosphorescent state. *J. Am. Chem. Soc.*, **63**, 3005–3018 (1941).

25. Saltiel, J., Curtis, H. C., Metts, L., Miley, J. W., Winterle, J., Wrighton, M., Delayed Fluroescence and Phosphorescence of Aromatic Ketones in Solution. *J. Am. Chem. Soc.*, **92**, 410-411 (1970).

26. Abedin, Z., Yamamoto, Y., Ohno, T., Nozaki, K., Structure-Dependent Photophysical Properties of Singlet and Triplet Metal-to-Ligand Charge Transfer States in Copper(I) Bis(diimine) Compounds. *Inorg. Chem.*, **42**, 6366-6378 (2003).

27. Iwamura, M., Takeuchi, S., Tahara, T., Real-Time Observation of the Photoinduced Structural Change of Bis(2,9-dimethyl-1,10-phenanthroline)copper(I) by Femtosecond Fluorescence Spectroscopy: A Realistic Potential Curve of the Jahn−Teller Distortion. *J. Am. Chem. Soc.*, **129**, 5248-5256 (2007).

28. Berberan-Santos, M. N., Garcia, J. M. M., Unusually strong delayed fluorescence of C_{70}. *J. Am. Chem. Soc.*, **118**, 9391–9394 (1996).

29. Yang, Z., Mao, Z., Xie, Z., Zhang, Y., Liu, S., Zhao, J., Xu, J., Chi, Z., Aldred, M. P., Recent advances in organic thermally activated delayed fluorescence materials. *Chem. Soc. Rev.*, **46**, 915-1016 (2017).

30. Baldo, M. A., O'Brien, D. F., Thompson, M. E., Forrest, S. R., Excitonic singlet-triplet ratio in a semiconducting organic thin film. *Phys. Rev. B*, **60**, 14422-14428 (1999).

31. Segal, M., Baldo, M. A., Holmes, R. J., Forrest, S. R., Soos, Z. G., Excitonic singlet-triplet ratios in molecular and polymeric organic materials. *Phys. Rev. B*, **68**, 075211 (2003).

32. Murawski, C., Leo, K., Gather, M. C., Efficiency Roll-Off in Organic Light-Emitting Diodes. *Adv. Mater.*, **25**, 6801-6827 (2013).

33. Baldo, M. A., Adachi, C., Forrest, S. R., Transient analysis of organic electrophosphorescence. II. Transient analysis of triplet-triplet annihilation. *Phys. Rev. B*, **62**, 10967-10977 (2000).

34. Klubek, K. P., Tang, C. W., Rothberg, L. J., Investigation of blue phosphorescent organic light-emitting diode host and dopant stability. *Org. Electron.*, **15**, 1312-1316 (2014).

35. Segal, M., Mulder, C., Celebi, K., Sing, M., Rivoire, K., Difley, S., Voorhis, T. V., Baldo, M. A., Spin and Device Engineering for Blue Organic Light Emitting Devices. *Proc SPIE*, **6999**, 699912 (2008).

36. Endo, A., Ogasawara, M., Takahashi, A., Yokoyama, D., Kato, Y., Adachi, C., Thermally Activated Delayed Fluorescence from Sn^{4+}–Porphyrin Complexes and Their Application to Organic Light Emitting Diodes — A Novel Mechanism for Electroluminescence. *Adv. Mater.* **21**, 4802-4806 (2009).

37. Osaheni, J. A., Jenekhe, S. A., Efficient blue luminescence of a conjugated polymer exciplex. *Macromolecules*, **27**, 739–742 (1994).

38. Berggren, M. Gustafsson, G., Inganäs, O., White light from an electroluminescent diode made from poly[3(4-octylphenyl)-2,2'-bithiophene] and an oxadiazole derivative. *J. Appl. Phys.*, **76**, 7530‑7534 (1994).

39. Goushi, K., Yoshida, K., Sato, K., Adachi, C., Organic light-emitting diodes employing efficient reverse intersystem crossing for triplet-to-singlet state conversion. *Nat. Photon.*, **6**, 253-258 (2012).

40. Sarma, M., Wong, K. T., Exciplex: An Intermolecular Charge-Transfer Approach for TADF. *ACS Appl. Mater. Interfaces*, **10**, 19279-19304 (2018).

41. Zhang, Q., Li, B., Huang, S., Nomura, H., Tanaka, H., Adachi, C., Efficient blue organic light-emitting diodes employing thermally activated delayed fluorescence. *Nat. Photon.*, **8**, 326-332 (2014).

42. Zeng, W., Lai, H. Y., Lee, W. K., Jiao, M., Shiu, Y. J., Zhong, C., Gong, S., Zhou, T., Xie, G., Sarma, M., Wong, K. T., Wu, C. C., Yang, C., Achieving Nearly 30% External Quantum Efficiency for Orange–Red Organic Light Emitting Diodes by Employing Thermally Activated Delayed Fluorescence Emitters Composed of 1,8-Naphthalimide-Acridine Hybrids. *Adv. Mater.*, **30**, 1704961 (2018).

43. Shizu, K., Noda, H., Tanaka, H., Taneda, M., Uejima, M., Sato, T., Tanaka, K., Kaji, H., Adachi, C., Highly Efficient Blue Electroluminescence Using Delayed-Fluorescence Emitters with Large Overlap Density between Luminescent and Ground States. *J. Phys. Chem. C*, **119**, 26283-26289 (2015).

44. Kaji, H., Suzuki, H., Fukushima, T., Shizu, K., Suzuki, K., Kubo, S., Komino, T., Oiwa, H., Suzuki, F., Wakamiya, A., Murata, Y., Adachi, C., Purely organic electroluminescent material realizing 100% conversion from electricity to light. *Nat. Commun.*, **6**, 8476 (2015).

45. Furukawa, T., Nakanotani, H., Inoue, M., Adachi, C., Dual enhancement of electroluminescence efficiency and operational stability by rapid upconversion of triplet excitons in OLEDs. *Sci*. *Rep*., **5**, 8429 (2015).

46. Masui, K., Nakanotani, H., Adachi, C., Analysis of exciton annihilation in high-efficiency sky-blue organic light-emitting diodes with thermally activated delayed fluorescence. *Org. Electron.*, **14**, 2721–2726 (2013).

47. Hynes, J., Floyd, S., Soini, A., O'Connor, R., Papkovsky, D. B., Fluorescence-Based Cell Viability Screening Assays Using Water-Soluble Oxygen Probes. *J. Biomol*. *Screen*., **8**, 264-272 (2003).

48. Hasebe, N., Suzuki, K., Horiuchi, H., Suzuki, H., Yoshihara, T., Okutsu, T., Tobita, S., Intracellular and in Vivo Oxygen Sensing Using Phosphorescent Ir(III) Complexes with a Modified Acetylacetonato Ligand. *Anal*. *Chem*., **87**, 2360-2366 (2015).

49. Yanai, N., Kimizuka, N., Recent emergence of photon upconversion based on triplet energy migration in molecular assemblies. *Chem*. *Commun*., **52**, 5354-5370 (2016).

50. Chen, X. K., Zhang, S. F., Fan, J. X., Ren, A. M., Nature of Highly Efficient Thermally Activated Delayed Fluorescence in Organic Light-Emitting Diode Emitters: Nonadiabatic Effect between Excited states. *J. Phys*. *Chem*. *C*, **119**, 9728-9733 (2015).

51. Gibson, J., Monkman, A. P., Penfold, T. J., The Importance of Vibronic Coupling for Efficient Reverse Intersystem Crossing in Thermally Activated Delayed Fluorescence Molecules. *ChemPhysChem*, **17**, 2956-2961 (2016).

52. Dias, F. B., Santos, J., Graves, D. R., Data, P., Nobuyasu, R. S., Fox, M. A., Batsanov, A. S., Palmeira, T., Berberan-Santos, M. N., Bryce, M. R., Monkman, A. P., The Role of Local Triplet Excited states and D-A Relative Orientation in Thermally Activated Delayed Fluorescence: Photophysics and Devices. *Adv. Sci*., **3**, 1600080 (2016).

53. Marian, C. M., Mechanism of the Triplet-to-Singlet Upconversion in the Assistant Dopant ACRXTN. *J. Phys. Chem. C*, **120**, 3715-3721 (2016).

54. Hosokai, T., Matsuzaki, H., Nakanotani, H., Tokumaru, K., Tsutsui, T., Furube, A., Nasu, K., Nomura, H., Yahiro, M., Adachi, C., Evidence and Mechanism of Efficient Thermally Activated Delayed Fluorescence Promoted by Delocalized Excited states. *Sci. Adv.*, **3**, e1603282 (2017).

55. Lim, B. T., Okajima, S., Chandra, A. K., Lim, E. C., Radiationless transitions in electron donor-acceptor complexes: selection rules for $S_1 \rightarrow T$ intersystem crossing and efficiency of $S_1 \rightarrow S_0$ internal conversion. *Chem*. *Phys*. *Lett*., **79**, 22-27 (1981).

Chapter 2

Excited-state engineering for efficient reverse intersystem crossing

Hiroki Noda, Hajime Nakanotani, & Chihaya Adachi
Science Advances, **4**, eaao6910, (2018)

Abstract

Reverse ISC from a T state to a S state is an attractive route to harvesting electrically generated triplet exciton as light, leading to highly efficient OLEDs. An ideal EL efficiency of 100% can be achieved by using highly efficient reverse ISC, but the suppression of efficiency rolloff and longer device lifetime have been still required. In this chapter, I establish molecular design rules for enhancing not only k_{RISC} but also operational stability under electrical excitation. I show that the introduction of a second D unit in an original D-A system induces effective mixing between CT and LE states, resulting in acceleration of the reverse ISC rate while maintaining high PLQY. OLEDs using the designed sky-blue emitter achieved a nearly 100% exciton production efficiency and exhibited not only low efficiency rolloff but also a dramatic improvement of operational stability.

2-1. Introduction

OLEDs, which can reach IQE of nearly 100%, are one of the most promising devices for next generation display and lighting applications. According to spin statistics (*1*), 75% of excitons are directly generated in a T state after carrier recombination, so two approaches exist for obtaining an ideal IQE: RTP (*2,3*), in which triplet excitons directly produce EL, and TADF (*4*), in which the reverse ISC of triplet excitons to a S state results in DF. In particular, since molecules exhibiting TADF can be designed without using expensive rare-metal elements such as Ir, the number of reports on molecular design for TADF has significantly increased (*5*), resulting in an abundance of emitter molecules achieving an ideal IQE (*6-8*). However, an investigation on not only the understanding of reverse ISC mechanism but also the relationship between k_{RISC} and molecular design, which is a critical issue for the development of high performance, commercially viable TADF-OLEDs, especially with blue emission, is still missing.

Reduction of exciton density (n_S for singlet and n_T for triplet) in TADF-OLEDs during electrical excitation is a key consideration for improving operational stability (*9,10*). In particular, high n_T induces detrimental exciton annihilation and/or chemical reactions because of the long exciton lifetime of triplets (*11,12*). Recently, Nakanotani et al. reported that by combing TADF molecules as energy donors and fluorescent molecules as energy acceptor and energy transfer of the triplet excitons generated on TADF molecules to the S_1 state of fluorescent molecules (TAF-system), narrow emission spectra (good color purity) originated from fluorescent molecules and high operational stability can be achieved (*9*). The characters of TAF-system are good color purity from fluorescent molecules and reduction of n_T because the rate constant of energy transfer via dipole–dipole coupling (that is, Förster energy transfer, FRET) (k_{FRET}) is much faster than that of radiative decay from S_1 (k_r) and k_{ISC} on a TADF molecule (*9,10*). Such properties lead to suppression of the rolloff characteristics and improvement of the operational lifetime. Thus, TAF-system is one of the promising methods for solving the problem of TAF-OLEDs. However, there are still few reports on TAF-OLEDs with long operational lifetime (*10,13*), since the stability of the TAF-system depends on

TADF materials themselves. Thus, in order to improve the stability of the TADF molecules, the k_{RISC} should be maximized and the n_T on the TADF molecules should be decreased. The basic molecular design for increasing k_{RISC} in aromatic compounds can be realized by reducing the $\Delta E_{S1\text{-}T1}$ because the first-order coefficient for mixing between the two states is inversely proportional to $\Delta E_{S1\text{-}T1}$ (*14*). In addition, the influence of not only $\Delta E_{S1\text{-}T1}$ but also second-order spin-vibronic coupling between CT and LE triplet states on the reverse ISC process has been proposed by several groups recently (*15-20*). These theoretical and experimental conclusions indicate that the mixing of wavefunctions between CT and LE is an important factor for accelerating reverse ISC in TADF molecules. However, there is still no clear molecular designs to realize maximum TADF performance based on these principles. Another important consideration is the charge transport abilities of the TADF molecules inside the EML. Since a narrow carrier recombination zone in the EML induces a high n_S and n_T, the carrier recombination zone should be expanded as much as possible (*21,22*).

Here, I propose a molecular design to establish both 1) effective mixing of the wavefunction between CT and LE states and 2) tuning of charge transport ability by the introduction of a second D unit (D_2) in an original D-A system. The designed molecule exhibits a k_{RISC} that is one order of magnitude larger than that of the template molecule while maintaining a high PLQY. Furthermore, TADF-OLEDs using the molecule as an emitter exhibit not only a remarkable enhancement of operational stability but also suppression of exciton annihilation processes with an EQE of over 20% even in the high luminance region.

2-2. Results and discussion

2-2-1. Heterodonor-acceptor (D-D_2-A) design

The molecular design for ideal TADF performance requires the following four conditions. (I) The organic molecule should have a D-A system to form intramolecular CT states, which provide small $\Delta E_{S1\text{-}T1}$ according to a spatial separation of the HOMO and LUMO. (II) The molecule should have two or more D units to form a delocalized CT triplet state ($^3CT^{de}$) (*19*), which provides a stable

T state. (III) The conformational change between S and T should be suppressed to achieve high device stability, so a sterically crowded molecule is preferred. (IV) Finally, since electron transition between a pure ^{3}CT and a pure ^{1}CT states is forbidden because of a vanishing of the SOC matrix elements between these molecular orbitals, the mediation of a molecular orbital having another orbital character other than CT, such as an LE state, is required to open a route for reverse ISC. This can be enhanced by mixing of LE character to an excited-state wavefunction of ^{3}CT, *i.e.*, small $|\Delta E_{3\text{LE-}3\text{CT}}|$.

In this study, 5CzBN, which has five carbazole (Cz) units and one benzonitrile (BN) unit, was used as a template molecule (**Fig. 2-1a**) (*23*). BN is well known to be a strong A unit with a high ^{3}LE$_1$ of 3.32 eV (*24*). On the other hand, phenyl-Cz (PhCz) is often used as a D unit, especially in blue TADF emitters, because PhCz also possesses a high ^{3}LE$_1$ of 3.10 eV. Therefore, combination of these D and A units in 5CzBN leads to the effective transfer of an excited electron on the Cz to BN, resulting in the formation of ^{1}CT$_1$ (2.94 eV) and ^{3}CT$_1$ (2.77 eV). While Hosokai et al. already reported that the T$_1$ state of 5CzBN has CT character (*25*), I also confirmed the solvatochromism of the

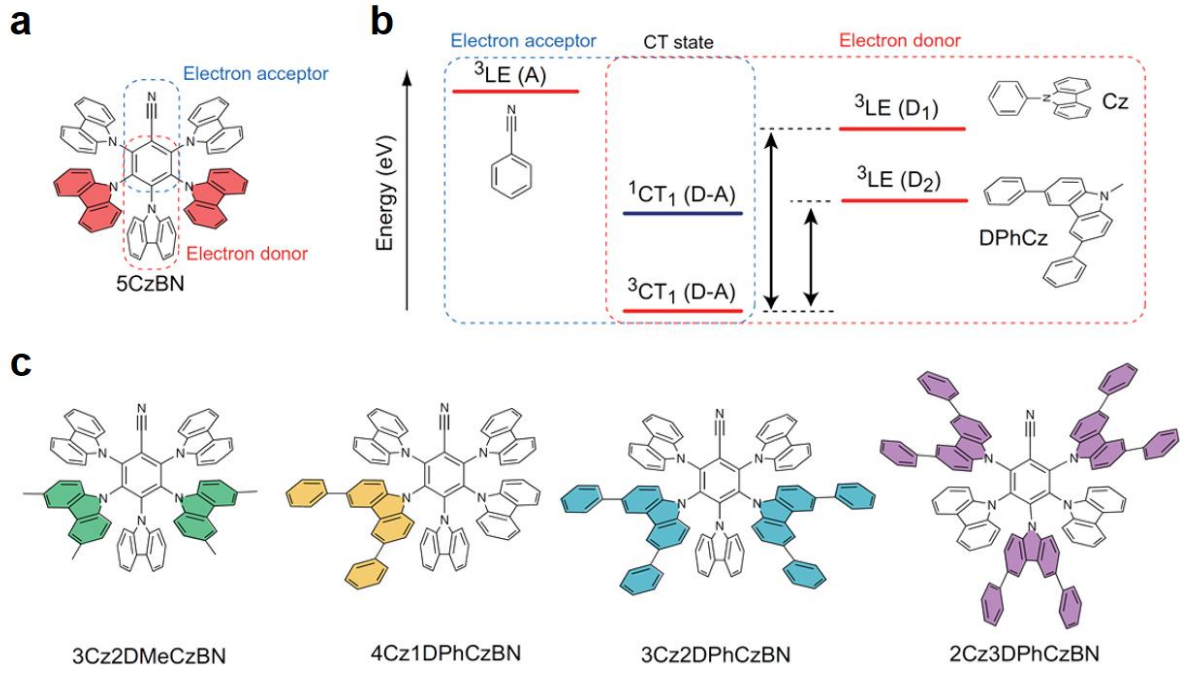

Figure 2-1 (**a**) Chemical structure of 5CzBN. (**b**) Schematic illustration of ^{1}CT$_1$, ^{3}CT$_1$ and ^{3}LE$_1$ energy level alignment for reverse ISC. (**c**) Chemical structures of D-D$_2$-A-type CzBN derivatives. The second type of substituted donor units are highlighted in the chemical structures.

phosphorescence spectra of 5CzBN (**Fig. 2-2**), indicating that the T_1 state of 5CzBN possesses more CT character than LE character despite the vibronic phosphorescence spectra. In addition, the presence of a radical Cz cation in the triplet excited-state of 5CzBN was experimentally confirmed by transient absorption spectroscopy (TAS) (*19*), indicating again the formation of a CT state in the triplet excited-state. Here note that the origin of the vibronic spectrum of the phosphorescence in toluene is unclear at this stage. Since the molecular structure of 5CzBN is rigid and dense, one possible reason for the origin of the vibronic spectrum of the phosphorescence is the suppression of molecular vibrations at 77 K. Since the $^3LE_1$ energies of Cz and BN are much higher than the $^3CT_1$ energy of 5CzBN, the triplet energy of $^3CT_1$ is sufficiently confined, resulting in a molecule showing TADF activity. However, the energy gap between $^3LE_1$ of Cz and $^3CT_1$ ($|\Delta E_{3LE\text{-}3CT}|$ = 0.32 eV) is much larger than $\Delta E_{S1\text{-}T1}$ (0.17 eV). Therefore, 5CzBN does not sufficiently satisfy the condition IV because of not only the weak mixing between ^3LE and ^3CT but also the endothermic positioning of $^3LE_1$ relative to $^1CT_1$.

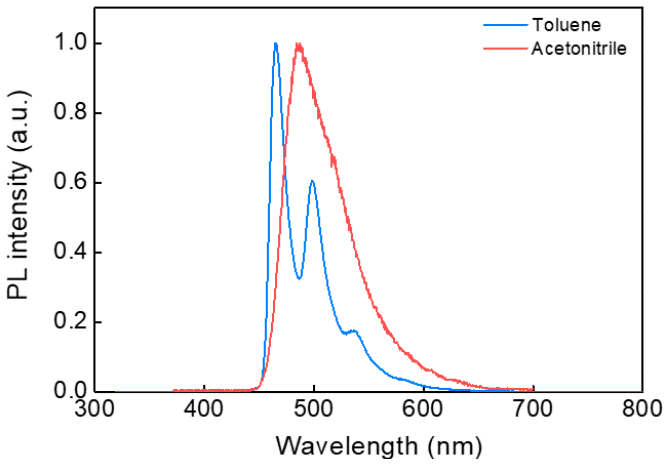

Figure 2-2 Phosphorescence spectra of 5CzBN in toluene and acetonitrile solutions.

To satisfy condition IV, I propose the introduction of D_2 units having a lower $^3LE_1$ than that of PhCz while maintaining the original Cz-BN-based CT system (**Fig. 2-1b**). To maintain the original D-A CT system, I introduced the D_2 in the *m*-position of BN because the *o*, *p*-position of BN shows high electron accepting properties. **Figure 2-1c** shows the chemical structures of our designed molecules. Since substitution of aromatic or methyl groups in the 3,6-position of Cz is expected to lower the $^3LE_1$ energy, 3,6-diphenylcarbazole (DPhCz) and 3,6-dimethylcarbazole (DMeCz) were used as D_2. These compounds were easily synthesized by a nucleophilic substitution reaction with good reaction yields of over 80%. Although 5CzBN showed a low solubility (< 0.1 wt%) in toluene,

a good solubility of over 0.1 wt% was obtained for 3Cz2DPhCzBN even with its higher molecular weight (MW = 1232.46) than 5CzBN (MW = 928.33). This is likely due to a reduction of molecular symmetry, and this improved solubility can enable easier purification of the compounds and the possibility for fabrication of OLEDs by solution processing.

2-2-2. Photoluminescence property relationship

First, to confirm if the type of D_2 has an effect on the improvement of the reverse ISC process, I compared PL characteristics of 5CzBN, 3Cz2DMeCzBN and 3Cz2DPhCzBN. Although the fluorescence spectra of 3Cz2DMeCzBN and 3Cz2DPhCzBN were slightly redshifted, the emission was still sky-blue with a peak wavelength of 480 nm as shown in **Fig. 2-3**. Further, the modification of the initial D-A system by D_2 had no effect on $\Delta E_{S1\text{-}T1}$ (0.15 ~ 0.17 eV) in 5CzBN (*19*), 3Cz3DMeCzBN, and 3Cz2DPhCzBN, which was confirmed experimentally from the difference in the onset energies of fluorescence and phosphorescence in diluted toluene solutions (**Fig. 2-3**). Thus, these compounds might be expected to exhibit similar TADF properties. However, as summarized in **Table 2-1**, their properties are significantly different.

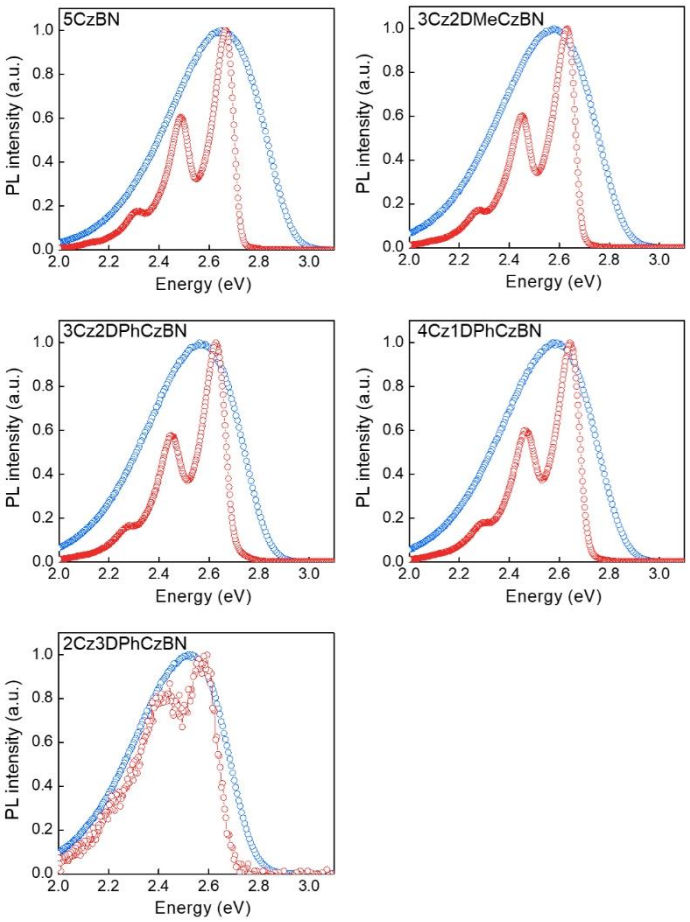

Figure 2-3 Fluorescence and phosphorescence spectra of CzBN derivatives. Blue circles show fluorescence and red circles show phosphorescence spectra.

Table 2-1 Photophysical characteristics of CzBN derivatives in toluene

Compound	PL_{max} (nm)	PLQY (%)*1)	$\Delta E_{S1\text{-}T1}$ (eV)*2)	$\lvert\Delta E_{3LE\text{-}3CT}\rvert$ (eV)*3)	$\lvert\Delta E_{1CT\text{-}3LE}\rvert$ (eV)*4)	E_a (eV)*5)	τ_p (ns)	τ_d (μs)	k_r (10^7 s^{-1})	k_{ISC} (10^8 s^{-1})	k_{RISC} (10^5 s^{-1})	k_{nrT} (10^4 s^{-1})
5CzBN	470	7 / 75	0.17	0.32	0.15	0.13	3.8	46.8	1.9	2.5	2.2	0.6
3Cz2DMeCzBN	480	8 / 85	0.17	0.30	0.13	0.10	5.9	23.6	1.3	1.5	4.4	0.7
4Cz1DPhCzBN	480	11 / 85	0.15	0.16	0.01	0.09	7.0	19.4	1.6	1.3	3.9	0.9
3Cz2DPhCzBN	480	9 / 81	0.15	0.16	0.01	0.06	5.8	12.2	1.5	1.5	7.2	1.7
2Cz3DPhCzBN	492	13 / 83	0.13	0.19	0.06	0.08	5.2	6.1	2.5	1.7	10.2	3.2

*1) PLQY for before (left) and after (right) Ar bubbling. The error is ± 2 %. *2) Energy gap between S_1 and T_1 state. The error is ± 0.03 eV. *3) Energy gap between $^3CT_1$ and $^3LE_1$ state. The error is ± 0.03 eV. *4) Energy gap between $^1CT_1$ and $^3LE_1$ state. The error is ± 0.03 eV. *5) The error is ± 0.01 eV.

All of the compounds exhibited similar k_r of 1.3–2.5 × 10^7 s^{-1} and a dramatic increase in PLQY attributed to DF after degassing by bubbling with argon (**Table 2-1**), indicating that the triplet excitons efficiently convert to singlet excitons through reverse ISC and then emit DF. On the other hand, the DF lifetime (τ_d) greatly decreased with the introduction of D_2, resulting in a faster τ_d of 12.0 μs for 3Cz2DPhCzBN than for 5CzBN (46.8 μs) as shown in **Fig. 2-4a**. Because of the reduction of τ_d while maintaining a high PLQY, 3Cz2DPhCzBN possesses a k_{RISC} (7.2 × 10^5 s^{-1}) that is more than three times larger than that of 5CzBN. To assess the reverse ISC processes in these compounds in more detail, the temperature dependence of k_{RISC} was measured. From an Arrhenius plot of the k_{RISC}, the activation energies for reverse ISC (E_A^{RISC}) were estimated to be 0.13, 0.10 and 0.06 eV for 5CzBN, 3Cz2DMeBN and 3Cz2DPhCzBN, respectively (**Fig. 2-4b**), clearly indicating a reduction of E_A^{RISC} that is independent of $\Delta E_{S1\text{-}T1}$. Note that the nonradiative decay rate from T_1 (k_{nr}^T) of 5CzBN (k_{nr}^T = 0.6 × 10^4 s^{-1}) was smaller than that of 3Cz2DPhCzBN, so the suppression of k_{nr}^T is not responsible for the faster τ_d.

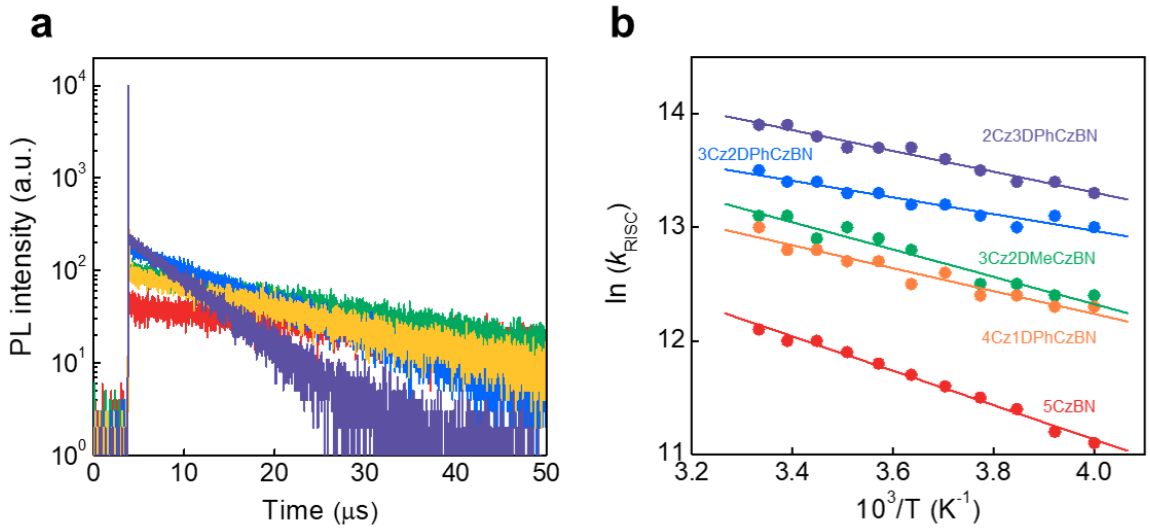

Figure 2-4 (**a**) PL transient decay curves of CzBN derivatives in oxygen free toluene at 295 K. (**b**) Arrhenius plots of the k_{RISC} for CzBN derivatives.

Next, to check the effect of the number of D_2 units, I designed 4Cz1DPhCzBN and 2Cz3DPhCzBN, which have one and three D_2 units of DPhCz, respectively. The fluorescence and phosphorescence spectra and PLQY of 4Cz1DPhCzBN nearly match those of 3Cz2DPhCzBN, so the compounds might be expected to also have similar $\Delta E_{S1\text{-}T1}$. However, a smaller k_{RISC} of 3.9×10^5 s^{-1} was observed for 4Cz1DPhCzBN, leading to slightly large E_A^{RISC} of 0.09 eV. On the other hand, 2Cz3DPhCzBN has a k_{RISC} (1.0×10^6 s^{-1}) that is one order of magnitude higher than that of 5CzBN, but its emission spectrum is markedly redshifted compared to that of 5CzBN. This redshift indicates that the DPhCz unit acts as the primary donor rather than D_2, which is a result of the DPhCz units substituted in *o*- and *p*-positions of BN, leading to the CT formation between DPhCz and BN units.

To understand the increase of k_{RISC} without a reduction of $\Delta E_{S1\text{-}T1}$, I examined $^3LE_1$ of D_2 in these compounds because the A unit remained constant. **Figures 2-5a, b** showed the molecular structures and phosphorescence spectra of PhCz, 5CzPh, 2DMeCzPh, 3DPhCzPh, 2DPhCzPh and 1DPhCzPh in toluene solutions. The phosphorescence spectrum of 5CzPh closely resembles that of PhCz, indicating that the $^3LE_1$ of 5CzPh is from PhCz. This case is specific to TADF molecules using Cz as a D moiety. For example, in the case of a diphenylamine, which is also widely used in TADF molecules, increasing the number of diphenylamine units leads to a lower triplet energy as shown in

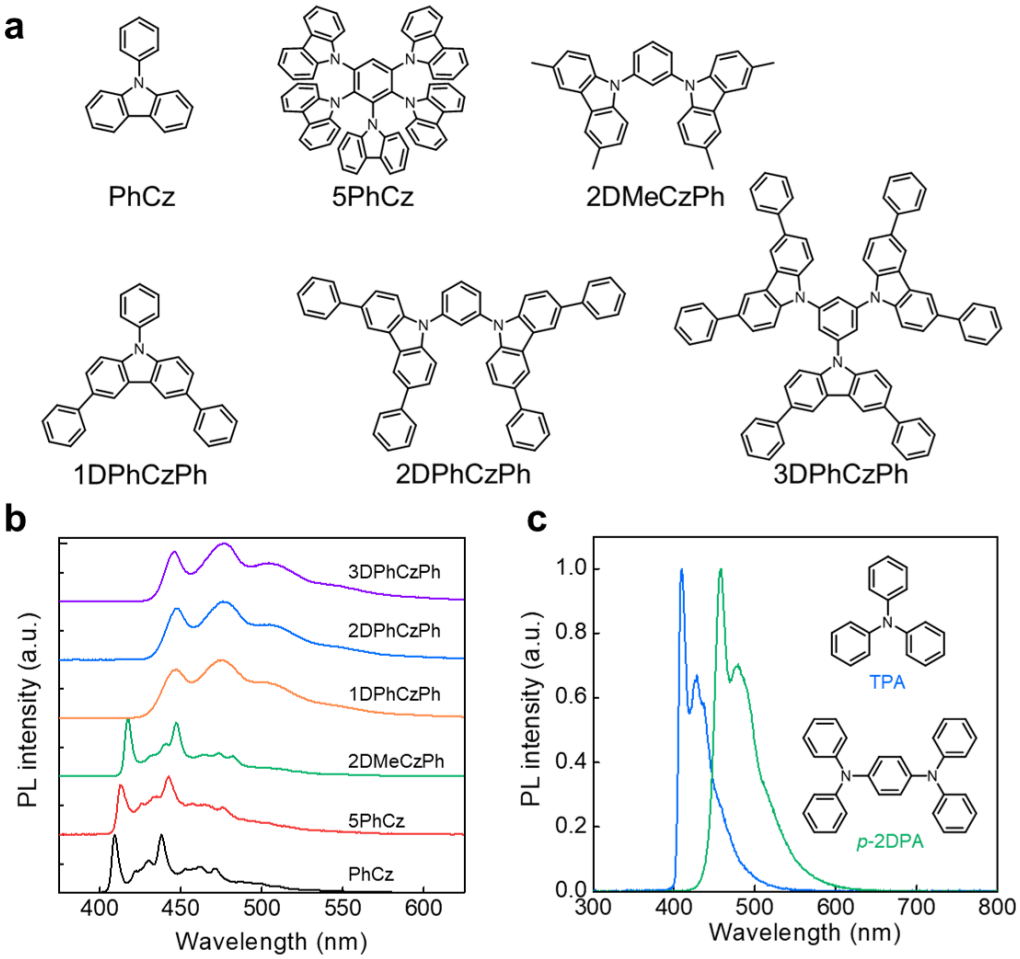

Figure 2-5 (**a**) Molecular structures of CzPh, 5CzPh, 2DMeCzPh, 1DPhCzPh, 2DPhCzPh and 3DPhCzPh. (**b**) Phosphorescence spectra of CzPh, 5CzPh, 2DMeCzPh, 1DPhCzPh, 2DPhCzPh and 3DPhCzPh in oxygen free toluene at 77 K. (**c**) Phosphorescence spectra of triphenylamine (TPA) and 1,4-bis(diphenylamino)benzene (*p*-2DPA) in toluene solutions.

Fig. 2-5c. On the other hand, the $^3LE_1$ energies of 2DMeCzPh (2.99 eV) and 2DPhCzPh (2.87 eV) are noticeably lower than that of 5CzPh (3.10 eV), leading to a reduction of $|\Delta E_{3LE\text{-}3CT}|$ as shown in **Fig. 2-6**. Thus, by introduction of 2DMeCzPh and 2DPhCzPh as the D_2 units in 5CzBN, the ^3LE states could be controlled. These results provide experimental evidence of not only the possibility to tune the energy level of the $^3LE_1$ state by introducing a D_2 into a D-A system but also of the strong influence of the energy level alignment of $^3LE_1$, $^3CT_1$, and $^1CT_1$, *i.e.*, $|\Delta E_{3LE\text{-}3CT}|$ and the energy gap between ^1CT and ^3LE ($|\Delta E_{1CT\text{-}3LE}|$), on reverse ISC. Although I cannot completely exclude the presence of unknown triplet excited-states between $^3LE_1$ of the donor moiety and $^3CT_1$ of the compound, the decrease of the ^3LE state of the D moiety should cause mixing between LE and CT character naturally when the D and A moieties are combined, leading to acceleration of k_{RISC}. Thus,

by introduction of a D_2, mixing between the ^{3}LE state and other triplet states will be increased because of the reduction of the energy level of the ^{3}LE state.

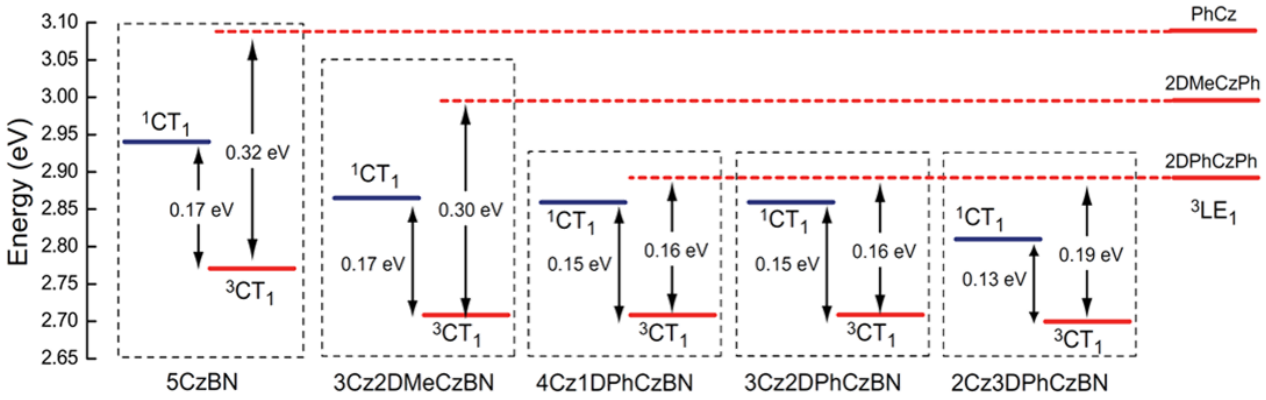

Figure 2-6 Energy level diagram of CzBN derivatives. The dashed red lines indicate the ^{3}LE$_1$ of CzPh derivatives for reference.

Although ^{3}LE$_1$ exhibits no dependency on the number of DPhCz units in **Fig. 2-5a**, k_{RISC} clearly changes with the number of D_2 units. Since second-order spin-vibronic coupling is related to the term $|\langle {}^1\Psi_{CT}|H_{SOC}|{}^3\Psi_{LE}\rangle\langle {}^3\Psi_{LE}|H_{vib}|{}^3\Psi_{CT}\rangle|^2$ (*16*), increasing the number of D_2 units increases the probability for vibronic coupling between the ^{3}LE state and the ^{3}CT state by the increasing of the electron density of D_2 units, thereby effectively inducing reverse ISC through second-order spin-vibronic coupling. In fact, the phosphorescence lifetime of 3Cz2DPhCzBN (120 ms) was appreciably shorter than those of 4Cz1DPhCzBN (136 ms) or 5CzBN (138 ms), indicating the strong mixing between S and T via second-order spin-vibronic coupling. These experimental results provide us with a clear molecular design rule for accelerating reverse ISC: minimize $|\Delta E_{3LE\text{-}3CT}|$ in addition to $\Delta E_{S1\text{-}T1}$, which can be done by introducing an appropriate number of a D_2 unit with a suitable donating ability. In addition, note that these findings also have consequences for the choice of a host-guest matrix for TADF emitters. Since ^{3}LE$_1$ clearly influences the reverse ISC process, organic molecules that have triplet energies higher than not only ^{3}CT$_1$ but also ^{3}LE$_1$ of the TADF emitter are favorable as the host matrix to suppress back-energy transfer from ^{3}LE$_1$ of the TADF emitter to a triplet state of the host matrix.

2-2-2. OLED performance

To demonstrate the impact of an increased k_{RISC} on OLED performance, I fabricated OLEDs with 5CzBN or 3Cz2DPhCzBN: mCBP co-deposited films as an EML. The photophysical properties of 3Cz2DPhCzBN are almost same as that of 5CzBN, but there is only difference in terms of k_{RISC}. Therefore, I investigated the OLEDs properties with 5CzBN or 3Cz2DPhCzBN as the emitters. Schematic diagrams of the energy levels of the fabricated devices and the chemical structures of the organic semiconductor materials used in them are presented in **Section 2-4-2** (*26*). Here, note that 20wt%-doped codeposited films showed the total PLQY of 65±2 and 80±2% for 5CzBN and 3Cz2DPhCzBN, respectively (**Table 2-2**).

Table 2-2 Photophysical characteristics of 20wt%-doped mCBP films

Compound	PL_{max} (nm)	PLQY (%)*1)	τ_p (ns)	τ_d (μs)	k_r (10^7 s^{-1})	k_{ISC} (10^8 s^{-1})	k_{RISC} (10^5 s^{-1})	k_{nrT} (10^4 s^{-1})
5CzBN	486	16 / 49 / 65	3.2	10.2	5.0	2.6	3.6	4.1
3Cz2DPhCzBN	495	14 / 66 / 80	4.5	5.65	3.0	1.9	9.9	4.1

*1) PLQY for prompt (left), delayed component (center) and total (right). The error is ± 2 %

The OLED characteristics of the fabricated OLEDs are shown in **Figs. 2-7a-d** and summarized in **Table 2-3**. The EL spectrum of each device was redshifted compared with that of the emitter in solution because of the relatively high doping concentration of the emitters, but the EL emission color coordinates still correspond to bluish-green emission. **Figure 2-7b** shows the EQE-luminance characteristics of the tested OLEDs. The OLEDs exhibited high EQE at 500 cd m^{-2} of 18.0% for 5CzBN and 20.9% for 3Cz2DPhCzBN.

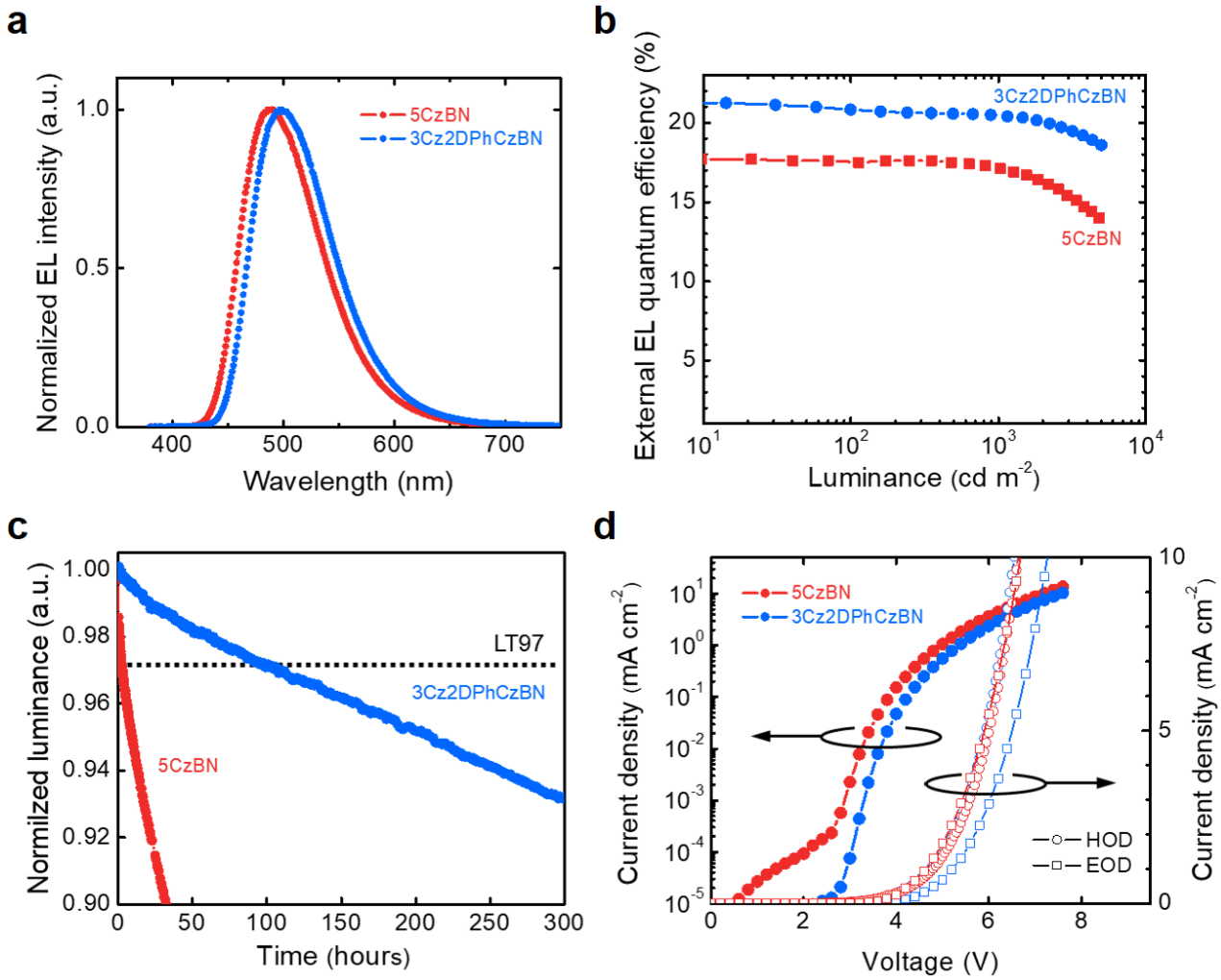

Figure 2-7 (**a**) EL spectrum in the OLEDs at 100 cd m^{-2}. (**b**) External EL quantum efficiency in the OLEDs as a function of luminance. (**c**) Normalized luminance of the OLEDs as a function of operating time at a constant current density. The initial luminance was 1,000 cd m^{-2} for each OLED, which was corresponding to constant driving current density at 2.4 and 1.6 mA cm^{-2} for 5CzBN and 3Cz2DPhCzBN based OLED, respectively. (**d**) Current density–voltage characteristics for OLEDs (filled circles), EODs (open squares), and HODs (open circles) based on 5CzBN or 3Cz2DPhCzBN as the dopant.

Table 2-3 Device performance of OLEDs based on CzBN emitters

Emitter	Voltage (V) *1)	EQE (%) *1)	Current efficiency (cd A^{-1}) *1)	CIE	LT97 (hour) *2)
5CzBN	5.0 / 5.6 / 7.7	18.0 / 17.0 / 13.9	44.9 / 43.6 / 35.0	(0.19, 0.41)	3
3Cz2DPhCzBN	5.2 / 5.8 / 7.4	20.9 / 20.8 / 18.6	63.0 / 62.2 / 55.9	(0.21, 0.44)	110

*1) Voltage, EQE and current efficiency were obtained at 500 / 1000 / 5000 cd m^{-2}, respectively. The error for EQE is ±0.2%, which was obtained from at least four devices. *2) Initial luminance of 1,000 cd m^{-2}.

Next, I assessed the operational stability of the fabricated OLEDs. **Figure 2-7c** shows the normalized luminance of the two representative OLEDs as a function of operational time under constant current density at an initial luminance L_0 of 1,000 cd m^{-2}. Although a rapid decrease of luminance with increasing operation time was observed in the 5CzBN-based OLED, for which the time until the luminance decreased to 97% of the initial (LT97) was only 3 h, a dramatic enhancement of operational stability was observed in the 3Cz2DPhCzBN-based OLED, resulting in an LT97 of over 100 h.

To assess the effect of the exciton annihilation process on the significant device lifetime enhancement, STA rate constant (k_{STA}) and TTA rate constant (k_{TTA}) of designed molecule were estimated using the rate equations (10, 11).

$$\frac{dN_s}{dt} = -(k_r^S + k_{ISC})N_s + k_{RISC}N_T - k_{STA}N_S N_T + \alpha k_{TTA}N_T^2 + \frac{J}{4de} \quad (10)$$

$$\frac{dN_T}{dt} = k_{ISC}N_S - (k_{RISC} + k_{nr}^T)N_T - (1+\alpha)k_{TTA}N_T^2 + \frac{3J}{4de} \quad (11)$$

where N_S and N_T are the singlet and triplet exciton densities, respectively, J is the current density, d is the recombination zone thickness, e is the electron charge, and α is the singlet exciton production ratio *via* TTA, which is 0.25 according to spin statistics (*11*). By fitting the experimental EQE-current density data with equations (10) and (11) (**Fig. 2-8a**), k_{STA} = 4.0 × 10^{-11} cm^3 s^{-1} and k_{TTA} = 6.0 × 10^{-14} cm^3 s^{-1} for 5CzBN, and k_{STA} = 3.5 × 10^{-11} cm^3 s^{-1} and k_{TTA} = 6.0 × 10^{-14} cm^3 s^{-1} for 3Cz2DPhCzBN were obtained. Although k_{STA} and k_{TTA} of the OLEDs with 5CzBN and 3Cz2DPhCzBN are quite similar and the calculated N_T of 3Cz2DPhCzBN-OLEDs is slightly decreased compared with that of 5CzBN-OLEDs (**Fig. 2-8b**), the operational stabilities are significantly different.

Since such a large lifetime enhancement cannot be explained by only the increase of k_{RISC} according to calculation results based on STA and TTA models, I suspected a shifting of the carrier recombination zone in the EMLs plays a role. In fact, although the HOMO (−6.1 eV for both) and LUMO (−3.3 eV for 5CzBN and −3.4 eV for 3Cz2DPhCzBN) levels of both molecules are almost the same, the driving voltage of the 3Cz2DPhCzBN-based OLED was slightly higher than that of the

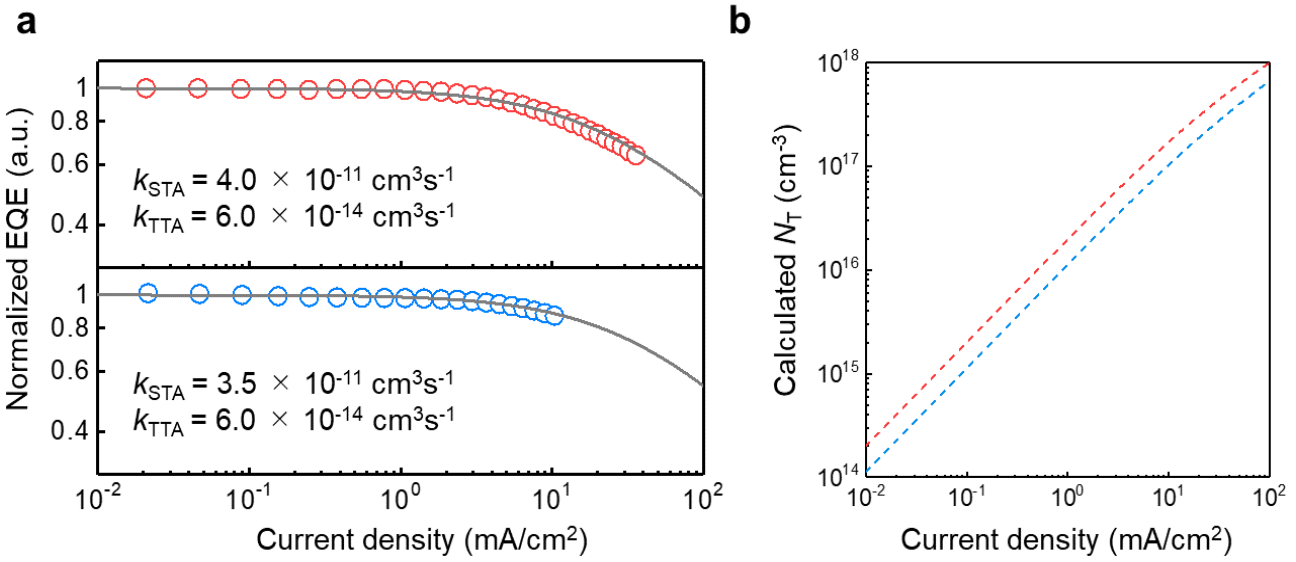

Figure 2-8 (**a**) EQE as a current density for 5CzBN (upper) and 3Cz2DPhCzBN (below). The lines correspond to the calculated EQE based on the STA and TTA models. (**b**) Calculated N_T of 5CzBN (red line) and 3Cz2DPhCzBN (blue line) using the rate equations (10) and (11) based on STA and TTA models.

5CzBN device (**Fig. 2-7d**). To check the carrier transport abilities of both EMLs, I analyzed the current density (*J*)–voltage (*V*) characteristics in electron-only devices (EOD) and hole-only devices (HOD) based on emitter: mCBP co-deposited films. I found a reduction of electron current in the 3Cz2DPhCzBN-based EOD compared to the 5CzBN device while the hole currents were similar (**Fig. 2-7d**), indicating that the introduction of a bulky substituent might be preventing carrier transport because of weaker molecular interactions between neighboring molecules. Since the HOMO level of the guest is similar to that of mCBP host, injected holes are expected to be mainly transported through the HOMO level of mCBP, resulting in the choice of guest having no effect on the hole current. Next, I evaluated EQE characteristic in the 5CzBN-based OLED without an electron blocking layer (EBL, mCBP layer (T_1: 2.90 eV)) (**Fig. 2-9**). In this device, significant decrease of EQE was observed even under low current density. This observation means that the charge recombination zone is mainly located near the HTL/EML interface, leading to the triplet excitons quenching by TrisPCz layer which has lower triplet energy level (2.70 eV) than that of 5CzBN (2.77 eV). Thus, the reduced electron transport ability in the 3Cz2DPhCzBN-based OLED can be expected to result in an expansion of carrier recombination zone inside the EML, leading to the reduction of the n_T in the device during

electrical excitation (*22*). In addition, Zhang et al. reported that the operational stability increases by introducing the substitution in Cz units such as a *tert*-butyl unit according to the enhancement of electrochemical stability (*23*). Thus, I strongly believe that the dramatic enhancement of operational lifetime in the 3Cz2DPhCzBN-based OLED originates from a combination of the increase in k_{RISC}, an expansion of the carrier recombination zone and the contribution of the substitution effect of Cz units.

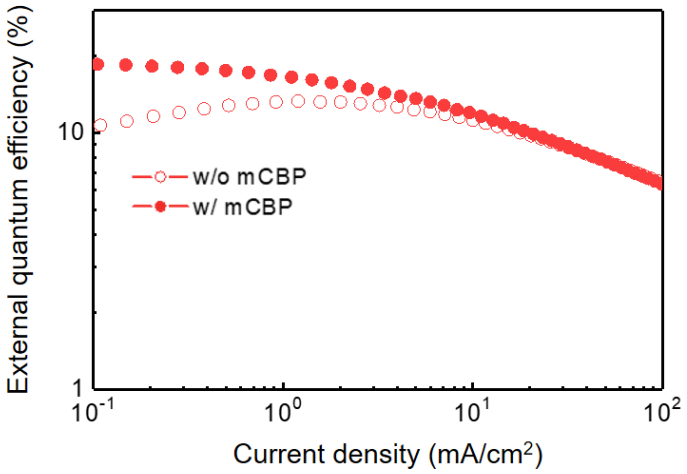

Figure 2-9 EQE–current density in the OLEDs with 5CzBN as emitter. Filled circles represent OLEDs with an mCBP layer between the ETL and EML, and open circles represent OLEDs without an mCBP layer.

2-3. Conclusion

I found that the introduction a D_2 into a D-A system can be used to tune the energy position of $^3LE_1$ relative to $^1CT_1$ and $^3CT_1$ while at the same time weakly pinning the $^1CT_1$ and $^3CT_1$ energy levels to those of the original D-A system, resulting in an increase of k_{RISC} according to a strong second-order spin-vibrionic coupling between $^3LE_1$ and $^3CT_1$. In addition, the $^3LE_1$ can be adjusted by changing the number or donor ability of the D_2 units. Further, I also found that the carrier transport properties in the EML can tuned by use of a bulky substituent, resulting in a change in the position and width of the carrier recombination zone. Thus, hetero donor molecular design is useful for boosting OLED performance, especially for blue TADF emitters, and will aid the development of future displays and lighting with high EL efficiencies and long operational lifetimes.

2-4. Materials and Methods

2-4-1. Measurement of photoluminescence properties

PLQY was measured under the flow of argon gas using an absolute PL quantum yield measurement system (C11347-01, Hamamatsu Photonics) with an excitation wavelength of 340 nm. Emission lifetimes were measured using a fluorescence lifetime measurement system (C11367-03 Quantaurus-Tau, Hamamatsu Photonics) and CoolSpek Cs-0296 (UNISOKU Co.). UV–vis absorption spectra and PL spectra were recorded on UV–vis (Perkin-Elmer Lambda 950-PKA) and PL (FluoroMax-4, Horiba Jobin Yvon)) spectrophotometers. Phosphorescence spectra in solution at 77 K were recorded on a Hamamatsu Photonics multichannel analyzer (PMA-12).

2-4-2. Device fabrication and characterization of OLED performance

Schematic diagrams of the energy levels of the fabricated devices and the chemical structures of the organic semiconductor materials used in them are presented in **Fig. 2-10**. Glass substrates with a pre-patterned, 50 or 100-nm-thick, tin-doped indium oxide (ITO) coating were used as anodes. Hole injection material dipyrazino[2,3-f:20,30-h]quinoxaline-2,3,6,7,10,11-hexacarbonitrile (HAT-CN), the hole transport material 9,9’,9”-triphenyl-9H,9’H,9”H-3,3’:6’,3”-tercarbazole (TrisPCz) and the host 3,3-di(9H-carbazol-9-yl)biphenyl (mCBP) use in the TADF-OLED devices. The HATCN, TrisPCz and mCBP were purchased from NARD institute, Ltd. The SF3-TRZ was developed in our labratory (*26*) and used as a hole blocking and electron transport material. Organic layers were formed by thermal evaporation. Doped emissive layers were deposited by co-evaporation. The bilayer of 2-nm LiQ / 100-nm Al was used as cathode.

To confirm unipolar carrier transport ability of the EML, I also fabricated an EOD (100-nm ITO / 30-nm ETM-001 / 30-nm dopant (20 wt.%):mCBP / 10-nm SF3-TRZ / 40-nm LiQ:SF3-TRZ / 2-nm LiQ / 100-nm Al) and a HOD (100-nm ITO / 10-nm HATCN / 30-nm TrisPCz / 30-nm dopant (20 wt.%):mCBP / 30-nm TrisPCz / 10-nm HATCN / 100-nm Al). After device fabrication, devices were immediately encapsulated with glass lids using epoxy glue in a nitrogen-filled glove box (O_2 <

0.1 ppm, H_2O < 0.1 ppm). Commercial calcium oxide desiccant (Dynic Co.) was included in each encapsulated package. The current density–voltage–luminance characteristics of the OLEDs were evaluated using a source meter (Keithley 2400, Keithley Instruments Inc.) and an absolute external quantum efficiency measurement system (C9920-12, Hamamatsu Photonics). The operational lifetime was measured using a luminance meter (SR-3AR, TOPCON) with the devices operated at a constant DC current. All measurements were performed in ambient atmosphere at room temperature.

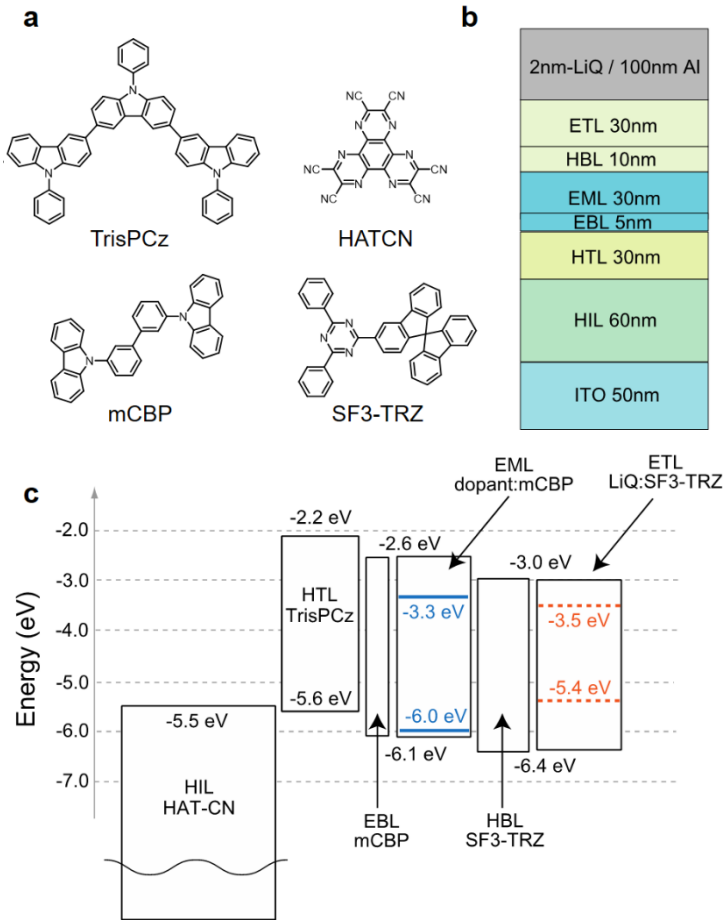

Figure 2-10 (**a**) Chemical strucutures of HATCN, TrisPCz, mCBP and SF3-TRZ (**b**) TADF-OLED structure used in this study. (**c**) HOMO and LUMO energy level diagram of the fabricated TADF-OLEDs. The solid blue lines and dashed orange lines represent the HOMO and LUMO energies of 3Cz2DPhCzBN and LiQ, respectively. HOMO levels were measured by photoelectron spectroscopy method using a Riken Keiki, AC-3. Optical energy gaps of these materials were obtained from the absorption edges of films.

2-4-3. Synthesis and characterization

2,3,4,5,6-penta(9H-carbazol-9-yl)benzonitrile (5CzBN), 2,4,6-tris(9H-carbazol-9-yl)-3,5-difluorobenzonitrile (3CzFBN), 2,3,4,6-tetrakis(9H-carbazol-9-yl)-5-fluorobenzonitrile (4CzFBN), and 3,6,9-triphenylcarbazole (1DPhCzPh) were synthesized according to literature. (*27-29*).

2,4,6-tris(9H-carbazole-9-yl)-3,5-bis(3,6-diphenylcarbazole-9-yl)benzonitrile (3Cz2DPhCzBN)

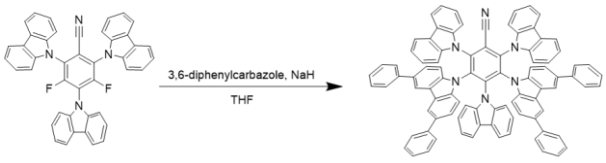

3CzFBN 3Cz2DPhCzBN

First, 3,6-diphenylcarbazole (1.0 g, 3.15 mmol) was added to a dispersion of sodium hydride (60% in mineral oil 0.13 g, 3.15 mmol) in anhydrous THF (20 ml) at 0 °C. After stirring for 30 min, 3CzFBN (0.80 g, 1.26 mmol) was added to the mixed solution under argon atmosphere. The reaction mixture was stirred at 50 °C overnight. The reaction mixture was quenched with water and the precipitate was filtered and washed with water and methanol. The obtained solid was purified by column chromatography on silica gel (toluene:hexane, 3:2 v/v) and then reprecipitated from toluene/ethanol to produce 3Cz2DPhCzBN as yellow powder (1.36 g, 1.10 mmol, 87%).

^{1}H NMR: (500 MHz, acetone-d_6): δ (ppm) = 7.82 (m, 14H), 7.72 (d, J = 8.7 Hz, 4H), 7.45 (m, 8H), 7.35 (m, 10H), 7.26 (t, J = 8.6 Hz, 4H), 7.16 (t, J = 8.3 Hz, 4H), 7.10 (t, J = 7.9 Hz, 4H), 6.98 (d, J = 8.6 Hz, 4H), 6.75 (m, 4H)

^{13}C NMR: (125 MHz, $CDCl_3$): δ (ppm) = 141.75, 141.39, 140.49, 138.99, 137.99, 137.94, 136.73, 133.99, 128.66, 127.03, 126.64, 125.49, 124.75, 124.43, 124.28, 124.06, 123.88, 121.28, 120.91, 120.35, 119.78, 118.06, 117.11, 112.80, 110.72, 110.65, 110.41

MS (MALDI-TOF MS): m/z 1233.24 $[M+H]^+$, (1232.46 calcd for $C_{91}H_{56}N_6$)

Elemental analysis: calcd. for $C_{91}H_{56}N_6$: C, 88.61; H, 4.58; N, 6.81; found: C, 88.39; H, 4.50; N, 6.84.

2,4,6-tris(9H-carbazole-9-yl)-3,5-bis(3,6-dimethylcarbazole-9-yl)benzonitrile (3Cz2DMeCzBN)

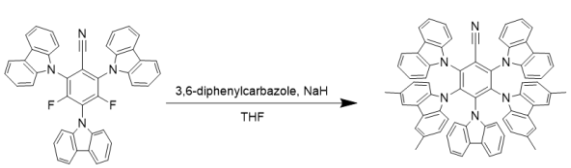

3CzFBN 3Cz2DMeCzBN

First, 3,6-dimethylcarbazole (0.39 g, 1.98 mmol) was added to a dispersion of sodium hydride (60% in mineral oil 0.08 g, 1.98 mmol) in anhydrous THF (20 ml) at 0 °C. After stirring for 30 min, 3CzFBN (0.50 g, 0.79 mmol) was added to the mixed solution under argon atmosphere. The reaction mixture was stirred at 50 °C overnight. The reaction mixture was quenched with water and

the precipitate was filtered and washed with water and methanol. The obtained solid was purified by column chromatography on silica gel (toluene:hexane, 3:2 v/v) and then reprecipitated from toluene/ethanol to produce 3Cz2DMeCzBN as yellow powder (0.79 g, 0.75 mmol, 95%).

^{1}H NMR: (500 MHz, acetone-d_6): δ (ppm) = 7.83 (d, J = 8.2 Hz, 4H), 7.71 (d, J = 7.1 Hz, 4H), 7.64 (d, J = 8.3 Hz, 2H), 7.45 (d, J = 8.4 Hz, 2H), 7.34 (d, J = 7.2 Hz, 2H), 7.09 (m, 12H), 6.72 (t, J = 7.9 Hz, 2H), 6.62 (d, J = 8.4 Hz, 2H), 6.45 (d, J = 8.3 Hz, 4H), 2.11 (s, 12H)

^{13}C NMR: (125 MHz, $CDCl_3$): δ (ppm) = 139.84, 139.04, 137.89, 137.06, 136.31, 129.48, 125.30, 124.36, 124.08, 123.82, 123.77, 120.92, 120.45, 120.12, 119.33, 110.77, 110.37, 109.89, 21.09

MS (MALDI-TOF MS): m/z 984.48 $[M+H]^+$, (984.39 calcd for $C_{71}H_{48}N_6$)

Elemental analysis: calcd. for $C_{71}H_{48}N_6$: C, 86.56; H, 4.91; N, 8.53; found: C, 86.52; H, 4.96; N, 8.52.

2,3,4,6-tetrakis(9H-carbazole-9-yl)-5-(3,6-diphenylcarbazole-9-yl)benzonitrile (4Cz1DPhCzBN)

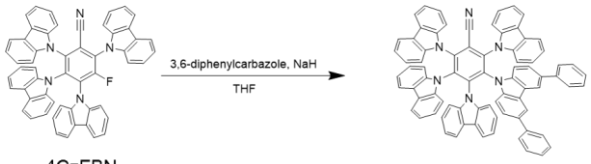

First, 3,6-diphenylcarbazole (0.61 g, 1.92 mmol) was added to a dispersion of sodium hydride (60% in mineral oil 0.08 g, 1.92 mmol) in anhydrous THF (20 ml) at 0 °C. After stirring for 30 min, 4CzFBN (1.0 g, 1.28 mmol) was added to the mixed solution under argon atmosphere. The reaction mixture was stirred at 50 °C overnight. The reaction mixture was quenched with water and the precipitate was filtered and washed with water and methanol. The obtained solid was purified by column chromatography on silica gel (toluene:hexane, 3:2 v/v) and then reprecipitated from toluene/ethanol to produce 4Cz1DPhCzBN as yellow powder (1.18 g, 1.09 mmol, 85%).

^{1}H NMR: (500 MHz, acetone-d_6): δ (ppm) = 7.82 (m, 8H), 7.75 (m, 4H), 7.67 (t, J = 7.8 Hz, 4H), 7.45 (m, 4H), 7.35 (m, 8H), 7.25 (t, J = 8.0 Hz, 2H), 7.11 (m, 8H), 6.95 (d, J = 8.6 Hz, 2H), 6.74 (m, 4H), 6.66 (t, J = 7.8 Hz, 4H)

^{13}C NMR: (125 MHz, $CDCl_3$) : δ (ppm) = 141.67, 141.40, 140.38, 139.00, 138.87, 137.93, 137.84, 137.72, 136.64, 136.55, 133.93, 128.65, 127.02, 126.62, 125.46, 125.39, 124.58, 124.39, 124.36, 124.25, 124.13, 123.91, 123.84, 123.68, 121.22, 121.17, 120.79, 120.50, 120.32, 120.23, 119.61, 119.45, 118.02, 116.95, 112.79, 110.71, 110.66, 110.39, 110.26

MS (MALDI-TOF MS): m/z 1081.22 [M+H]+, (1080.39 calcd for $C_{79}H_{48}N_6$)

Elemental analysis: calcd. for $C_{79}H_{48}N_6$: C, 87.75; H, 4.47; N, 7.77; found: C, 87.84; H, 4.46; N, 7.72.

2,4,6-tris(3,6-diphenylcarbazole-9-yl)-3,5-difluorobenzonitrile (2F3DPhCzBN)

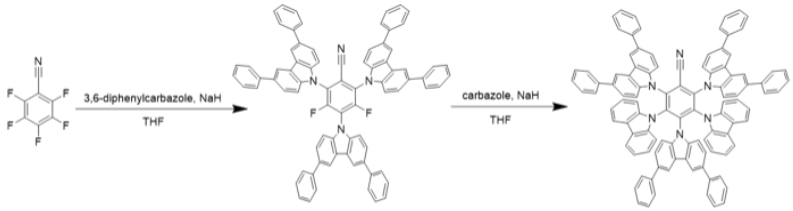

First, 3,6-diphenylcarbazole (1.0 g, 3.13 mmol) was added to a dispersion of sodium hydride (60% in mineral oil 0.13 g, 3.13 mmol) in anhydrous THF (20 ml) at 0 °C. After stirring for 30 min, 2,3,4,5,6-pentafluorobenzonitrile (0.20 g, 1.04 mmol) was added to the mixed solution under argon atmosphere. The reaction mixture was stirred at room temperature overnight. The reaction mixture was quenched with water and the precipitate was filtered and washed with water and methanol. The obtained solid was purified by column chromatography on silica gel (chloroform:hexane, 2:3 v/v) and then reprecipitated from chloroform/ethanol to produce 2F3DPhCzBN as yellow powder (0.34 g, 0.31 mmol, 30%).

^{1}H NMR: (500 MHz, $CDCl_3$): δ (ppm) = 8.46 (s, 4H), 8.41 (s, 2H), 7.87 (d, *J* = 8.5 Hz, 4H), 7.87 (d, *J* = 8.5 Hz, 2H), 7.77 (d, *J* = 8.3 Hz, 8H), 7.73 (d, *J* = 8.2 Hz, 4H), 7.53 (m, 16H), 7.44 (m, 8H)

^{13}C NMR: (125 MHz, $CDCl_3$): δ (ppm) = 141.40, 141.19, 139.94, 139.11, 135.90, 135.75, 128.91, 128.90, 127.48, 127.41, 127.14, 127.06, 126.55, 126.49, 125.31, 125.15, 119.71, 119.40, 110.44, 109.80.

MS (MALDI-TOF MS): m/z 1091.41 [M+H]+, (1090.38 calcd for $C_{79}H_{48}F_2N_4$)

2,4,6-tris(3,6-diphenylcarbazole-9-yl)-3,5-(9H-carbazole-9-yl)benzonitrile (2Cz3DPhCzBN)

Carbazole (0.14 g, 0.84 mmol) was added to a dispersion of sodium hydride (60% in mineral oil 0.03 g, 0.84 mmol) in anhydrous THF (10 ml) at 0 °C. After stirring for 30 min, 2F3PhCzBN (0.3 g, 0.28 mmol) was added to the mixed solution under argon atmosphere. The reaction mixture was stirred at 50 °C overnight. The reaction mixture was quenched with water and the precipitate was filtered and washed with water and methanol. The obtained solid was purified by column chromatography on silica gel (toluene:hexane, 4:1 v/v) and then reprecipitated from chloroform/ethanol to produce 2Cz3DPhCzBN as yellow powder (0.33 g, 0.24 mmol, 85%).

^{1}H NMR: (500 MHz, $CDCl_3$): δ (ppm) = 8.30 (s, 4H), 8.41 (d, *J* = 8.6 Hz, 4H), 7.80 (m, 8H), 7.87 (d, *J* = 8.5 Hz, 2H), 7.66 (d, *J* = 8.3 Hz, 8H), 7.45 (m, 20H), 7.32 (m, 8H), 7.23 (t, *J* = 7.9 Hz, 8H), 6.95 (d, *J* = 8.6 Hz, 2H), 6.80 (m, 8H)

^{13}C NMR: (125 MHz, $CDCl_3$): δ (ppm) = 141.51, 141.21, 140.49, 138.96, 137.94, 136.66, 134.84, 134.21, 128.75, 128.61, 127.28, 126.98, 126.79, 126.65, 125.01, 124.84, 124.59, 124.00, 120.73, 119.70, 118.87, 118.11, 111.10, 110.83, 110.30.

MS (MALDI-TOF MS): m/z 1385.17 $[M+H]^+$, (1384.52 calcd for $C_{103}H_{64}N_6$)

Elemental analysis: calcd. for $C_{103}H_{64}N_6$: C, 89.28; H, 4.66; N, 6.07; found: C, 89.33; H, 4.65; N, 6.02.

penta(9H-carbazole-9-yl)benzene (5CzPh)

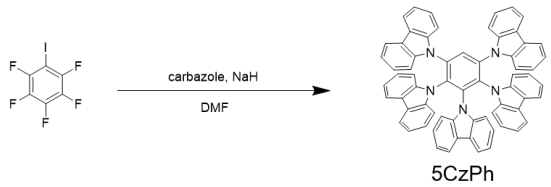

Carbazole (3.98 g, 23.8 mmol) was added to a dispersion of sodium hydride (60% in mineral oil 0.95 g, 23.8 mmol) in anhydrous DMF (60 ml) at 0 °C. After stirring for 30 min, pentafluoroiodobenzene (1.0 g, 3.40 mmol) was added to the mixed solution under argon atmosphere. The reaction mixture was stirred at 150 °C overnight. The reaction mixture was quenched with water and the precipitate was filtered and washed with water and methanol. The obtained solid was purified by column chromatography on silica gel (toluene) and then reprecipitated from toluene/ethanol to produce 5CzPh as white powder (1.93 g, 2.13 mmol, 63%).

^{1}H NMR: (500 MHz, acetone-d_6): δ (ppm) = 8.60 (s, 1H), 7.84 (m, 4H), 7.69 (m, 4H), 7.55 (d, J = 8.2 Hz, 4H), 7.51 (d, J = 8.3 Hz, 2H), 7.39 (d, J = 7.6 Hz, 4H), 7.32 (d, J = 7.5 Hz, 2H), 7.03 (m, 8H), 6.68 (m, 10H), 6.57 (t, J = 8.1 Hz, 2H)

^{13}C NMR: (125 MHz, $CDCl_3$): δ (ppm) = 139.46, 138.21, 137.15, 137.00, 133.53, 130.37, 125.55, 124.41, 124.21, 123.73, 123.53, 123.46, 120.55, 120.06, 119.99, 119.90, 119.35, 119.23, 110.42, 110.26, 109.86

MS (MALDI-TOF MS): m/z 905.09 $[M+H]^+$, (903.34 calcd for $C_{66}H_{41}N_5$)

Elemental analysis: calcd. for $C_{66}H_{41}N_5$: C, 87.68; H, 4.57; N, 7.75; found: C, 87.91; H, 4.56; N, 7.73.

1,3-bis(3,6-diphenylcarbazole-9-yl)benzene (2DPhCzPh)

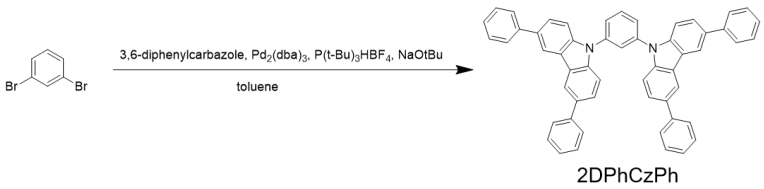

A mixture of 1,3-dibromobenzene (1.0 g, 4.24 mmol), 3,6-diphenylcarbazole (2.94 g, 9.33 mmol), tris(dibenzylideneacetone)dipalladium (0.19 g, 0.21 mmol), tri-*tert*-butylphosphonium tetrafluoroborate (0.25 g, 0.85 mmol) and sodium *tert*-butoxide (1.22 g, 12.7 mmol) in 50 ml of toluene was heated and stirred at 120°C for 12 h. After cooling, the mixture was partitioned between chloroform and water. The organic layer was separated, and the aqueous layer was extracted with the chloroform. The combined organic layers were washed with brine and dried over Mg_2SO_4. The crude product was purified by column chromatography on silica gel ($CHCl_3$) and then recrystallized from acetone and methanol to yield 2DPhCzPh as a white solid (2.6 g, 3.64 mmol, 86%).

^{1}H NMR: (500 MHz, $CDCl_3$): δ (ppm) = 8.42 (s, 4H), 7.93 (m, 2H), 7.79 (d, J = 7.9 Hz, 2H), 7.73 (m, 12H), 7.65 (d, J = 8.5 Hz, 4H), 7.49 (t, J = 7.8 Hz, 8H), 7.36 (t, J = 7.4 Hz, 4H)

^{13}C NMR: (125 MHz, $CDCl_3$): δ (ppm) = 141.74, 140.48, 139.40, 134.16, 131.44, 128.33, 127.35, 126.74, 125.93, 125.74, 124.95, 124.32, 119.05, 110.11

MS (FD-MS): m/z 712.23 [M]•, (712.29 calcd for $C_{54}H_{36}N_2$)

Elemental analysis: calcd. for $C_{54}H_{36}N_2$: C, 90.98; H, 5.09; N, 3.93; found: C, 90.92; H, 5.09; N, 3.87.

1,3-bis(3,6-dimethylcarbazole-9-yl)benzene (2DMeCzPh)

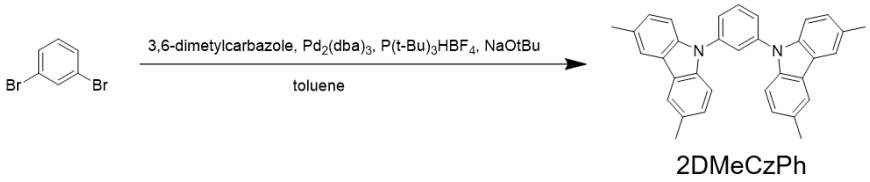

2DMeCzPh

A mixture of 1,3-dibromobenzene (2.00 g, 8.48 mmol), 3,6-dimethylcarbazole (3.64 g, 18.7 mmol), tris(dibenzylideneacetone)dipalladium (0.388 g, 0.424 mmol), tri-*tert*-butylphosphonium tetrafluoroborate (0.492 g, 1.70 mmol) and sodium *tert*-butoxide (2.44 g, 25.4 mmol) in 100 ml of toluene was heated and stirred at 120°C for 24 h. After cooling, the mixture was partitioned between chloroform and water. The organic layer was separated, and the aqueous layer was extracted with the chloroform. The combined organic layers were washed with brine and dried over Mg_2SO_4. The crude product was purified by column chromatography on silica gel (toluene) and then recrystallized from acetone and methanol to yield 2DMeCzPh as a white solid (3.01 g, 6.48 mmol, 76%).

^{1}H NMR: (500 MHz, $CDCl_3$): δ (ppm) = 7.90 (s, 4H), 7.77 (m, 2H), 7.63 (d, J = 7.9 Hz, 2H), 7.41 (d, J = 8.4 Hz, 4H), 7.22 (d, J = 8.4 Hz, 4H), 2.54 (s, 12H)

^{13}C NMR: (125 MHz, $CDCl_3$): δ (ppm) = 139.69, 139.04, 130.94, 129.47, 127.22, 125.03, 124.62, 123.62, 120.27, 109.39, 21.38

MS (FD-MS): m/z 464.22 [M]•, (464.23 calcd for $C_{34}H_{28}N_2$)

Elemental analysis: calcd. for $C_{34}H_{28}N_2$: C, 87.90; H, 6.07; N, 6.03; found: C, 88.05; H, 6.11; N, 6.09.

1,3,5-tris(3,6-diphenylcarbazole-9-yl)benzene (3DPhCzPh)

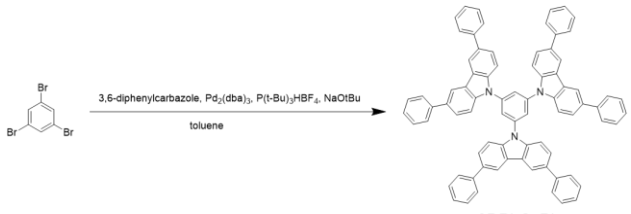

3DPhCzPh

A mixture of 1,3,5-tribromobenzene (0.5 g, 1.59 mmol), 3,6-diphenylcarbazole (1.78 g, 5.57 mmol), tris(dibenzylideneacetone)dipalladium (0.16 g, 0.15 mmol), tri-*tert*-butylphosphonium tetrafluoroborate (0.19 g, 0.64 mmol) and sodium *tert*-butoxide (1.37 g, 14.3 mmol) in 30 ml of toluene was heated and stirred at 120°C for 12 h. After cooling, the mixture was partitioned between chloroform and water. The organic layer was separated, and the aqueous layer was extracted with the chloroform. The combined organic layers were washed with brine and dried over Mg_2SO_4. The crude

product was purified by column chromatography on silica gel (toluene:hexane, 3:7 v/v) and then reprecipitated from toluene/ethanol to produce 3DPhCzPh as a white powder (0.5 g, 0.49 mmol, 30%).

^{1}H NMR: (500 MHz, $CDCl_3$): δ (ppm) = 8.45 (s, 6H), 8.11 (m, 2H), 7.76 (m, 24H), 7.49 (t, *J* = 7.7 Hz, 12H), 7.38 (t, *J* = 7.4 Hz, 6H)

^{13}C NMR: (125 MHz, $CDCl_3$): δ (ppm) = 141.57, 140.96, 140.18, 134.66, 128.87, 127.37, 126.88, 126.16, 124.63, 123.11, 119.23, 110.12

MS (MALDI-TOF MS): m/z 1030.48 $[M+H]^+$, (1029.41calcd for $C_{78}H_{51}N_3$)

Elemental analysis: calcd. for $C_{78}H_{51}N_3$: C, 90.93; H, 4.99; N, 4.08; found: C, 91.12; H, 5.01; N, 4.08.

References

1. Baldo, M. A., O'Brien, D. F., Thompson, M. E., Forrest, S. R., Excitonic singlet-triplet ratio in a semiconducting organic thin film. *Phys. Rev. B*, **60**, 14422-14428 (1999).

2. Baldo, M. A., O'Brien, D. F., You, Y., Shoustikov, A., Sibley, S., Thompson, M. E., Forrest, S. R., Highly efficient phosphorescent emission from organic electroluminescent devices. *Nature*, **395**, 151-154 (1998).

3. Reineke, S., Lindner, F., Schwartz, G., Seidler, N., Walzer, K., Lüssem, B., Leo, K., White organic light-emitting diodes with fluorescent tube efficiency. *Nature*, **459**, 234-238 (2009).

4. Endo, A., Ogasawara, M., Takahashi, A., Yokoyama, D., Kato, Y., Adachi, C., Thermally Activated Delayed Fluorescence from Sn^{4+}–Porphyrin Complexes and Their Application to Organic Light Emitting Diodes — A Novel Mechanism for Electroluminescence. *Adv. Mater.*, **21**, 4802-4806 (2009).

5. Wong, M. Y., Zysman-Colman, E., Purely Organic Thermally Activated Delayed Fluorescence Materials for Organic Light-Emitting Diodes. *Adv. Mater.*, **29**, 1605444 (2017).

6. Uoyama, H., Goushi, K., Shizu, K., Nomura, H., Adachi, C., Highly efficient organic light-emitting diodes from delayed fluorescence. *Nature*, **492**, 234-238 (2012).

7. Hirata, S., Sakai, Y., Masui, K., Tanaka, H., Lee, S. Y., Nomura, H., Nakamura, N., Yasumatsu, M., Nakanotani, H., Zhang, Q., Shizu, K., Miyazaki, H., Adachi, C., Highly efficient blue electroluminescence based on thermally activated delayed fluorescence. *Nat. Mater.*, **14**, 330-336 (2015).

8. Lin, T. A., Chatterjee, T., Tsai, W. L., Lee, W. L., Wu, M. J., Jiao, M., Pan, K. C., Yi, C. L., Chung, C. L., Wong, K. T., Wu, C. C., Sky-Blue Organic Light Emitting Diode with 37% External Quantum Efficiency Using Thermally Activated Delayed Fluorescence from Spiroacridine-Triazine Hybrid. *Adv. Mater.*, **28**, 6976-6983 (2016).

9. Nakanotani, H., Higuchi, T., Furukawa, T., Masui, K., Morimoto, K., Numata, M., Tanaka, H., Sagara, Y., Yasuda. T., Adachi, C., High-efficiency organic light-emitting diodes with fluorescent emitters. *Nat. Commun.*, **5**, 4016-4023 (2014).

10. Furukawa, T., Nakanotani, H., Adachi, C., Dual enhancement of electroluminescence efficiency and operational stability by rapid upconversion of triplet excitons in OLEDs. *Sci. Rep*., **5**, 8429 (2015).

11. Masui, K., Nakanotani, H., Adachi, C., Analysis of exciton annihilation in high-efficiency sky-blue organic light-emitting diodes with thermally activated delayed fluorescence. *Org. Electron*., **14**, 2721-2726 (2013).

12. Schmidbauer, S., Hohenleutner, A., König, B., Chemical Degradation in Organic Light-Emitting Devices: Mechanisms and Implications for the Design of New Materials. *Adv. Mater*., **25**, 2114-2129 (2013).

13. Nakanotani, H., Masui, K., Nishide, J., Shibata, T., Adachi, C., Promising operational stability of high-efficiency organic light-emitting diodes based on thermally activated delayed fluorescence. *Sci*. *Rep*., **3**, 2127 (2013)

14. Turro, N. J., Ramamurthy, V., Scaiano, J. C., Principle of Molecular Photochemistry: An Introduction. Chapter **3**, p.113–118 (University Science Books, 2009).

15. Chen, X. K., Zhang, S. F., Fan, J. X., Ren, A. M., Nature of Highly Efficient Thermally Activated Delayed Fluorescence in Organic Light-Emitting Diode Emitters : Nonadiabatic Effect between Excited States. *J*. *Phys*. *Chem*. *C*, **119**, 9728-9733 (2015).

16. Gibson, J., Monkman, A. P., Penfold, T. J., The Importance of Vibronic Coupling for Efficient Reverse Intersystem Crossing in Thermally Activated Delayed Fluorescence Molecules. *ChemPhysChem*, **17**, 2956-2961 (2016).

17. Dias, F. B., Santos, J., Graves, D. R., Data, P., Nobuyasu, R. S., Fox, M. A., Batsanov, A. S., Palmeira, T., Berberan-Santos, M. N., Bryce, M. R., Monkman, A. P., The Role of Local Triplet Excited States and D-A Relative Orientation in Thermally Activated Delayed Fluorescence: Photophysics and Devices. *Adv. Sci*., **3**, 1600080 (2016).

18. Marian, C. M., Mechanism of the Triplet-to-Singlet Upconversion in the Assistant Dopant ACRXTN. *J. Phys. Chem. C*, **120**, 3715-3721 (2016).

19. Hosokai, T., Matsuzaki, H., Nakanotani, H., Tokumaru, K., Tsutsui, T., Furube, A., Nasu, K., Nomura, H., Yahiro, M., Adachi, C., Evidence and Mechanism of Efficient Thermally Activated Delayed Fluorescence Promoted by Delocalized Excited States. *Sci. Adv*., **3**, e1603282 (2017).

20. Gibson, J., Penfold, T.J., Nonadiabatic coupling reduces the activation energy in thermally activated delayed fluorescence. *Phys*. *Chem*. *Chem*. *Phys*., **19**, 8248-8434 (2017).

21. Erickson, N. C., Holmes, R. J., Investigating the Role of Emissive Layer Architecture on the Exciton Recombination Zone in Organic Light-Emitting Devices. *Adv. Mater*., **23**, 5190-5198 (2013).

22. Zhang, Y., Lee, J., Forrest, S. R., Tenfold increase in the lifetime of blue phosphorescent organic light-emitting diodes, *Nat*. *Comm*., **5**, 5008 (2014).

23. Zhang, D. D., Cai, M. H., Zhang, Y. G., Zhang, D. Q., Duan, L., Sterically shielded blue thermally activated delayed fluorescence emitters with improved efficiency and stability. *Mater. Horiz*., **3**, 145-151 (2016).

24. Takei, K., Kanda, Y., Phosphorescence spectra of benzonitrile and related compounds. *Spectchim. Acta*, **18**, 1201-1216 (1962).

25. Hosokai, T., Noda, H., Nakanotani, H., Nawata, T., Nakayama, Matsuzaki, H., Adachi, C., Solvent-dependent investigation of carbazole benzonitrile derivatives: Does the ^{3}LE-^{1}CT energy gap facilitate TADF? *J. Photon. Energy*, **8**, 032102 (2018).

26. Cui, L-S., Ruan, S. B., Nagata, R., Zhang, L., Inada, K., Nakanotani, H., Liao, L. S., Adachi, C., Long-lived efficient delayed fluorescence organic light-emitting diodes using n-type hosts. *Nat. Comm.*, **8**, 2250 (2017).

27. Cho, Y. J., Jeon, S. K., Lee, J. Y., Molecular Engineering of High Efficiency and Long Lifetime Blue Thermally Activated Delayed Fluorescent Emitters for Vacuum and Solution Processed Organic Light-Emitting Diodes. *Adv. Opt. Mater*., **4**, 688-693 (2016).

28. Cho, Y. J., Chin, B. D., Jeon, S. K., Lee., J. Y., 20% External Quantum Efficiency in Solution-Processed Blue Thermally Activated Delayed Fluorescent Devices. *Adv. Funct. Mater*., **25**, 6786-6792 (2015).

29. Park, M., Buck, J. R., Rizzo, C. J., A Convenient Synthesis of 3,6-Substituted Carbazoles via Nickel Catalyzed Cross-Coupling. *Tetrahedron*, **54**, 12707-12714 (1998).

Chapter 3

Highly efficient thermally activated delayed fluorescence with slow reverse intersystem crossing

Hiroki Noda, Hajime Nakanotani, & Chihaya Adachi
Chemistry Letters, (DOI:10.1246/cl.180813).

Abstract

I show an efficient luminescent molecule exhibiting TADF with a long-delayed fluorescence lifetime of 0.8 ms. Although the k_{RISC} is small of 2.1×10^3 s^{-1}, the molecule shows a high PLQY of 89±2%, indicating the suppression of nonradiative decay from T_1 state.

3-1. Introduction

In TADF processes, triplet excitons can be harvested as DF from S_1 during multiple forward/reverse ISC cycles. Managing k_{RISC} is crucial for harvesting all triplet excitons as DF. Several groups recently reported the influence on reverse ISC by $\Delta E_{S1\text{-}T1}$ and also by spin-vibronic coupling between a ^{3}LE state and a ^{3}CT state (*1-5*). These results indicated that for a fast reverse ISC process, the $|\Delta E_{3LE\text{-}3CT}|$ must be small, in addition to the small $\Delta E_{S1\text{-}T1}$. Aligning these energy levels is therefore critical for controlling k_{RISC}.

A large k_{RISC} can be exploited in developing highly stable and low rolloff OLEDs because these undesirable characteristics strongly depend on n_T (*6,7*). Hence, developing molecules exhibiting TADF with a large k_{RISC} has been a major recent focus in OLED research (*8*). On the other hand, decreasing the k_{RISC} is likely to be beneficial for some applications. For example, the long lifetime of a triplet exciton is suitable for spatiotemporal imaging of oxygen distributions with high sensitivity (*9*). This is because triplet excitons are efficiently quenched by the presence of oxygen (*10*). TADF molecules with a small k_{RISC} are therefore promising in bio-imaging at the cellular and tissue level. In another advantage, TADF emitters also do not require costly and potentially toxic rare elements such as Ir and Eu (*11-13*). An important problem that needs to be overcome is limiting the utilization of TADF for these applications; the coexistence of a high PLQY and long emission decay time. Thus, an alternative molecular design is required (*14,15*).

In this chapter, I developed a TADF molecule with a very long τ_d (0.8 ms) and a high PLQY. This balance is achieved by controlling the $\Delta E_{S1\text{-}T1}$ and $|\Delta E_{3LE\text{-}3CT}|$. Although the k_{RISC} of the molecule is very small (2.1×10^3 s^{-1}), the molecule shows a high PLQY (89±2%). This indicates that the molecule can harvest triplet excitons as DF efficiently.

3-2. Results and discussion

3-2-1. Molecular design for slow reverse ISC process

According to the selection rules for ISC (*i.e.*, El-Sayed rule), electron transition from a pure ^{3}CT to a pure ^{1}CT is prohibited because of the vanishing SOC elements between these two states (*16*). This transition is nevertheless common in many TADF molecules. This is because molecules exhibiting TADF generally contain some D groups and A groups which induce a small $\Delta E_{S1\text{-}T1}$. Therefore, to achieve efficient reverse ISC, the intense mixing between the S and T should be achieved by reducing both the $\Delta E_{S1\text{-}T1}$ and $|\Delta E_{3LE\text{-}3CT}|$. However, to realize slow reverse ISC while maintaining a high PLQY, the intense mixing between the LE state and CT state is not required. Thus, the molecular design for slow reverse ISC involves suppressing spin-vibronic coupling between the ^{3}LE and ^{3}CT, while maintaining a small $\Delta E_{S1\text{-}T1}$. This in turn realizes a low probability for spin-flip between the S_1 and T_1. In addition, molecular vibration is one of the nonradiative decay pathways from T_1 to S_0, and should be suppressed to realize a high PLQY.

In this study, I used CzPh as a D unit and phenyl-dimesitylboron (BMePh) as an A unit because of the high ^{3}LE of these moieties (3.10 eV and 3.12 eV, respectively). To induce a large $|\Delta E_{3LE\text{-}3CT}|$, the CT state can be stabilized according to the formation of a CR state (*5,17,18*) between two redox sites. For this, I designed 9,9'-(2,5-bis(dimesitylboranyl)-1,4-phenylene)bis(9H-carbazole) (*p*-2Cz2BMe) that has 9,9'-(1,4-phenylene)bis-9H-

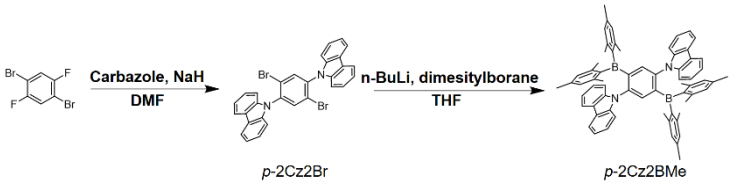

Scheme 3-1 Synthesis of *p*-2Cz2BMe.

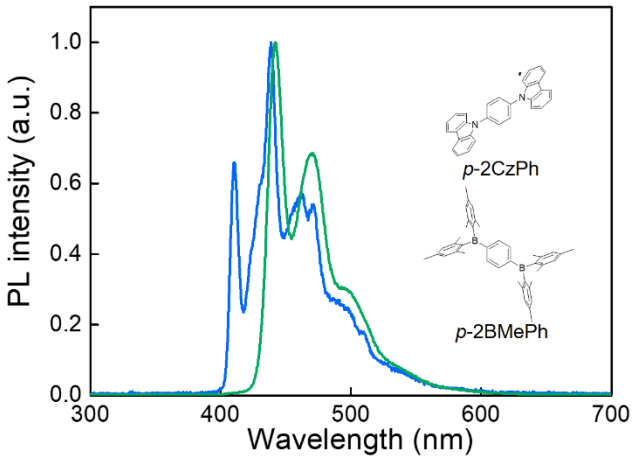

Figure 3-1 Phosphorescence spectra of *p*-2CzPh (blue) and *p*-2BMePh (green) in toluene solutions at 77 K.

carbazole (*p*-2CzPh) as a D unit and 1,4-bis(dimesitylboryl)benzene (*p*-2BMePh) unit as an A unit. *p*-2Cz2BMe was synthesized according to **Scheme 3-1**. The precursor was synthesized via nucleophilic substitution. After lithiation in THF, the reaction was treated with dimesitylboron fluoride, giving *p*-2Cz2BMe (>99% purity after vacuum sublimation). The origin of the ^{3}LE state of *p*-2Cz2BMe is considered to be the *p*-2CzPh and *p*-2BMePh units, and not the CzPh and BMePh units. The ^{3}LE values of these units still show very high energy levels (*p*-2CzPh: 3.10 eV and *p*-2BMePh: 2.93 eV) which were obtained experimentally from the onset energies of the phosphorescence spectra in diluted toluene solutions at 77 K (**Fig. 3-1**).

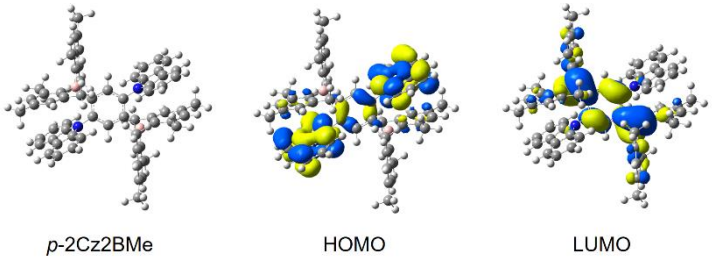

Figure 3-2 Optimized structure, HOMO and LUMO distributions of *p*-2Cz2BMe.

To gain insight into the electronic states of *p*-2Cz2BMe, the S_0, S_1, and T_1 were calculated using the Gaussian 09 program package. The S_0 geometry was optimized at the PBE0/6-31G(d) level of theory, and the S_1 and T_1 were calculated with time-dependent density functional theory (TD-DFT) and PBE0/6-31G(d) methods using the optimized S_0 geometry. **Figure 3-2** shows the optimized structures and HOMO and LUMO distributions of *p*-2Cz2BMe. The HOMO and LUMO are mainly delocalized on the D and A redox sites, respectively, indicating that *p*-2Cz2BMe can form CR states. TD-DFT calculations showed that the energy levels of the excited-state in *p*-

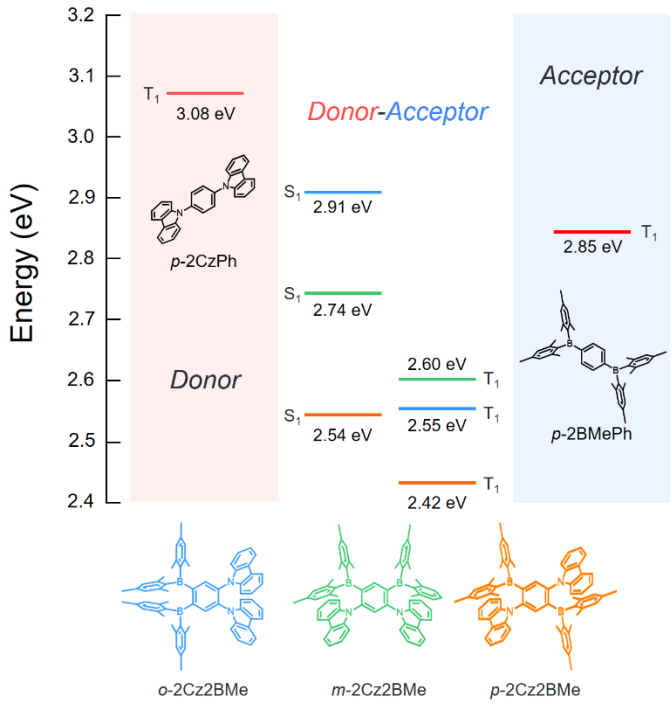

Figure 3-3 Calculated energy level diagram of the excited-state in CzBMe derivatives and D and A units. Blue: *o*-2Cz2BMe, Green: *m*-2Cz2BMe, Orange: *p*-2Cz 2BMe.

2Cz2BMe (^{1}CT : 2.54 eV and ^{3}CT : 2.42 eV) are stabilized compared with the ^{3}LE energy level (3.08 and 2.85 eV), and that the $\Delta E_{S1\text{-}T1}$ is sufficiently small (0.12 eV) to induce reverse ISC, as shown in **Fig. 3-3**. The calculations also indicated that the energy levels of *o*-2Cz2BMe and *m*-2Cz2BMe are much higher than that of *p*-2Cz2BMe (**Fig. 3-3**). This indicates that the CR formation leads to strong CT energy stabilization. Therefore, *p*-2Cz2BMe satisfies the conditions of possessing S_1 and T_1 states with similar excited-state character, a relatively small $\Delta E_{S1\text{-}T1}$, and a large$|\Delta E_{3LE\text{-}3CT}|$.

3-2-2. Fundamental photophysical properties

The fundamental photophysical properties of *p*-2Cz2BMe in 1×10^{-5} M toluene solution are summarized in **Table 3-1** and shown in **Fig. 3-4**. *p*-2Cz2BMe shows a weak and broad featureless absorption band at 400–500 nm which is assigned to the ground state CT absorption (**Fig. 3-4a**). The steady-state PL spectrum and calculation results show that the S_1 energy of *p*-2Cz2BMe (2.52 eV) is stabilized compared to the ^{3}LE energy (3.10 and 2.93 eV). The energy gap between the S_1 and ^{3}LE is quite large, so participation of the ^{3}LE to reverse ISC process is not expected. Thus, the S_1 and T_1 states of *p*-2Cz2BMe are isolated from the LE state which has different excited-state characteristics. This ensures almost no mixing of other electronic characters with the S_1 and T_1 states in *p*-2Cz2BMe. Transient PL and PLQY measurements confirm the TADF properties of *p*-2Cz2BMe in oxygen-free and oxygen-saturated 1×10^{-5} M toluene solutions, as shown in **Fig. 3-4b**. In oxygen-saturated solution, *p*-2Cz2BMe shows only single-component PL decay; *i.e*. nanosecond-scale prompt fluorescence (PF), while the PL decay curve of *p*-2Cz2BMe in oxygen-free solution shows two components; PF and DF.

Table 3-2 Photophysical properties of *p*-2Cz2BMe in toluene solution and solid-state thin film

state	PL_{max} (nm)	Φ_{PL} (%)	τ_p (ns)	τ_d (ms)	k_r ($\times10^7$ s^{-1})	k_{ISC} (10^7 s^{-1})	k_{nr}^T (10^2 s^{-1})	k_{RISC} (10^3 s^{-1})
toluene	558	20→89[*1]	45.0	0.8	1.05	1.17	2.56	2.10
film[*2]	552	94	34.9	1.1	1.67	1.19	1.31	1.34

*1: PLQY of the solution sample before / after Ar bubbling.

*2: *p*-2Cz2BMe was doped into a mCBP host matrix with doping concentration of 6 wt %.

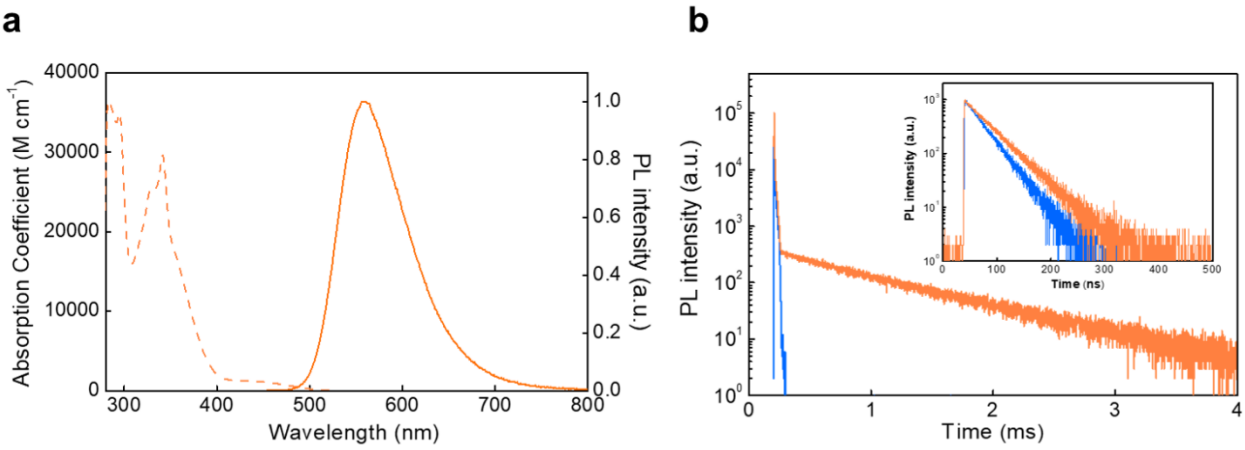

Figure 3-4 (**a**) UV-vis absorption (dashed line) and PL spectra (solid line) of *p*-2Cz2BMe in toluene solution. (**b**) PL transient decay curves of *p*-2Cz2BMe in oxygen free toluene (orange line) and air-saturated (blue line) solutions at 295 K. Inset: Expanded transient decay profile for prompt region.

The PF lifetime (τ_p) and τ_d are estimated to be 45 ns (16 ns before Ar bubbling) and 802 μs, respectively. After bubbling with Ar, the PLQY of *p*-2Cz2BMe in solution increases from 20±2% to 89±2%, indicating a high reverse ISC efficiency of 86%. The k_{RISC} and k_{ISC} of *p*-2Cz2BMe are calculated to be 2.1×10^3 s^{-1} and 1.2×10^7 s^{-1}, respectively. The k_{RISC} of *p*-2Cz2BMe is among the smallest values reported for compounds in solution state. The long decay lifetime of triplet excitons generally induces a high probability of nonradiative decay from the T_1 to S_0. However, the current results indicate that nonradiative decay from the T_1 to S_0 in *p*-2Cz2BMe is completely suppressed. The k_{nr}^T of the T_1 of *p*-2Cz2BMe in oxygen-free solution (2.6×10^2 s^{-1}) is an order of magnitude smaller than the k_{RISC} (2.1×10^3 s^{-1}).

3-2-3. Temperature dependence of ^{1}H-NMR spectrum

Molecular vibrational modes are one of the main nonradiative decay pathways from the T_1 to S_0, so should be considered. To evaluate the effect of molecular vibration on suppression of nonradiative decay, I measured the temperature dependence of ^{1}H-NMR spectra in toluene-d8 (**Fig. 3-5**). At 300 K, the ^{1}H-NMR spectrum of *p*-2Cz2BMe shows a mix of broad and sharp peaks, suggesting that some rotational modes are suppressed. Thus, *p*-2Cz2BMe shows multiple environments for the same protons. Increasing the temperature to 353 K causes some broad peaks to

sharpen. These results indicate that at high temperature, the mesityl group and carbazole ring of *p*-2Cz2BMe can be activated to rotate freely, but at room temperature a rigid and dense structure of *p*-2Cz2BMe partly prevents rotational motion of the mesityl group. This suppresses nonradiative decay from the T_1, even in solution. No significant differences in PLQY are observed in the solid-state film, as shown in **Table 3-2**.

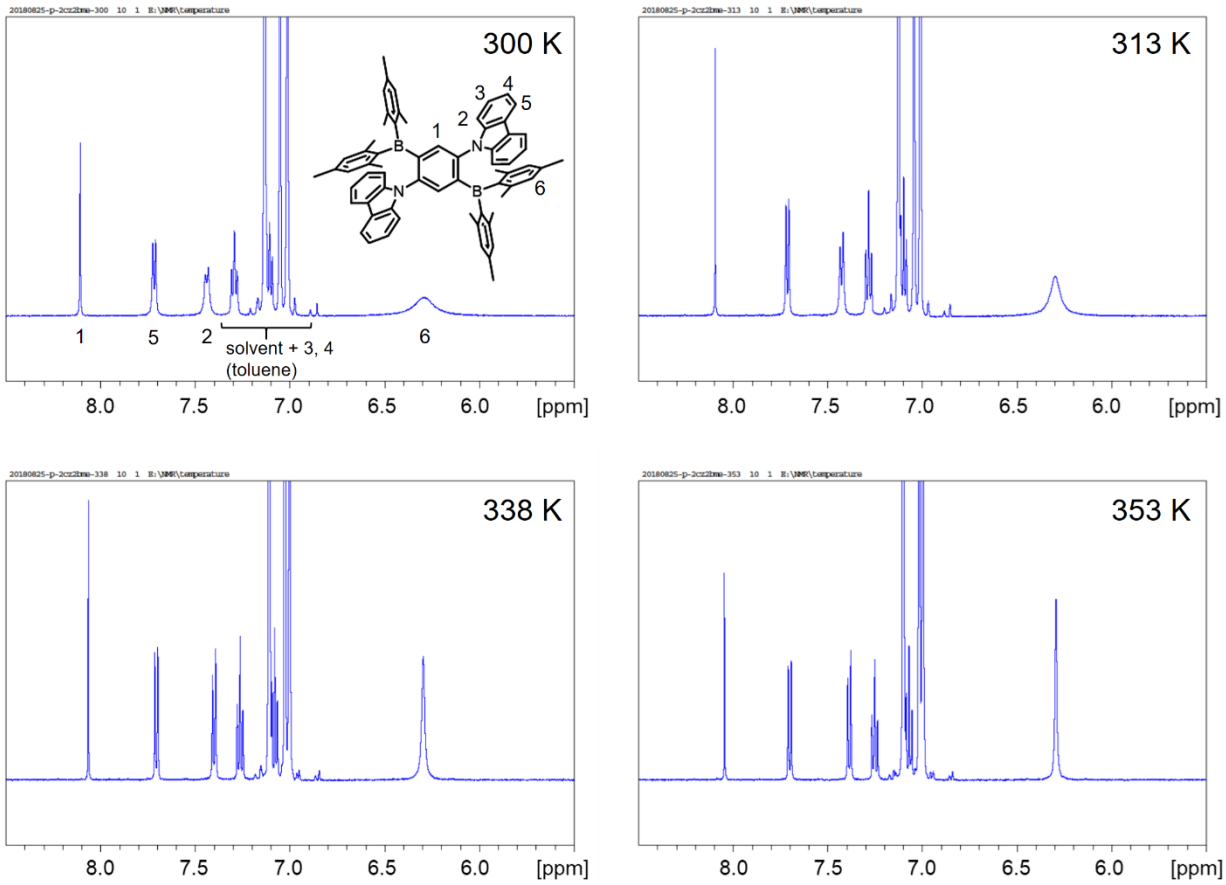

Figure 3-5 Temperature dependent ^{1}H-NMR spectrum of *p*-2Cz2BMe in toluene-d8.

3-2-4. Temperature dependence of PL lifetime

To investigate reverse ISC in more detail, I measured the temperature dependence of the k_{RISC}. The k_{RISC} of *p*-2Cz2BMe strongly decreases with decreasing temperature, as shown in **Fig. 3-6**. Using the equation (9) in chapter 1, I estimated the E_A^{RISC} for *p*-2Cz2BMe to be 0.13 eV, which is similar to the calculated $\Delta E_{S1\text{-}T1}$ (0.12 eV). These results indicate that reverse ISC proceeds directly between the S_1 and T_1 in *p*-2Cz2BMe. In this case, the factor for k_{RISC} depends on the $\Delta E_{S1\text{-}T1}$ and H_{SOC} value between the S_1 and T_1. The DFT calculations indicated that the S_1 and T_1 states in *p*-2Cz2BMe are dominated by HOMO → LUMO transition (S_1: 98%, T_1: 89%, *i.e.*, pure CT transitions). Therefore, the H_{SOC} value between the ^{1}CT and ^{3}CT states in *p*-2Cz2BMe is not expected to be large. Thus, the small $\Delta E_{S1\text{-}T1}$ induces relatively little mixing between the ^{1}CT and ^{3}CT states, leading to the small k_{RISC}.

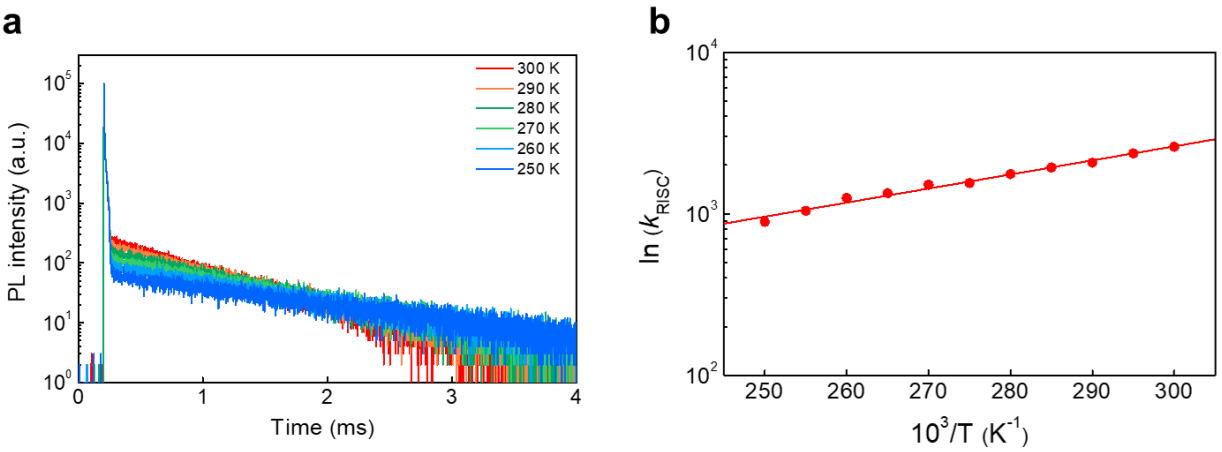

Figure 3-6 (**a**) PL decay curve of *p*-2Cz2BMe at 300-250 K. (**b**) Temperature dependence of the k_{RISC} of *p*-2Cz2BMe in toluene. The solid line is the fitting result based on the Arrhenius equation.

3-3. Conclusion

In summary, *p*-2Cz2BMe shows very slow reverse ISC (k_{RISC} : 2.1×10^3 s^{-1}) but high PLQY (89±2%), despite the relatively small $\Delta E_{S1\text{-}T1}$. These features are because the spin-flip process proceeds between the ^{1}CT and ^{3}CT states without mixing of the LE states. The rigid structure suppresses nonradiative decay from the T_1 to S_0. From these results, I conclude that management of the $|\Delta E_{3LE\text{-}3CT}|$ is important for controlling the spin-flip rate. I also conclude that the rigid structure

enables a long lifetime of triplet excitons without sacrificing the high PLQY. Slow reverse ISC is promising for materials in high sensitivity oxygen sensors. This molecular design approach opens a new path to obtaining oxygen sensing molecules for future bio-imaging applications.

3-4. Materials and Methods

3-4-1. Measurement of photoluminescence properties

PLQY was measured by an absolute PL quantum yield measurement system (C11347-01, Hamamatsu Photonics) with an excitation wavelength of 340 nm. Emission lifetimes were measured using a fluorescence lifetime measurement system (C11367-03 (Quantaurus-Tau), Hamamatsu Photonic) and CoolSpek Cs-0296 (UNISOKU Co.). UV–vis absorption spectra and PL spectra were recorded on UV–vis (Perkin-Elmer Lambda 950-PKA) and PL (FluoroMax-4, Horiba Jobin Yvon)) spectrophotometer.

3-4-2. Synthesis and characterization

1) 2,4-bis(carbazole-9-yl)-3,5-dibromobenzene *p*-2Cz2Br

First, carbazole (4.6 g, 27.5 mmol) was added to a dispersion of sodium hydride (60% in mineral oil 1.1 g, 27.5 mmol) in anhydrous DMF (100 ml) at 0 °C. After stirring for 30 min, 1,4-dibromo-2,5-difluorobenzene (3.0 g, 11 mmol) was added to the mixed solution under argon atmosphere. The reaction mixture was stirred at 60 °C overnight. The reaction mixture was quenched with water and the precipitate was filtered. Then the crude product was washed with water and methanol to produce *p*-2Cz2Br as white powder (4.83 g, 8.6 mmol, 75%).
^{1}H NMR: (500 MHz, $CDCl_3$): δ (ppm) = 8.19 (d, *J* = 7.6 Hz, 4H), 8.01 (s, 2H), 7.50 (t, *J* = 7.7 Hz, 4H), 7.37 (t, *J* = 7.9 Hz, 4H), 7.26 (d, *2*H).

2) *p*-2Cz2BMe (1)

To a solution of *p*-2Cz2Br (1.0 g, 1.77 mmol) in THF at -78 °C was added dropwise n-BuLi in hexane (1.6 M, 2.4 ml). The mixture was stirred for 30 min at -78 °C. Dimesitylboron fluoride (1.0 g, 3.89 mmol) was added to this solution and stirred at 0 °C overnight. After reaction, water was added to the solution and organic layer was extracted by dichloromethane. The reaction mixture was quenched with water and the precipitate was filtered and washed with water and methanol. The obtained solid was reprecipitated from chlorofolm/ethanol to produce *p*-2Cz2BMe as orange powder (0.82 g, 0.90 mmol, 51%).

^{1}HNMR ($CDCl_3$, 500 MHz) δ (ppm) = 7.79 (m, 6H), 7.26 (m, 4H), 7.13 (m, 8H), 6.27 (s, 8H), 1.98 (s, 12H), 1.47 (s, 24H)

^{13}C NMR: (125 MHz, $CDCl_3$): δ (ppm) = 149.42, 149.24, 140.40, 138.23, 137.94, 128.32, 128.05, 124.40, 121.89, 23.40, 21.11

MS/ASAP: m/z 904.92, (904.86 calcd for $C_{66}H_{62}B_2N_2$)

Elemental analysis: calcd. for $C_{66}H_{62}B_2N_2$: C, 87.61; H, 6.91; N, 3.10; found: C, 87.67; H, 6.94; N, 3.14.

References

1. Chen, X. K., Zhang, S. F., Fan. J. X., Ren, A. M., Nature of Highly Efficient Thermally Activated Delayed Fluorescence in Organic Light-Emitting Diode Emitters: Nonadiabatic Effect between Excited states. *J. Phys. Chem. C*, **119**, 9728-9733 (2015).

2. Gibson, J., Monkman, A. P., Penfold, T. J., The Importance of Vibronic Coupling for Efficient Reverse Intersystem Crossing in Thermally Activated Delayed Fluorescence Molecules. *ChemPhysChem*, **17**, 2956-2961 (2016).

3. Dias, F. B., Santos, J., Graves, D. R., Data, P., Nobuyasu, R. S., Fox, M. A., Batsanov, A. S., Palmeira, T., Berberan-Santos, M. N., Bryce, M. R., Monkman, A. P., The Role of Local Triplet Excited states and D-A Relative Orientation in Thermally Activated Delayed Fluorescence: Photophysics and Devices. *Adv. Sci*., **3**, 1600080 (2016).

4. Marian, C. M., Mechanism of the Triplet-to-Singlet Upconversion in the Assistant Dopant ACRXTN. *J. Phys. Chem. C*, **120**, 3715-3721 (2016).

5. Hosokai, T., Matsuzaki, H., Nakanotani, H., Tokumaru, K., Tsutsui, T., Furube, A., Nasu, K., Nomura, H., Yahiro, M., Adachi, C., Evidence and Mechanism of Efficient Thermally Activated Delayed Fluorescence Promoted by Delocalized Excited states. *Sci. Adv.*, **3**, e1603282 (2017).

6. Masui, K., Nakanotani, H., Adachi, C., Analysis of exciton annihilation in high-efficiency sky-blue organic light-emitting diodes with thermally activated delayed fluorescence. *Org. Electron.*, **14**, 2721–2726 (2013).

7. Furukawa, T., Nakanotani, H., Inoue, M., Adachi, C., Dual enhancement of electroluminescence efficiency and operational stability by rapid upconversion of triplet excitons in OLEDs. *Sci. Rep.*, **5**, 8429 (2015).

8. Noda, H., Nakanotani, H., Adachi, C., Excited state engineering for efficient reverse intersystem crossing. *Sci. Adv.*, **4**, eaao6910 (2018).

9. Hynes, J., Floyd, S., Soini, A., O'Connor, R., Papkovsky, D. B., Fluorescence-Based Cell Viability Screening Assays Using Water-Soluble Oxygen Probes. *J. Biomol. Screen.*, **8**, 264-272 (2003).

10. Hasebe, N., Suzuki, K., Horiuchi, H., Suzuki, H., Yoshihara, T., Okutsu, T., Tobita, S., Intracellular and in Vivo Oxygen Sensing Using Phosphorescent Ir(III) Complexes with a Modified Acetylacetonato Ligand. *Anal. Chem.*, **87**, 2360-2366 (2015).

11. Uoyama, H., Goushi, K., Shizu, K., Nomura, H., Adachi, C., Highly efficient organic light-emitting diodes from delayed fluorescence. *Nature*, **492**, 234-238 (2012).

12. Yang, Z., Mao, Z., Xie, Z., Zhang, Y., Liu, S., Zhao, J., Xu, J., Chi, Z., Aldred, M. P., Recent advances in organic thermally activated delayed fluorescence materials. *Chem. Soc. Rev.*, **46**, 915-1016 (2017).

13. Berberan-Santos, M. N., Garcia, J. M. M., Unusually strong delayed fluorescence of C_{70}. *J. Am. Chem. Soc.*, **118**, 9391–9394 (1996).

14. Xiong, X., Song, F., Wang, J., Zhang, Y., Xue, Y., Sun, L., Jiang, N., Gao, P., Tian, L., Peng, X., Thermally Activated Delayed Fluorescence of Fluorescein Derivative for Time-Resolved and Confocal Fluorescence Imaging. *J. Am. Chem. Soc.*, **136**, 9590-9597 (2014).

15. Li, T., Yang, D., Zhai, L., Wang, S., Zhao, B., Fu, N., Wang, L., Tao, Y., Huang, W., Thermally Activated Delayed Fluorescence Organic Dots (TADF Odots) for Time‐Resolved and Confocal Fluorescence Imaging in Living Cells and In Vivo. *Adv. Sci.*, **4**, 1600166 (2017).

16. Lim, B. T., Okajima, S., Chandra, A. K., Lim, E. C., Radiationless transitions in electron donor-acceptor complexes: selection rules for $S_1 \rightarrow T$ intersystem crossing and efficiency of $S_1 \rightarrow S_0$ internal conversion. *Chem. Phys. Lett.*, **79**, 22-27 (1981).

17. Yamamoto, M., Tsuji, Y., Tuchida, A., Near-infrared charge resonance band of intramolecular carbazole dimer radical cations studied by nanosecond laser photolysis. *Chem. Phys. Lett.*, **154**, 559-562 (1989).

18. Kaafarani, B. R., Risko, C., El-Assaad, T. H., El-Ballouli, A. O., Marder, S. R., Barlow, S., Mixed-Valence Cations of Di(carbazol-9-yl) Biphenyl, Tetrahydropyrene, and Pyrene Derivatives. *J. Phys. Chem. C*, **120**, 3156-3166 (2016).

Chapter 4

Critical role of intermediate electronic states for spin-flip processes in multi-donor-acceptor charge-transfer-type purely organic molecules

Hiroki Noda, Xian-Kai Chen, Hajime Nakanotani, Takuya Hosokai, Momoka Miyajima, Naoto Notsuka, Jean-Luc Brédas, & Chihaya Adachi
(submitted).

Abstract

Spin-flip in purely organic molecular systems is often described as a forbidden process; however, it is commonly observed and utilized to harvest triplet excitons in a wide variety of organic material-based applications, such as OLEDs and photon upconversion systems. Although the initial and final electronic states of the spin-flip between the S_1 and T_1 state are self-evident, the exact process and the role of intermediate states through which spin-flip occurs are still far from being comprehensively determined. In chapter 4, I show that efficient spin-flip in multi-D-A CT-type organic molecular systems involves the critical role of an intermediate triplet excited-state. The proposed mechanism can be applied to unify the understanding of the ISC mechanism in a wide variety of CT-type molecular systems, opening the way to greater control over the spin-flip rates.

4-1. Introduction

The dynamics of processes that allow the conversion between a S and a T or the S_0 in purely organic molecular systems is central to determining the fate of excitons and critical in applications including chemical reactions (*1*), EL (*2-4*), LL-RTP (*5*), bio-imaging (*6,7*), chemical compasses (*8*), photon upconversion systems (*9*), photodynamic therapy (*10*) and singlet fission (*11*). Purely organic aromatic molecules exhibiting TADF are particularly attractive systems for studying the spin-flip mechanisms since both forward and reverse ISC are simultaneously operational in these molecules. Based on the equation (2) in chapter 1, minimization of $\Delta E_{S1\text{-}T1}$ has been a widely adopted method for realizing efficient TADF. This is most commonly achieved by the design of CT-type molecules with spatially separated hole and electron distributions in the excited-state. Efficient TADF with a high reverse ISC efficiency approaching 100% has been observed in a variety of recently developed CT-type molecular systems (*12*). However, in such molecules, both the S_1 and T_1 states generally have substantial CT-excitation character; the consequence in that the direct spin-flip between the ^{1}CT and ^{3}CT should in reality be very inefficient because of the vanishing SOC between such states (*13*). Thus, the question naturally arises of how spin-flip does in fact proceed in these molecules.

To rationalize the spin-flip mechanism in these CT-type molecules, several groups have recently proposed that reverse ISC is promoted by the nonadiabatic coupling between a ^{3}CT state and a ^{3}LE state since a large difference in the nature of the excitation characters for CT and LE states should induce a large H_{SOC} value (*14-20*). In addition, I also figured out the importance of the energy level alignment between a ^{3}CT state and a ^{3}LE state to control a spin-flip rate in CT-type organic molecules in chapters 2 and 3. However, there exist a wide variety of CT-type molecular systems to which this mechanism does not apply. In particular, this mechanism fails to explain the spin-flip processes in multi-D-A type CzCN derivatives (**Fig. 4-1a**) as represented instance by 2,4,5,6-tetra(9H-carbazol-9-yl)isophthalonitrile (4CzIPN) (*4*), because the energies of the ^{3}LE states of the PhCz (3.08 eV) and the isophthalonitrile (IPN) (3.27 eV) (*21* are dramatically higher than those of both the S_1 (2.71 eV) and T_1 (2.67 eV) states of 4CzIPN. Thus, the nonadiabatic coupling between

$^3CT_1$ and ^3LE is expected to be hardly efficient in emitters such as 4CzIPN.

Although there are many reports on the process of spin conversion in multi-donor-acceptor-type CzCN molecules such as 4CzIPN as a representative example, a comprehensive understanding is still missing (*18*, *22-24*). Since CzCN derivatives are promising materials not only for highly efficient and stable OLEDs (*4, 25, 26*) but also for photon upconversion media (*27*) because of their nearly 100% PLQY and high k_{RISC}, these derivatives represent key model systems for CT-type molecules exhibiting *E*-type DF; a comprehensive understanding of the spin-flip mechanisms in these systems is thus most desirable. Here, I uncover the spin-flip routes for both forward and reverse ISC processes in a wide variety of CT-type molecules via a joint experimental and theoretical study. I demonstrate that the spin-flip processes proceed through a specific intermediate higher-lying triplet excited-state and, importantly, that this intermediate excited-state is related to the electronic structure of a "partial" molecular structure of the CT-type molecule. The observation of forward ISC with a well-defined activation energy indicates the instances where the energy of the intermediate triplet excited-state lies higher than that of the S_1 state, and the involvement of the intermediate excited-state is explained based on molecular vibrations.

4-2. Results and discussion

4-2-1. Photophysical properties of CzCN derivatives

First, I summarize the fundamental photophysical properties of the CzCN derivatives of 4CzIPN and 5CzBN (*25*) in toluene as model cases here (**Table 4-1** and **Fig. 4-1**). An important observation is, while k_{RISC} of 4CzIPN (8.8×10^5 s^{-1}) is four times larger than that of 5CzBN (2.2×10^5 s^{-1}), k_{ISC} of 4CzIPN (0.7×10^8 s^{-1}) is in fact three times smaller than that of 5CzBN (2.5×10^8 s^{-1}). Although the k_r is nearly the same in both molecules, the prompt component of PLQY for 5CzBN (7%) is much lower than that for 4CzIPN (21%). This implies that a large fraction of initially

generated singlet excitons in 5CzBN very rapidly transform to triplet excitons through ISC, leaving a fewer number of singlets to produce PF.

Table 4-1 Photophysical properties of TADF emitters in toluene.

Compound	PLQY (%)[*1]	τ_p (ns)	τ_d (μs)	k_r (10^7 s^{-1})	k_{ISC} (10^8 s^{-1})	k_{RISC} (10^5 s^{-1})	E_A^{ISC} (eV)	E_A^{RISC} (eV)	S_1 (eV)	T_1 (eV)	$\Delta E_{S1\text{-}T1}$ (eV)	$\Delta E_{S1\text{-}T2}$ (eV)	$\Delta E_{T1\text{-}T2}$ (eV)
4CzIPN	21 / 86	11.3	4.6	1.8	0.70	8.8	0.04	0.09	2.71	2.67	0.04	0.04	0.08
5CzBN	7 / 75	3.8	46.8	1.9	2.5	2.2	N.A.	0.13	2.95	2.78	0.17	–0.15	0.02
m-3CzIPN	12 / 86	7.9	26.1	1.5	1.1	2.7	0.04	0.11	2.91	2.76	0.15	–0.05	0.10
o-3CzIPN	17 / 86	13.8	7.5	1.2	0.60	6.6	0.04	0.10	2.81	2.74	0.07	0.05	0.12
p-2DPA2BMe	60 / 80	10	N.O.	2.3	0.08	---	---	---	2.20	2.02[*2]	0.18[*2]	0.39	0.59

*1: Photoluminescence quantum efficiency of the solution sample before / after Ar bubbling.

*2: These values were obtained from the result of theoretical calculations (ω B97XD /6-31G(d,p) calculation).

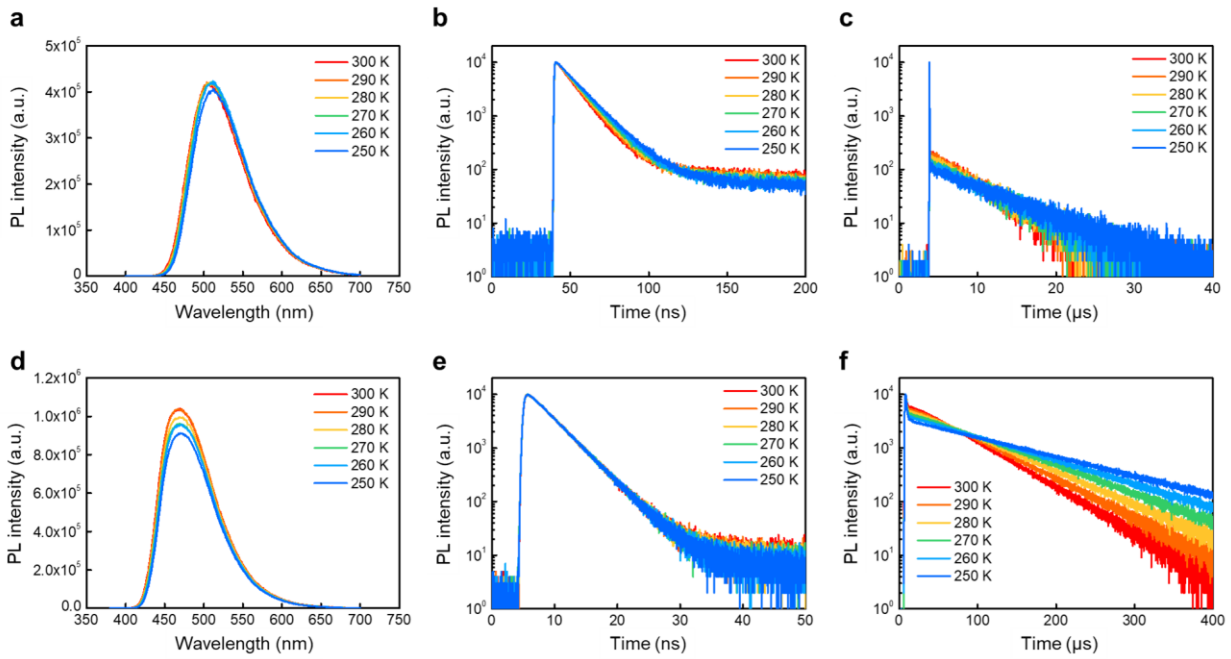

Figure 4-1 PL spectrum, nano-seconds and micro-seconds PL decay profile of 4CzIPN (**a, b, c**) and 5CzBN (**d, e, f**) in toluene solutions at different temperature.

To understand the spin-flip processes in more detail, I investigated the temperature dependences of k_{ISC} and k_{RISC}. As expected for TADF, the k_{RISC} values of 4CzIPN and 5CzBN strongly decrease with temperature (**Fig. 4-2b**). Using equation (9) in chapter 1, I estimated the E_A^{RISC}

for 4CzIPN and 5CzBN to be 0.09 eV and 0.13 eV, respectively. In contrast to k_{RISC}, k_{ISC} of 5CzBN does not exhibit any temperature dependence (**Fig. 4-2c**). Interestingly, k_{ISC} of 4CzIPN clearly increases with temperature, yielding an activation energy for forward ISC (E_A^{ISC}) of 0.04 eV (**Fig. 4-2c**). Although toluene shows a slight polarity change with decreasing temperature (*28*), I confirmed that this temperature dependent polarity did not impact to any significant extent the excited-state energies of 4CzIPN and 5CzBN over this temperature range (**Fig. 4-1**), which indicates that the forward ISC in 4CzIPN is an uphill process. Importantly, I found that the sum of the energy gap between S_1 and T_1 (S_1 = 2.71 eV and T_1 = 2.67 eV, determined from the fluorescence and phosphorescence spectra, respectively; $\Delta E_{S1\text{-}T1}$ = 0.04 eV) and of E_A^{ISC} (0.04 eV) is nearly equal to E_A^{RISC} (0.09 eV) in 4CzIPN. Thus the combination of these experimental results points to the existence of an intermediate excited-state between S_1 and T_1 that mediates both the forward and reverse ISC processes in 4CzIPN. As demonstrated in the investigation by Samanta et al., (*29*) I expect that the excitation character of the intermediate excited-state differs largely from those of S_1 and T_1, since a change in the nature of the excited-state character during ISC is required to induce a large H_{SOC} and thus facilitate ISC.

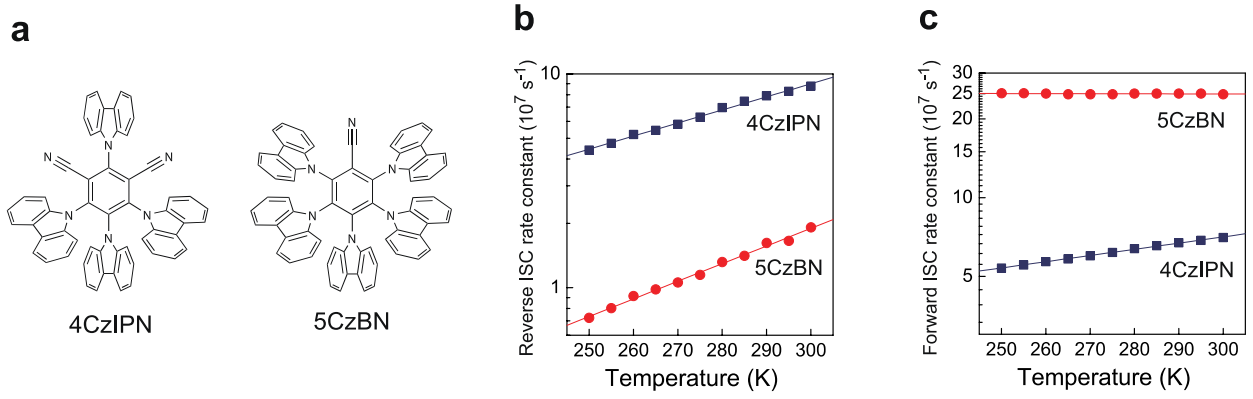

Figure 4-2 (**a**) Molecular structures of 4CzIPN and 5CzBN. (**b**) Temperature dependence of the k_{RISC} of 4CzIPN and 5CzBN in toluene. (**c**) Temperature dependence of the k_{ISC} of 4CzIPN and 5CzBN in toluene. The solid lines in each figure are fitting results based on the Arrhenius equation. The concentration of the toluene solution was fixed at 10^{-5} mol L^{-1}.

In this chapter, I reveal that the nature of the intermediate excited-state for the spin-flip processes in these CT-type molecules is a higher-lying CT triplet excited-state that corresponds to the electronic structure of a partial molecular (sub-molecular) structure of the parent molecule. First, I test the validity of my proposed mechanism by applying it to explain the spin-flip processes of 4CzIPN. Then, I demonstrate the robustness of the mechanism by extending it to other CT-type molecular systems.

4-2-2. The role of sub-molecular structures

The appreciation of the role of partial molecular structures was triggered by observation

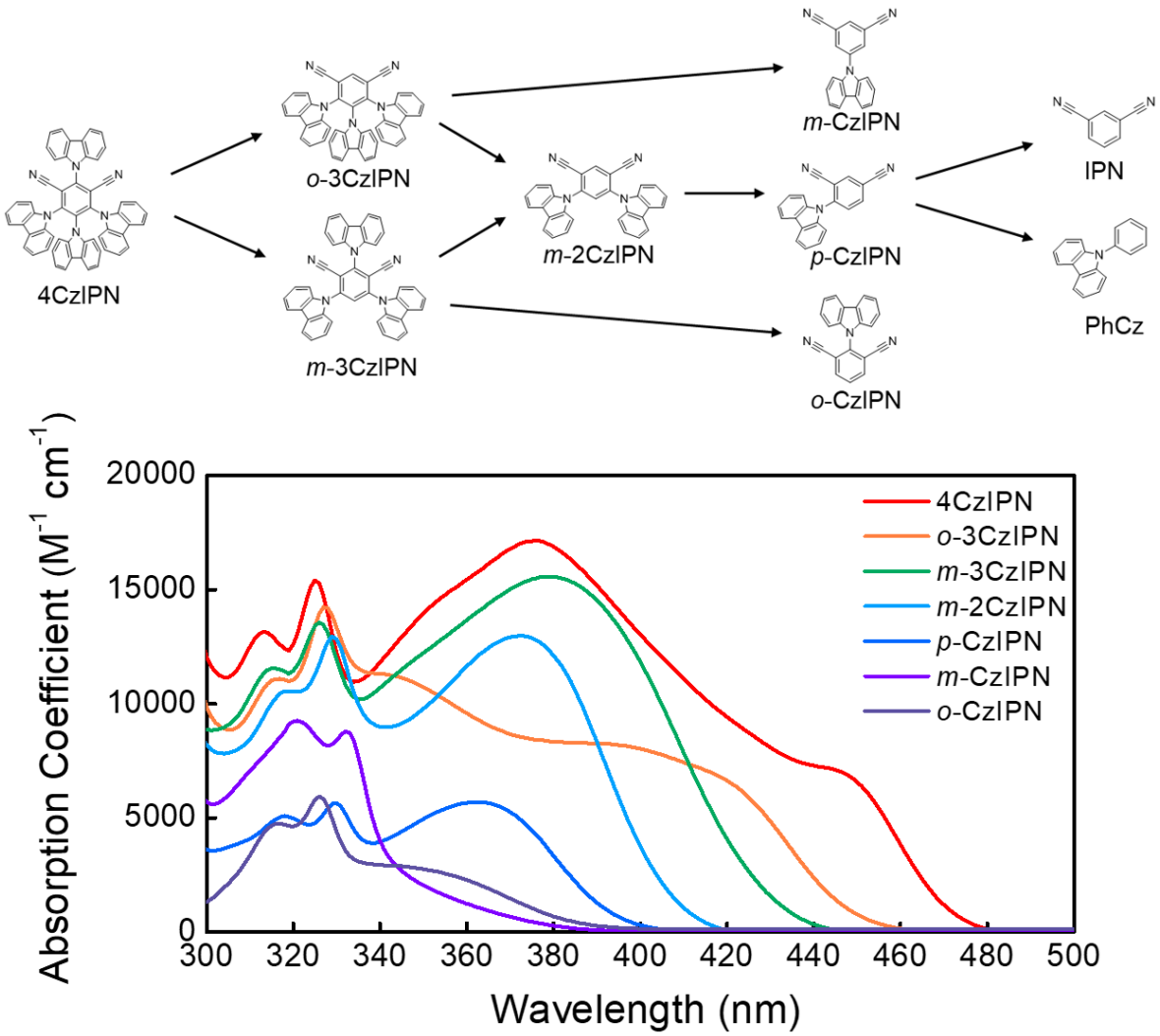

Figure 4-3 Complete and partial molecular structures of 4CzIPN and absorption coefficient spectra of 4CzIPN and the partial molecular structures of 4CzIPN in toluene at a concentration of 10^{-5} mol L^{-1}.

made when analyzing the absorption spectra of 4CzIPN and its sub-molecular structures *o*-3CzIPN and *m*-3CzIPN (**Fig. 4-3**), which differ from 4CzIPN by the removal of a single Cz unit. As shown in **Fig. 4-3**, the absorption spectrum of 4CzIPN has features reflecting those of *o*-3CzIPN and *m*-3CzIPN, which points to the existence of electronic states in 4CzIPN similar to those of *o*-3CzIPN and *m*-3CzIPN. Note that the absorption spectra of *o*-3CzIPN (or *m*-3CzIPN) also well reflect features of the spectra (**Fig. 4-3**) of its partial derivatives, *i.e.*, *m*-2CzIPN and CzIPN derivatives. Given these characterization of the singlet excited-states, I conjectured that a same situation could appear in the triplet manifold. To ascertain the possibility that the T_2 state of 4CzIPN originates from *o*-3CzIPN and/or *m*-3CzIPN, I assessed the excited-state energies in the letter. The T_1 energies of *o*-3CzIPN (2.74 eV) and *m*-3CzIPN (2.76 eV) are higher than the $^1CT_1$-state energy (2.71 eV) of 4CzIPN, as shown in **Fig. 4-4**, by 0.03 and 0.05 eV, respectively, which is in excellent agreement with the observed E_A^{ISC} (0.04 eV). Moreover, note that E_A^{RISC} (0.09 eV) corresponds well to the energy gap

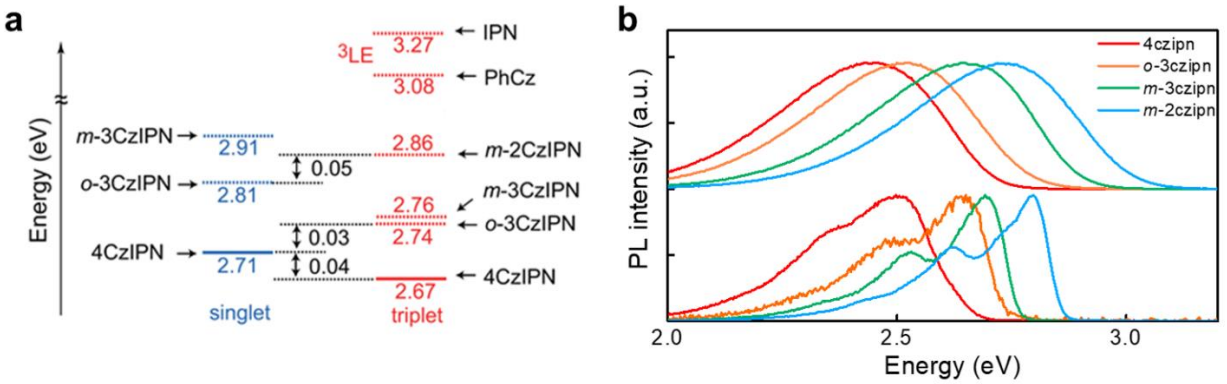

Figure 4-4 (**a**) Energy diagrams showing the singlet and triplet excited-states of 4CzIPN and of the partial molecular structures of 4CzIPN. All energies were estimated experimentally from the onset energies of the fluorescence and phosphorescence spectra of the molecules in toluene (10^{-5} mol L^{-1}). (**b**) Fluorescence spectra (top) and phosphorescence spectra (bottom) of 4CzIPN, *o*-3CzIPN, *m*-3CzIPN, and *m*-2CzIPN in 10^{-5} mol L^{-1} toluene solutions. Phosphorescence spectra were measured in 10^{-5} mol L^{-1} toluene solutions at 77 K.

between the T_1 state of 4CzIPN and the T_1 state of *o*-3CzIPN or *m*-3CzIPN. These results suggest that the forward (or reverse) ISC process between S_1 and T_1 in 4CzIPN proceeds through a higher-lying T_2 with character similar to *o*-3CzIPN and/or *m*-3CzIPN.

To further answer experimentally the question of whether it is the partial structure corresponding to *o*-3CzIPN or *m*-3CzIPN which reflects the electronic structure of the T_2 states in 4CzIPN, TAS was performed; the results are shown in **Fig. 4-5**. The TAS contour map of 4CzIPN is found to match the contour map of *o*-3CzIPN better than that of *m*-3CzIPN, which indicates that the relevant higher-lying triplet-state in 4CzIPN has an electronic structure similar to that in *o*-3CzIPN.

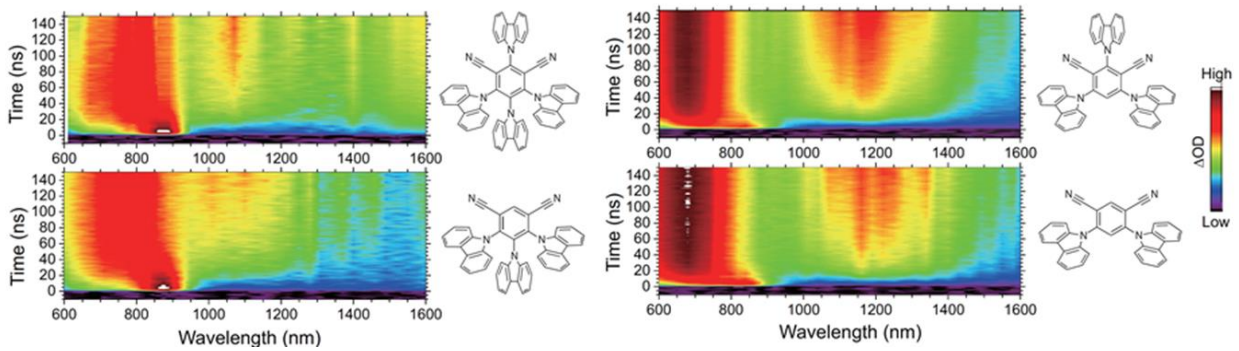

Figure 4-5 Contour maps of transient absorption spectra of 4CzIPN, *o*-3CzIPN, *m*-3CzIPN, and *m*-2CzIPN in toluene at a concentration of 10^{-3} mol L^{-1}. The TAS measurements were performed at 295 K.

To evaluate the temperature effect on TAS spectrum, TAS measurement of 4CzIPN at low temperature (183 K) was performed (**Fig. 4-6**). Although there is almost no change of the absorption intensity of the CR state observed around 1500 nm region between at room temperature and 183 K, it was found that the absorption intensity around 600-800 nm and 1000-1400 nm corresponding to the absorption band of the partial molecular structure was clearly decreased with decreasing a temperature, indicating that the population of excited state density on the high order triplet state, *i.e.*, intermediate triplet state, is small at low temperature. This results also suggest that the spin-flip of 4CzIPN proceeds through a higher-lying triplet states corresponding with partial molecular structures.

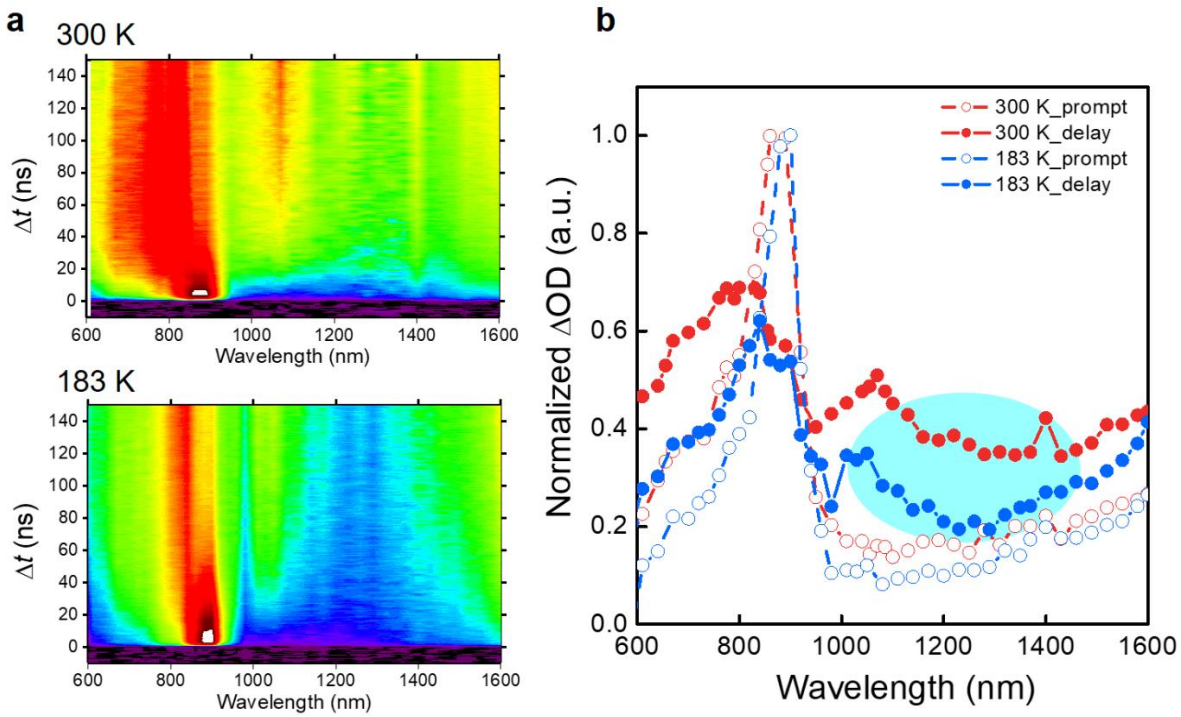

Figure 4-6 (**a**) Contour maps of transient absorption spectra of 4CzIPN in toluene at a concentration of 10^{-3} mol L^{-1} at 300 K and 183 K. (**b**) The TAS spectra of the prompt (Δt = 4.5 to 5.5 ns) and delay (Δt = 50 to 100 ns) states of 4CzIPN at 300 K and 183 K.

Next, to clarify the nature of the excited-states in 4CzIPN, I performed detailed quantum-chemical calculations using the long-range corrected ωB97XD functional with a non-empirically tuned range-separation parameter ω, which is appropriate for extended π-conjugated system (*30*). The S_1-state equilibrium geometry of 4CzIPN exhibits a dihedral angle of about 35° between the 2-Cz and 5-Cz groups (**Fig. 4-7a**), and the hole and electron densities are strongly localized on the 4,5,6-position Cz units and the IPN unit, respectively, which indicates the formation of a conventional CT state in the S_1 state, *i.e.*, $^1CT_1$. In the T_1- and T_2-state equilibrium geometries the dihedral angle between the para-linked 2-Cz and 5-Cz decreases and these two groups essentially become coplanar. The T_2 state is assigned as a hybrid local-CT excited-state ($^3HLCT_2$) since the hole density (mainly on the 4,5,6-position Cz units) and the electron density partially overlap on the central phenyl ring (**Fig. 4-7a**). Interestingly, in the T_1 state the hole density clearly spreads to the 2-Cz unit, which I attribute to the appearance of a CR-type HLCT state in the T_1 state, *i.e.*, $^{CR,3}HLCT_1$. This theoretical picture agrees well with the earlier experimental observations, via TAS measured by Hosokai et al.

(*18*), of CR-type ^{3}CT states that are formed between the mixed-valence radical cation formed in a pair of the linearly connected Cz units and an IPN unit (*31,32*) in 4CzIPN. However, at the optimized S_1 and T_2 geometries of 4CzIPN, there is little to no contribution from 2-Cz to the hole density distribution in those states, leading to similar electronic structures at the equilibrium S_1 and T_2 geometries. The larger difference in the excited-state characters between S_1 and T_1 than T_2 makes the spin-flip between S_1 and T_1 seem, at first sight, more probable; however, as documented above, forward ISC in 4CzIPN is experimentally observed to be an uphill process; thus, the spin-flip should be proceeding between S_1 and T_2. Thus, this raises the question of what is the additional factor that actually makes spin-flip between S_1 and T_2 more favorable.

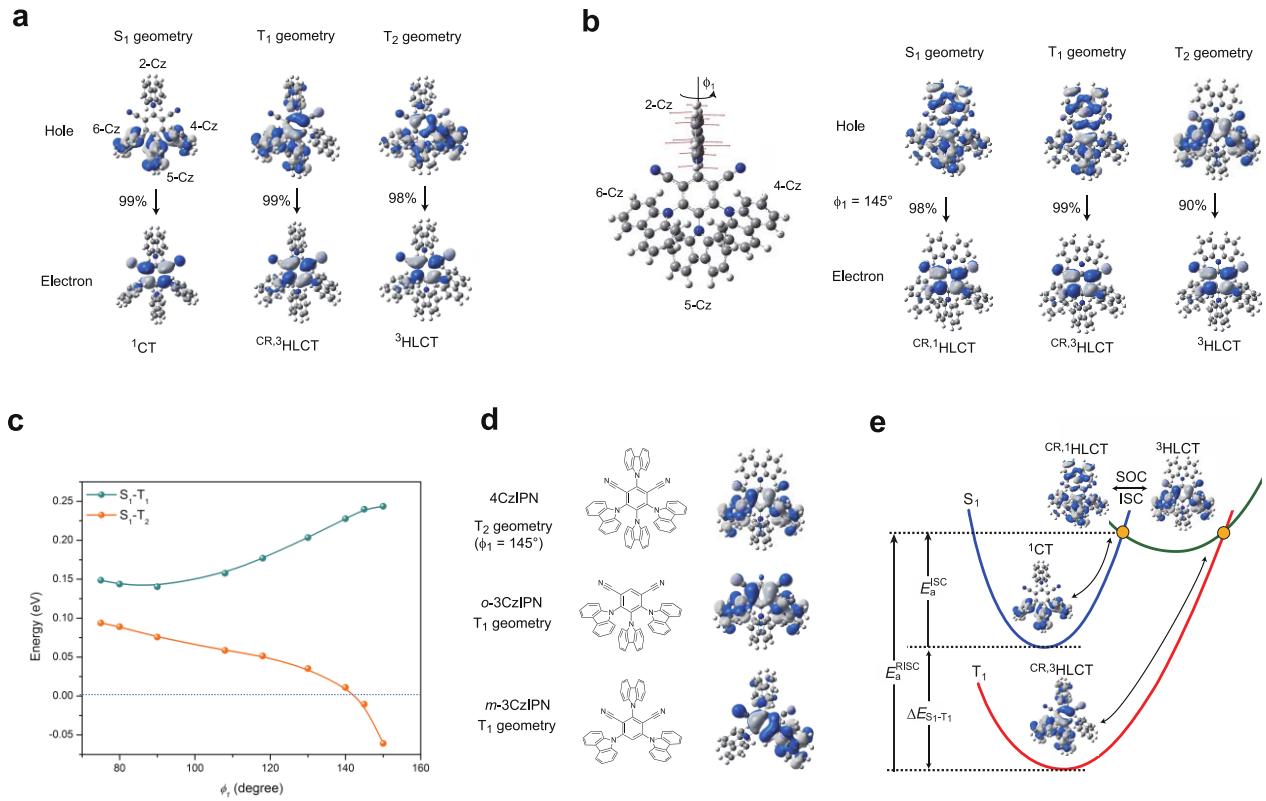

Figure 4-7 (**a**) Hole and electron Natural Transition Orbitals (NTOs) in 4CzIPN at optimized S_1, T_1, and T_2 geometries. (**b**) Left: Rotation mode vector of the 2-Cz group relative to the center phenyl ring. Right: Hole and electron NTOs in the S_1, T_1, and T_2 states of 4CzIPN at $\phi_1 = 145°$. (**c**) Dependence on ϕ_1 of the energy gaps between S_1 and T_1 and S_1 and T_2 calculated using TDDFT/ωB97XD with a non-empirically tuned range-separation parameter ω. (**d**) Hole NTOs of the T_2 state in 4CzIPN at $\phi_1 = 145°$, T_1 state in *o*-3CzIPN, and T_1 state in *m*-3CzIPN. (e) Proposed spin-flip process with illustration of the energy potential surfaces for the S_1, T_1, and T_2 states of 4CzIPN.

To answer this question, I turned our attention to the molecular vibration of 4CzIPN. According to the DFT calculations, only the 2-Cz unit can easily rotate and change its dihedral angle with the center phenyl ring, as shown in **Fig. 4-7b**; indeed, the bulkiness of the 4CzIPN molecular structure prevents a large change in dihedral angles for any of the Cz units in the 4,5,6-positions. Due to the low energy (12 cm^{-1}) of the vibrational mode related to the 2-Cz rotation, the mode is effectively activated at room temperature. When the dihedral angle (ϕ_1) with the central phenyl ring increases to 145º via 2-Cz rotation, the excited-state character of the S_1 state transforms from conventional $^1CT_1$ (**Fig. 4-7a**) to CR-type HLCT (**Fig. 4-7b**) due to an increase in the planarity between the 2-Cz and 5-Cz units. Since this thermally activated transformation operates at room temperature, the S_1 state gains a mixed excited-state character. On the other hand, the excited-state character of the T_2 state is not sensitive to the rotation of the 2-Cz unit and remains ^{3}HLCT (**Fig. 4-7a** and **4-7b**). Thus, this rotation induces a large difference between the excitation characters of the S_1 and T_2 states while the S_1 state gains an excitation character similar to that of the T_1 state. In fact, the calculated SOC matrix element (SOCME) between S_1 and T_2 (0.51 cm^{-1}) is nearly one order of magnitude larger than that between S_1 and T_1 (0.06 cm^{-1}). According to Fermi's Golden rule (*33,34*), k_{ISC} is proportional to the square of the SOCME and described as

$$k_{ISC} = \frac{2\pi}{\hbar}\rho_{FC}\,|\langle S_1|H_{SOC}|T_1\rangle|^2 \qquad (12)$$

where $|\langle S_1|H_{SOC}|T_1\rangle|$ is the SOCME and ρ_{FC} is the Frank–Condon weighted density of states. ρ_{FC} can be given by the following semiclassical Marcus theory expression.

$$\rho_{FC} = \frac{1}{\sqrt{4\pi\lambda k_B T}}\, exp\left[-\frac{(\Delta E_{S-T}+\lambda)}{4\lambda k_B T}\right] \qquad (13)$$

where λ is the Marcus reorganization energy associated with the forward ISC process, k_B is the Boltzmann constant, and T is temperature. By utilizing these formulas, I calculated the k_{ISC} ($S_1 \rightarrow T_1$) and k_{ISC} ($S_1 \rightarrow T_2$). In forward ISC process from S_1 to T_1, I assumed a process without an activation barrier (**Fig. 4-8a**). In this case, λ is equal to $\Delta E_{S1\text{-}T1}$ (0.04 eV) and k_{ISC} ($S_1 \rightarrow T_1$) is estimated to be 9.9×10^5 s^{-1}. On the other hand, in the forward ISC process from S_1 to T_2, the relationship of E_A^{ISC}, $\Delta E_{S\text{-}T}$ and λ is given by the following formula.

$$E_A = \frac{(\Delta E_{S-T} + \lambda)^2}{4\lambda} \quad (14)$$

Since E_A^{ISC} and $\Delta E_{S1\text{-}T2}$, the energy gap between S_1 in 4CzIPN (2.71 eV) and T_1 in *o*-3CzIPN (2.74 eV) (**Fig. 4-8b**), are 0.04 eV and 0.03 eV, respectively, λ and k_{ISC} ($S_1 \rightarrow T_2$) is calculated to be 0.09 eV and 4.8×10^7 s^{-1}. k_{ISC} ($S_1 \rightarrow T_2$) (4.8×10^7 s^{-1}) shows good agreement with experimentally obtained k_{ISC} (7.0×10^7 s^{-1}) rather than k_{ISC} ($S_1 \rightarrow T_1$) (9.9×10^5 s^{-1}). Furthermore, the S_1 energy in 4CzIPN is calculated to become equal to the T_2 energy at $\phi_1 = 145°$ (**Fig. 4-7c**). Note that gaining a fully quantitative agreement with experiment remains a most difficult task since it would require a precise knowledge of all the possible molecular configurations that exist in the solution state (or solid state). I believe that the key point here is that molecular vibrations do contribute to significant reductions in the energy gaps between relevant excited states. Also, I note that vibrational quantum-tunneling effects (which depend on the overlap between the quantum vibrational wavefunctions in different states and do not require to fully overcome an energy barrier) do impact electronic transition processes (*35*). The important consequence is that fully reaching a dihedral angle of 145° is not a necessary condition to trigger an increased RISC process from T_2 to S_1.

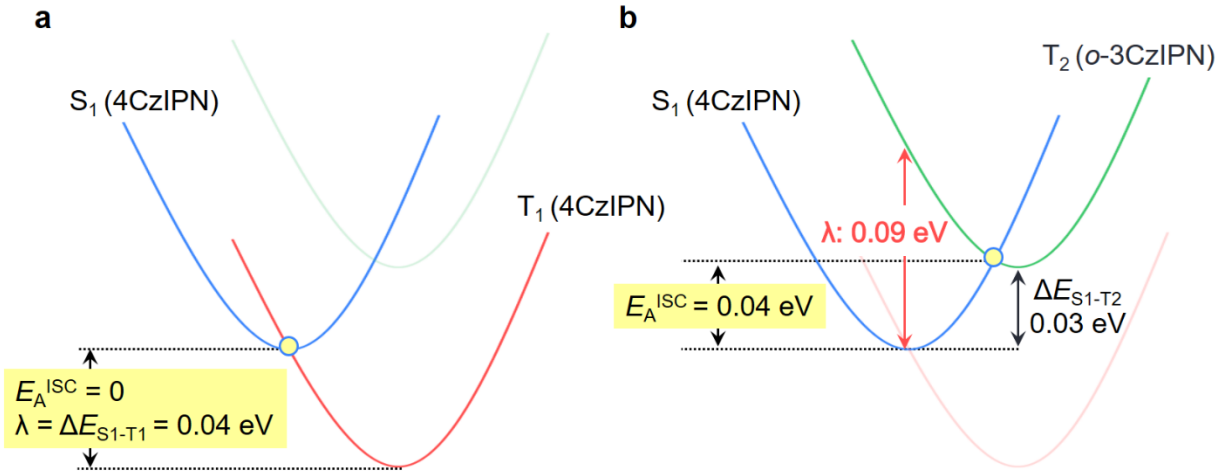

Figure 4-8 (**a**) Schematic image of forward ISC process between S_1 and T_1 in 4CzIPN. Non-activation energy is assumed. (**b**) Schematic image of forward ISC process between S_1 and T_2 (originated from T_1 in *o*-3CzIPN) in 4CzIPN. This process is proposed process.

Therefore, this large SOCME and decreasing energy gap at the cross point of the S_1 and T_2 potential energy surfaces will further facilitate the spin-flip processes. Importantly, the calculations indicate that the excitation character of the T_2 (^{3}HLCT$_2$) state at $\phi_1 = 145°$ in 4CzIPN is very similar to the T_1 state character of *o*-3CzIPN (**Fig. 4-7d**). Thus, these theoretical results confirm the experimental observations of the role of the partial molecular structures and lead to the conclusion that the higher triplet-state with an electronic structure similar to the T_1 state of *o*-3CzIPN is the critical intermediate state in the spin-flip processes in 4CzIPN.

Combing these experimental and theoretical results, I summarize the relationship between the molecular vibration (ring rotation) and the spin-flip processes in 4CzIPN as illustrated in **Fig. 4-7e**. The activated rotation of the 2-Cz unit results in the evolution of the S_1 state excitation character from ^{1}CT$_1$ to ^{CR,1}HLCT$_1$. Near the crossing point between the two potential energy surfaces, this then triggers the spin-flip between the ^{CR,1}HLCT$_1$ state and the ^{3}HLCT$_2$ state, with the latter corresponding to the T_1 state of the sub-molecular structure equivalent to *o*-3CzIPN. The ^{3}HLCT$_2$ state then vibrationally relaxes to ^{CR,3}HLCT$_1$ via internal conversion. Then, in the opposite order, this process can also be used to explain the reverse ISC process. My conclusion can further explain the origin of the difference in the pre-exponential constant (A) in the Arrhenius equation between forward ISC ($A = 3.0 \times 10^8$) and reverse ISC ($A = 2.7 \times 10^7$) process. The larger A indicates the higher transition frequency to crossing point between S_1 and T_2 states. In case of the forward ISC process, only one crossing point ($S_1 \rightarrow T_2$) exists. However, the reverse ISC process has two crossing points for a spin-flip ($T_2 \rightarrow S_1$) and an internal conversion process ($T_2 \rightarrow T_1$). Since an internal conversion process is faster than a spin-flip process, the transition frequency in the reverse ISC process becomes small. Therefore, I concluded that the A in the reverse ISC process is smaller than the forward ISC process.

4-2-3. Spin-flip processes in various CT-type molecules

At this state, I experimentally and theoretically confirmed that, in the case of the 4CzIPN system, a higher-lying triplet state corresponding to the T_1 state of a partial molecular structure plays a key role as the intermediate state in ISC. Next, to demonstrate the robustness of this understanding

of spin-flip in CT-type molecules, I evaluate the spin-flip processes in three different types of CT molecules: (i) a CT-type molecule in which the forward ISC process exhibits a temperature dependence, *o*-3CzIPN; (ii) a CT-type molecule in which k_{ISC} is very fast with no temperature dependence, 5CzBN; and (iii) a CT-type molecule in which the forward ISC process is limited, *p*-2DPA2BMe.

In *o*-3CzIPN, the S_1 state lies below the T_1 state of the partial molecular structure *m*-2CzIPN, which gives rise to the *o*-3CzIPN T_2, as summarized in **Fig. 4-4a**. In this instance, the proposed mechanism would predict that both forward and reverse ISC are uphill processes. The experimental results confirm that indeed the two ISC processes exhibit positive activation energies (E_A^{ISC} = 0.04 eV and E_A^{RISC} = 0.10 eV; **Fig. 4-9**). Moreover, these activation energies agree well with the energy gaps between the T_1 energy of *m*-2CzIPN and the S_1 (E_A^{ISC}) or T_1 (E_A^{RISC}) energy of *o*-3CzIPN (see **Fig. 4-4a**).

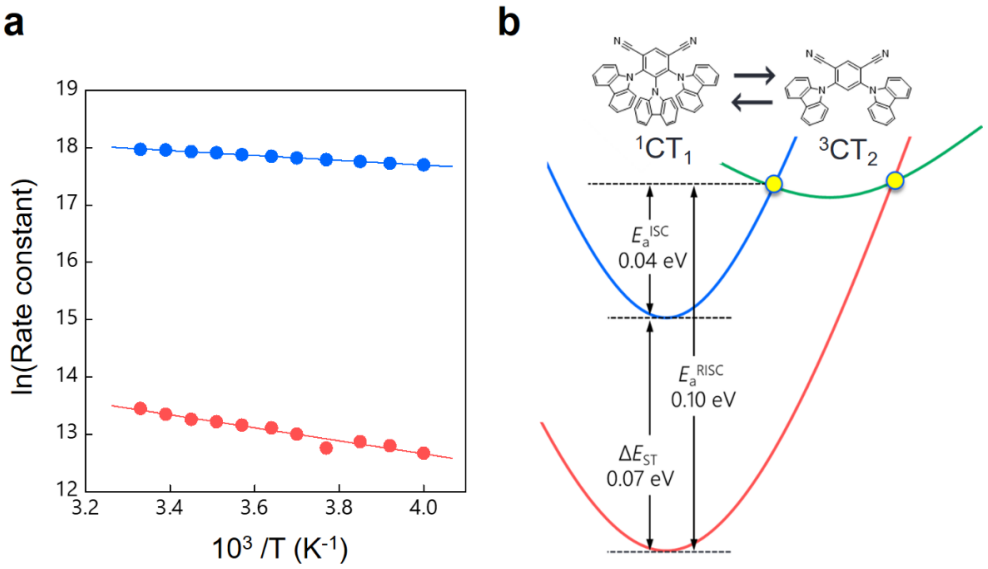

Figure 4-9 (**a**) Arrhenius plot of forward ISC (blue circle) and reverse ISC (red circle). The activation energies of forward and reverse ISC are 0.04 eV and 0.10 eV respectively. (**b**) The proposed energy potential surfaces for *o*-3CzIPN.

In the case of 5CzBN, the forward ISC process does not show any temperature dependence (**Fig. 4-1c**). As for 4CzIPN, the 5CzBN molecule can form a ^{CR}HLCT since it has two pairs of linearly connected Cz units (*18*). In addition, 5CzBN can exhibit rotation of the Cz units in the 2,6-positions (**Fig. 4-10a**) that leads to changes in the electronic structure. My calculations indicate that the excitation character of the 5CzBN T_2 state ($^{CR,3}HLCT_2$) is comparable to that of the 4CzBN T_1 state (**Fig. 4-10b and Fig. 4-10c**). Thus, 4CzBN (**Fig. 4-11a**) can be taken as the relevant partial molecular structure of 5CzBN. The T_1 state energy of 4CzBN (2.80 eV) being lower than that of the 5CzBN S_1 state (2.95 eV) (**Fig. 4-11b**), this rationalizes the reasons why the ISC process in 5CzBN is temperature independent and k_{ISC} (2.5×10^8 s^{-1}) is substantially (four times) larger than that of 4CzIPN (0.7×10^8 s^{-1}). In addition, E_A^{RISC} (0.13 eV) is smaller than $\Delta E_{S1\text{-}T1}$ (0.17 eV) and close to the energy gap between the 4CzBN T_1 and the 5CzBN S_1 (0.15 eV). In fact, the TAS contour map of 5CzBN clearly shows the presence of two types of CT states (^{3}HLCT and ^{CR,3}HLCT) (*ref 18* and **Fig. 4-10d**), indicating that the triplet population in 5CzBN partly involves the $^{CR,3}HLCT_2$ state that has an electronic structure similar to that of 4CzBN during both forward and reverse ISC. I also note (see

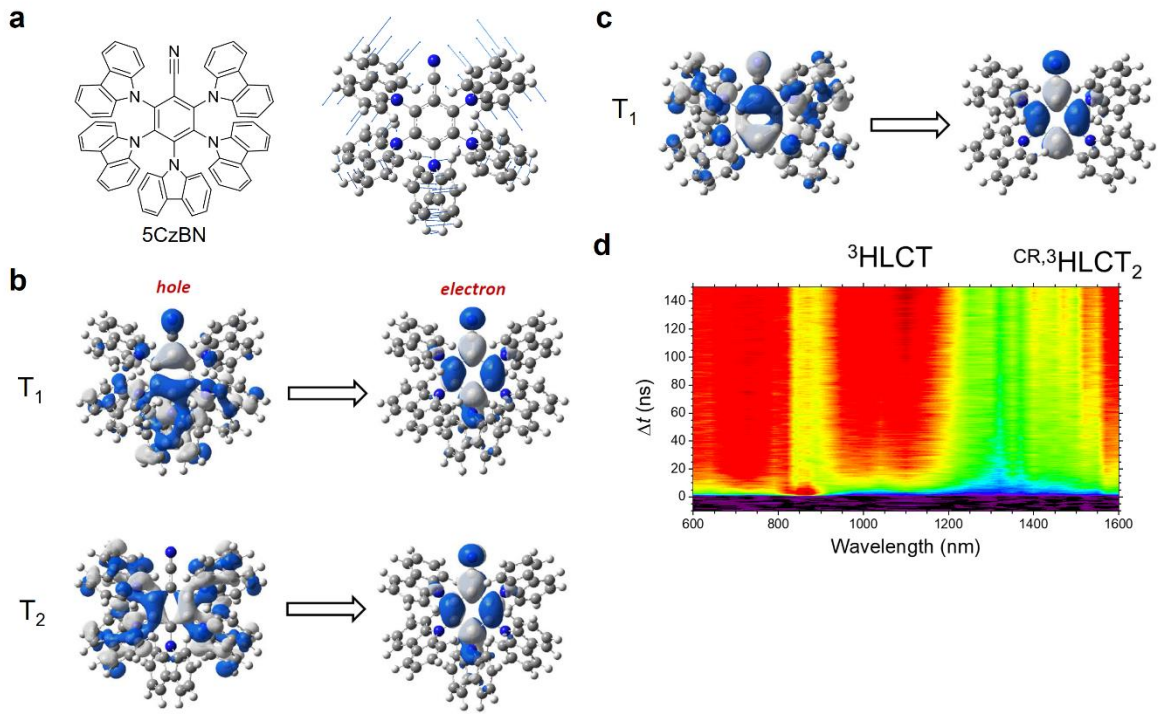

Figure 4-10 (**a**) Molecular structure and vibration mode of 5CzBN. (**b, c**) Molecular orbitals of T_1 and T_2 states in 5CzBN (**b**) and T_1 state in 4CzBN (**c**). (**d**) Contour maps of TAS results for 5CzBN.

Fig. 4-11b) that, although the energy of the $^{CR,3}HLCT_2$ in 5CzBN produces a high k_{ISC}, the uphill energy gap (0.15 eV) that must be overcome when going from $^{CR,3}HLCT_2$ to $^1CT_1$ strongly decelerates the reverse ISC rate; this is in contrast to the downhill (−0.04 eV) conversion from $^3HLCT_2$ to $^1CT_1$ in 4CzIPN. Thus, in 4CzIPN, the final step of the reverse ISC process helps to accelerate the overall rate of the reverse ISC.

Finally, I consider a molecule in which the energy gap from $^1CT_1$ to the closest higher-order triplet state with a different type of excitation character is much larger than the thermal energy, such as 9,10-diphenyl-anthracene (*36*–*38*). In this case, both ISC processes should exhibit very small rate

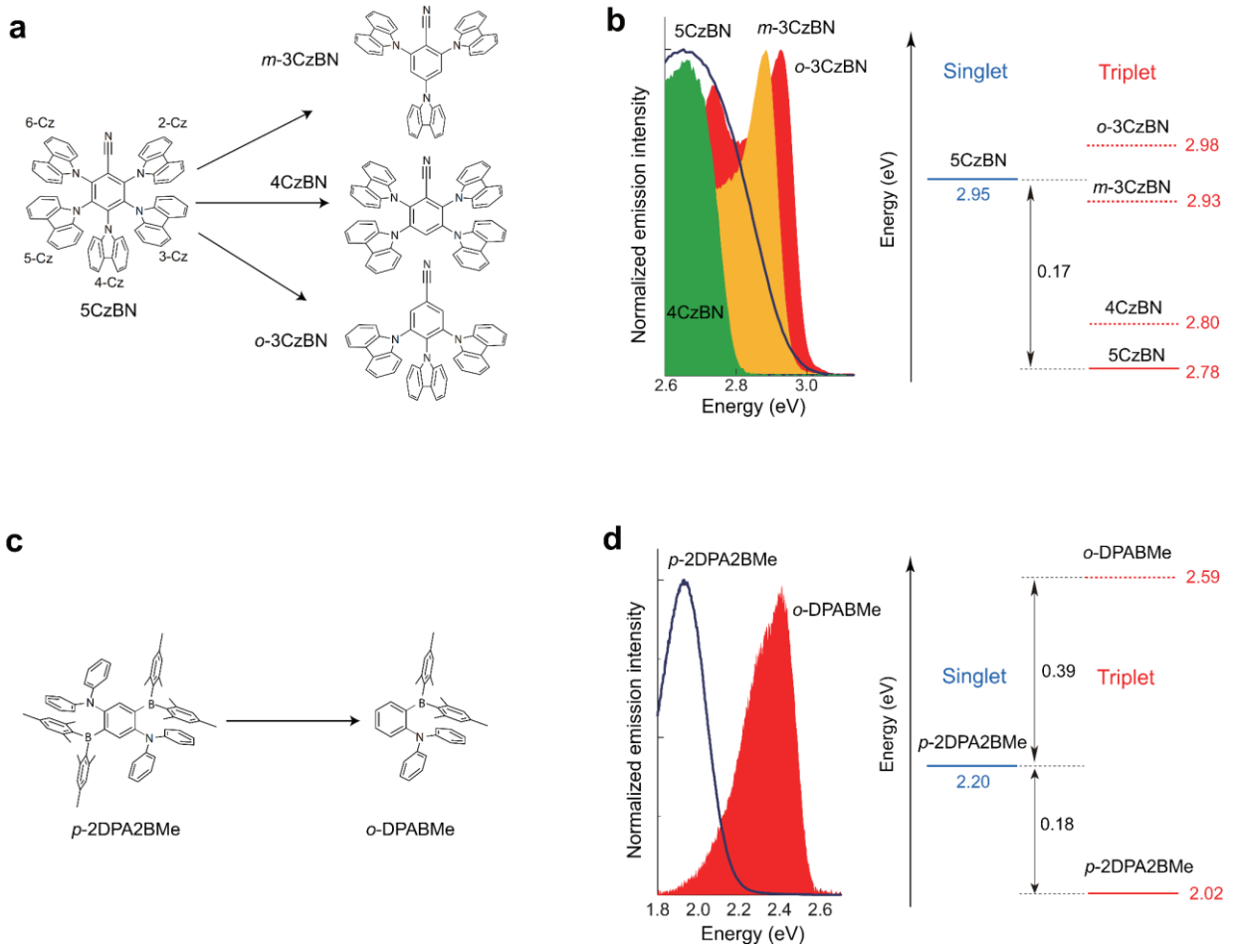

Figure 4-11 (**a**) Complete and partial molecular structures of 5CzBN. (**b**) Phosphorescence spectra of 4CzBN, *m*-3CzBN, and *o*-3CzBN and fluorescence spectrum of 5CzBN in toluene (10^{-5} mol L^{-1}) (left) along with the energy diagram of 5CzBN (right). The solid arrows indicate the spin-flip route for forward and reverse ISC in 5CzBN. (**c**) Complete and partial molecular structures of *p*-2DPA2BMe. (**d**) Phosphorescence spectrum of *o*-DPABMe and fluorescence spectrum of *p*-2DPA2BMe in toluene (10^{-5} mol L^{-1}) (left) along with the energy diagram of *p*-2DPA2BMe (right).

constants based on our proposed mechanism. To assess the photophysical properties in a model compound with such an energy-level structure, the *p*-2DPA2BMe molecule was designed and synthesized (**Fig. 4-11c**). In this molecule, the CR states can form because of the presence of a linearly connected donor (or acceptor) pair, and I evaluate the presence of an upper CT state originating from the partial structure corresponding to *o*-DPABMe. In contrast to the earlier case, the absorption spectrum of *p*-2DPA2BMe does not contain any features corresponding to the absorption of the *o*-DPABMe partial structure (**Fig. 4-12a**), indicating no apparent contribution from the electronic structure of *o*-DPABMe to that of *p*-2DPA2BMe. This can be understood based on the large energy gap (0.39 eV) between the S_1 state (2.20 eV) of *p*-2DPA2BMe and the T_1 state (2.59 eV) of *o*-DPABMe, as shown in **Fig. 4-11d**. Since no intermediate states for spin-flip are accessible at room temperature, the spin-flip processes in *p*-2DPA2BMe should be very slow. Indeed, *p*-2DPA2BMe exhibits a small k_{ISC} of 8.0×10^6 s^{-1} and only an intense prompt fluorescence with a high PLQY of 80%. Even at 77 K, phosphorescence from *p*-2DPA2BMe could not be detected, further confirming that the T_1-state population of *p*-2DPA2BMe is very small under photo-excitation at room temperature. Thus, both forward and reverse ISC processes in *p*-2DPA2BMe are strongly limited.

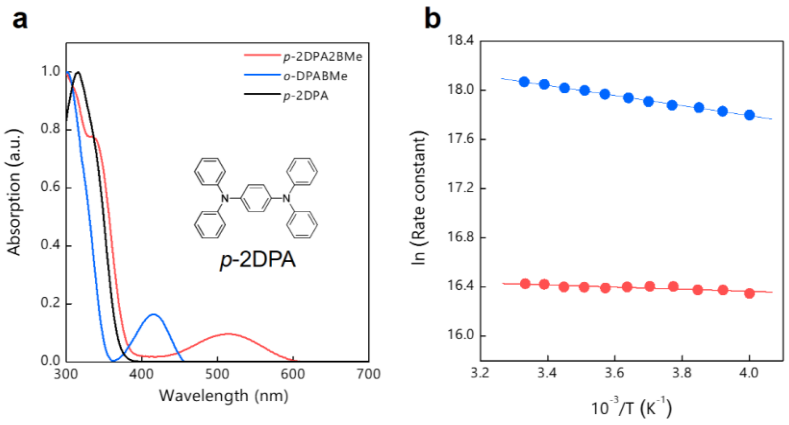

Figure 4-12 (**a**) Absorption spectra of *p*-2DPA2BMe (red line), *o*-DPABMe (blue line), and *p*-2DPA (black line), which is one of the possibilities for the absorption band around 350 nm in toluene. Obviously, *p*-2DPA2BMe has no absorption band originating from a partial molecule, *i.e.*, *o*-DPABMe, indicating that, in the ground state, there is no contribution from an electronic structure similar to that of a partial molecular structure. (**b**) Arrhenius plot of forward ISC: 4CzIPN (blue circle) and *p*-2DPA2BMe (red circle).

4-3. Conclusion

The experimental and theoretical results on a wide range of multi-D-A CT-type molecules, lead the conclusion that a higher-lying triplet excited-state that corresponds to the electronic structure of a partial molecular structure acts as a critical intermediate excited-state in the case of efficient spin-flip processes. Thus, the energy of these intermediate triplet excited-states *vs.* the S_1 and T_1 energies is the key to controlling not only k_{ISC} but also k_{RISC} in such CT-type molecular systems. Since the presence of a clear E_A^{ISC} (10 meV) was observed even in the solid state (**Fig. 4-13**), which can be explained by our proposed mechanism, a proper choice of matrix polarity is important to gain maximum TADF performance.

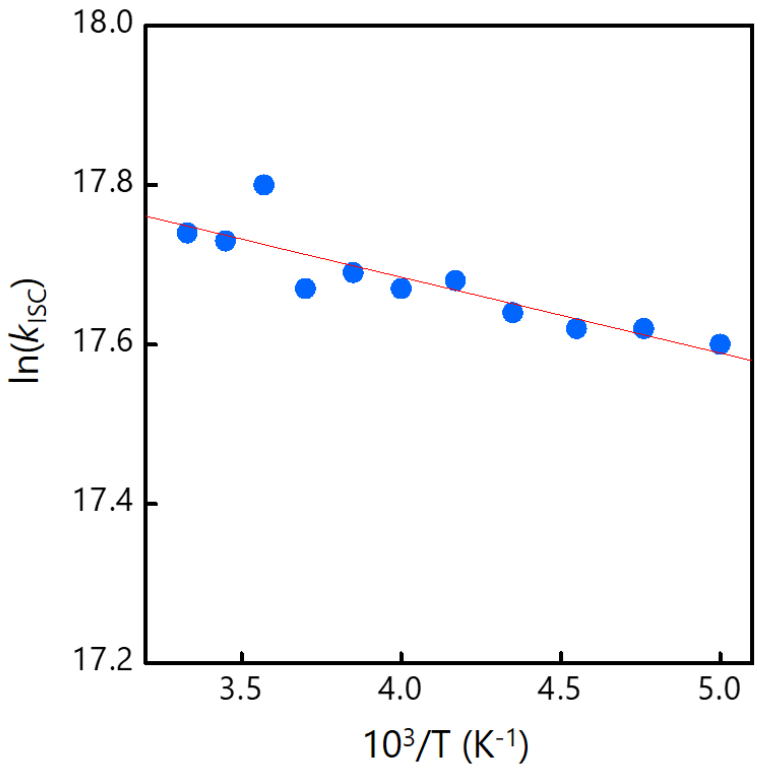

Figure 4-13 Temperature dependence of the k_{ISC} of 4CzIPN in 3,3-di(9H-carbazol-9-yl)biphenyl (mCBP) solid-state host matrix. The solid lines in each figure are fitting results based on Arrhenius equation. The concentration of the 4CzIPN was fixed at 10 wt%.

My work directly connects the evolution of the excited-state character caused by molecular vibrations to the spin-conversion processes. The mechanism proposed here does not contradict the promotion of the ISC process by nonadiabatic coupling between ^{3}CT and ^{3}LE (*14-20*) but rather acts as an important complement to that model. Thus, our work provides the research community with a comprehensive understanding of the spin-flip processes in purely organic multi-D-A CT-type molecules. Importantly, it has demonstrated that the combination of CT states with a different nature and with contribution from partial molecular structures, can lead to the appearance of a dense triplet manifold, which facilitates the spin-conversion processes. Since the electronic structures and the energy levels of the generated CT states are easily changed by the substitution position and the number of substituent units even in the CT state formed by the combination of the identical donor and acceptor units, 'hetero' multi-donor-acceptor-type molecular systems having multiple types of substituents are promising because they can contribute to the control of the formation of multiple CT states. I expect that this understanding will therefore enable the molecular design of novel efficient TADF emitters on the basis of a judicious choice of full *vs*. partial molecular structures.

4-4. Materials and Methods

4-4-1. Measurement of photoluminescence properties

Solutions were prepared by dissolving the purified molecules in toluene solvent. Absolute PLQY of the solutions was measured before and after the bubbling of pure argon gas to estimate prompt PLQY and total PLQY, respectively, using an absolute PL quantum yield measurement system (C11347-01, Hamamatsu Photonics) with an excitation wavelength of 340 nm. The temperature dependence of both τ_p and τ_d was measured using a fluorescence lifetime measurement system (C11367-03 Quantaurus-Tau, Hamamatsu Photonics) and liquid nitrogen cryostat (CoolSpek Cs-0296, UNISOKU Co.). Ground state UV–vis absorption spectra and steady-state PL spectra were recorded on UV–vis (Perkin-Elmer Lambda 950-PKA) and photoluminescence (FluoroMax-4, Horiba Jobin

Yvon)) spectrophotometers. Phosphorescence spectra in solution at 77 K were recorded on a Hamamatsu Photonics multichannel analyzer (PMA-12).

4-4-2. TAS measurements

Nanosecond-TAS measurements were conducted using an apparatus developed in-house (*39*). For the measurements, I used the third harmonic of the fundamental light (1,064 nm) from a Nd^{3+}:YAG laser (wavelength: 355 nm; FWHM pulse: <150 ps; repetition: 10 Hz) as the pump light and a xenon flash lamp as the probe light. The response time was ~1 ns. The irradiated intensity of the pump laser was set to 0.7 to 1.1 mJ/cm^2 depending on the samples. To avoid (possible) irradiation damage by the pump light, I used home-made sample flow cells that enable the measurement of fresh samples after sufficient nitrogen bubbling to avoid triplet deactivation by oxygen. All measurements were carried out at 295 K.

4-4-2. Computational details

The initial ground-state geometries of the molecules were optimized with the long-range corrected functional ωB97XD (with the default range-separation parameter ω of 0.2 bohr^{-1}) and the 6-31G(d,p) basis set (*30*). Then, the "gap" tuning procedure was performed to obtain the optimal ω values for these geometries; the geometries were then reoptimized using the new ω values. This procedure was iterated until the change in ω became < 10^{-3} Bohr^{-1}. The vibrational frequencies of the optimized ground-state geometries were analyzed to ensure that all positive frequencies were obtained. The Tamm-Dancoff approximation (TDA) in the framework of TD-DFT was employed to study the excited-state properties; all the excited-state properties of the molecules were examined at the TDA tuned-ωB97XD/6-31G(d,p) level combined with the polarizable continuum model (PCM; solvent: toluene). NTO analyses were also performed to examine the nature of the excited-states (*40*). All quantum-chemical calculations were performed with the Gaussian 09 Rev D01 program (*41*). In addition, the SOC were estimated by employing the Breit-Pauli spin-orbit Hamiltonian with an effective charge approximation implemented in the PySOC code (*42*).

4-4-3. Synthesis and characterization

4CzIPN, *m*-2CzIPN, 5CzBN, *o*-3CzBN, *m*-3CzBN and *o*-DPABMe were synthesized according to the literature (*4,25,43,44*).

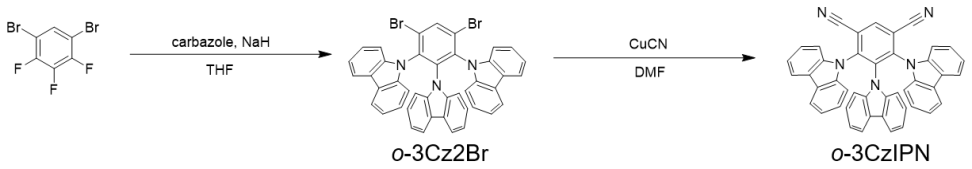

1) 1,5-dibromo-2,3,4-tri(9H-carbazol-9-yl)benzene (*o*-3Cz2Br)

First, carbazole (2.3 g, 13.8 mmol) was added to a dispersion of sodium hydride (60% in mineral oil 0.55 g, 13.8 mmol) in anhydrous THF (40 ml) at 0 °C. After stirring for 30 min, 1,5-dibromo-2,3,4-trifluorobenzene (1.0 g, 3.45 mmol) was added to the mixed solution under argon atmosphere. The reaction mixture was stirred at room temperature overnight. The reaction mixture was quenched with water and the precipitate was filtered and washed with water and methanol. The obtained solid was further washed by acetone. Then we used *o*-3Cz2Br without further purification.

2) 4,5,6-tri(9H-carbazol-9-yl)isophthalonitrile (*o*-3CzIPN)

To a solution of o-3Cz2Br (0.8 g) in DMF (10 ml) was added copper (I) cyanide (0.21g, 2.4 mmol). The solution was refluxed overnight. The reaction mixture was cooled to room temperature and poured into a 10% solution of NaOH. The organic layer was extracted using dicloromethane and washed with water, brine and dried over anhydrous Na_2SO_4, filtered and concentrated in *vacuo*. The crude product was purified by column chromatography on silica gel (toluene) and then reprecipitated from toluene and methanol to produce *o*-3CzIPN as yellow powder (total; 0.41 g 0.66 mmol, 19%).
^{1}H NMR: (500 MHz, acetone-d_6): δ (ppm) = 9.15 (s, 1H), 7.82 (m, 4H), 7.50 (m, 4H), 7.37 (d, J = 7.5 Hz, 2H), 7.29 (d, J = 8.2 Hz, 2H), 7.08 (m, 8H), 6.76 (t, J = 7.9 Hz, 2H), 7.44 (t, J = 8.4 Hz, 2H)
^{13}C NMR: (125 MHz, $CDCl_3$): δ (ppm) = 144.14, 138.28, 137.56, 137.02, 125.62, 124.62, 124.35, 123.72, 121.70, 120.77, 120.29, 119.50, 115.31, 114.09, 110.04, 109.38
MS (FD-MS): m/z 625.13 $[M+H]^+$, (623.21 calcd for $C_{44}H_{25}N_5$)
Elemental analysis: calcd. for $C_{44}H_{25}N_5$: C, 84.73; H, 4.04; N, 11.23; found: C, 84.69; H, 3.99; N, 11.29.

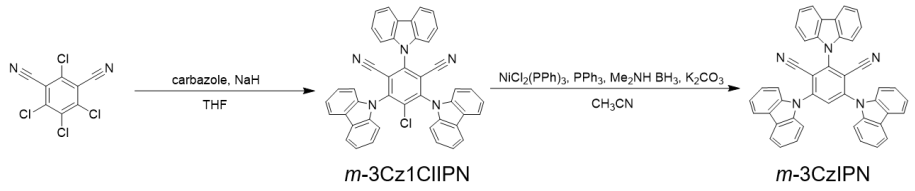

3) 3-chloro-2,4,6-tri(9H-carbazol-9-yl)isophthalonitrile (*m*-3Cz1ClIPN)

First, carbazole (2.8 g, 16.9 mmol) was added to a dispersion of sodium hydride (60% in mineral oil 0.68 g, 16.9 mmol) in anhydrous THF (60 ml) at 0 °C. After stirring for 30 min, tetrachloroisophthalonitrile (1.5 g, 5.64 mmol) was added to the mixed solution under argon atmosphere. The reaction mixture was stirred at room temperature overnight. The reaction mixture was quenched with water and the precipitate was filtered and washed with water and methanol. The obtained solid was purified by column chromatography on silica gel (toluene) and then reprecipitated from toluene/methanol to produce *m*-3Cz1ClIPN as yellow powder (2.75 g, 4.18 mmol, 74%).

^{1}H NMR: (500 MHz, acetone-d_6): δ (ppm) = 8.29 (m, 6H), 7.78 (d, J = 8.2 Hz, 2H), 7.68 (d, J = 8.3 Hz, 4H), 7.57 (m, 6H), 7.42 (m, 6H)

^{13}C NMR: (125 MHz, $CDCl_3$): δ (ppm) = 145.07, 144.23, 139.72, 139.23, 137.04, 126.93, 126.90, 124.79, 124.61, 122.44, 122.18, 121.32, 121.23, 117.62, 110.69, 109.48, 109.29

MS (FD-MS): m/z 658.12 $[M+H]^+$, (657.17 calcd for $C_{44}H_{24}ClN_5$)

4) 2,4,6-tri(9H-carbazol-9-yl)isophthalonitrile (*m*-3CzIPN)

A mixture of *m*-3Cz1ClIPN (0.5 g, 0.76 mmol), bis(triphenylphosphine)nickel(II) dichloride (14.9 mg, 0.023 mmol), triphenylphosphine (5.98 mg, 0.023 mmol), 98% borane– dimethylamine complex (50 mg, 0.84 mmol) and potassium carbonate (0.12 g, 0.84 mmol) in 5 ml of acetonitrile was heated and stirred at 40 °C overnight. After cooling, the mixture was filtered through Celite. The organic layer was separated, and the aqueous layer was extracted with the chloroform. The mixture was concentrated in *vacuo*. The crude product was purified by column chromatography on silica gel (toluene:hexane, 4:1 v/v) to give *m*-3CzIPN (190 mg, 0.30 mmol, 40%).

^{1}H NMR: (500 MHz, acetone-d_6): δ (ppm) = 8.69 (s, 1H), 8.31 (d, J = 7.8 Hz, 4H), 8.25 (d, J = 7.7 Hz, 4H), 7.82 (m, 6H), 7.61 (t, J = 8.3 Hz, 2H), 7.55 (t, J = 8.4 Hz, 4H), 7.42 (m, 6H)

^{13}C NMR: (125 MHz, $CDCl_3$): δ (ppm) = 148.12, 147.10, 140.06, 139.52, 128.02, 126.92, 126.88, 124.93, 124.81, 122.50, 122.21, 121.32, 121.09, 112.43, 111.71, 109.87, 109.35

MS (MALDI-TOF MS): m/z 624.14 $[M+H]^+$, (623.21 calcd for $C_{44}H_{25}N_5$)

Elemental analysis: calcd. for $C_{44}H_{25}N_5$: C, 84.73; H, 4.04; N, 11.23; found: C, 84.69; H, 4.00; N, 11.28.

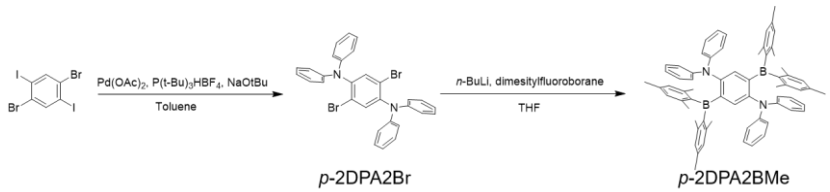

5) 2,5-dibromo-N^1,N^1,N^4,N^4-tetraphenyl-1,4-benzenediamine (*p*-2DPA2Br)

A mixture of 1,4-dibromo-2,5-diiodobenzene (3.0 g, 6.15 mmol), diphenylamine (2.1 g, 12.3 mmol), palladium(II) acetate (0.14 g, 0.615 mmol), tri-tert-butylphosphonium tetrafluoroborate (0.36 g, 1.23 mmol) and sodium tert-butoxide (2.36 g, 24.6 mmol) in 60 ml of toluene was heated and stirred at 100 °C overnight. After cooling, the mixture was filtered through Celite. The organic layer

was separated, and the aqueous layer was extracted with the dichloromethane. The mixture was concentrated in *vacuo*. The crude product was purified by column chromatography on silica gel (dichloromethane:hexane, 1:6 v/v) to give *p*-2DPA2Br (1.03 g, 1.81 mmol, 29%).

^{1}H NMR: (500 MHz, acetone-d_6): δ (ppm) = 7.56 (s, 2H), 7.31 (t, J = 8.0 Hz, 8H), 7.03 (m, 12H)

^{13}C NMR: (125 MHz, $CDCl_3$): δ (ppm) = 146.64, 143.96, 135.99, 129.27, 122.68, 122.60, 122.38

MS (FD-MS): m/z 571.07 $[M+H]^+$, (570.33 calcd for $C_{30}H_{22}Br_2N_2$)

6) 2,5-bis(dimesitylboranyl)- N^1,N^1,N^4,N^4-tetraphenyl-1,4-benzenediamine (*p*-2DPA2BMe)

To a solution of p-2DPABr (0.50 g, 0.88 mmol) in THF at −78 °C was added dropwise n-BuLi in hexane (1.6 M, 1.21 ml, 1.94 mmol). The mixture was stirred for 30 min at -78 °C. Dimesitylboron fluoride (0.52 g, 1.94 mmol) was added to this solution and stirred at 0 °C overnight. After reaction, water was added to the solution and the organic layer was extracted by dichloromethane. The mixture was concentrated in *vacuo*. The crude product was purified by column chromatography on silica gel (dichloromethane:hexane, 1:5 v/v) to give *p*-2DPA2BMe (0.07 g, 0.07 mmol, 8.8%).

^{1}H NMR: (500 MHz, $CDCl_3$): δ (ppm) = 6.99 (m, 10H), 6.81 (t, J = 7.3 Hz, 4H), 6.55 (d, J = 7.6 Hz, 8H), 6.52 (s, 8H), 2.14 (s, 12H), 1.74 (s, 24H)

^{13}C NMR: (125 MHz, $CDCl_3$): δ (ppm) = 149.43, 149.24, 142.46, 140.41, 138.24, 137.95, 128.33, 128.05, 124.40, 121.90, 23.43, 21.11

MS (FD-MS): m/z 909.70 $[M+H]^+$, (908.89 calcd for $C_{66}H_{66}B_2N_2$)

Elemental analysis: calcd. for $C_{66}H_{66}B_2N_2$: C, 87.22; H, 7.32; N, 3.08; found: C, 87.51; H, 7.28; N, 3.11.

References

1. Lamola, A. A., Hammond, G. S., Mechanisms of Photochemical Reactions in Solution. XXXIII. Intersystem Crossing Efficiencies. *J. Chem. Phys.*, **43**, 2129-2135 (1965).
2. Baldo, M. A., O'Brien, D. F., You, Y., Shoustikov, A., Sibley, S., Thompson, M. E., Forrest, S. R., Highly efficient phosphorescent emission from organic electroluminescent devices. *Nature*, **395**, 151-154 (1998).
3. Reineke, S., Lindner, F., Schwartz, G., Seidler, N., Walzer, K., Lüssem, B., Leo, K., White organic light-emitting diodes with fluorescent tube efficiency. *Nature*, **459**, 234-238 (2009).
4. Uoyama, H., Goushi, K., Shizu, K., Nomura, H., Adachi, C., Highly efficient organic light-emitting diodes from delayed fluorescence. *Nature*, **492**, 234-238 (2012).

5. Hirata, S., Recent Advances in Materials with Room-Temperature Phosphorescence: Photophysics for Triplet Exciton Stabilization. *Adv. Opt. Mater.*, **5**, 1700116 (2017).

6. Zhao, Q., Huang, C., Li, F., Phosphorescent heavy-metal complexes for bioimaging. *Chem. Soc. Rev.*, **40**, 2508-2524 (2011).

7. Xiong, X., Song, F., Wang, J., Zhang, Y., Xue, Y., Sun, L., Jiang, N., Gao, P., Tian, L., Peng, X., Thermally Activated Delayed Fluorescence of Fluorescein Derivative for Time-Resolved and Confocal Fluorescence Imaging. *J. Am. Chem. Soc.*, **136**, 9590-9597 (2014).

8. Maeda, K., Henbest, K. B., Cintolesi, F., Kuprov, I., Rodgers, C. T., Liddell, P. A., Gust, D., Timmel, C. R., Hore, P. J., Chemical compass model of avian magnetoreception. *Nature*, **453**, 387-390 (2008).

9. Baluschev, S., Miteva, T., Yakutkin, V., Nelles, G., Yasuda, A., Wegner, G., Up-Conversion Fluorescence: Noncoherent Excitation by Sunlight. *Phys. Rev. Lett.*, **97**, 143903 (2006).

10. Castano, P., Mroz, P., Hamblim, M. R., Photodynamic therapy and anti-tumourimmunity. *Nat. Rev. Cancer*, **6**, 535-545 (2006).

11. Smith, M. B., Michi, J., Singlet Fission. *Chem. Rev.*, **110**, 6891-6936 (2010).

12. Wong, M. Y., Zysman-Colman, E., Purely Organic Thermally Activated Delayed Fluorescence Materials for Organic Light-Emitting Diodes. *Adv. Mater.*, **29**, 1605444 (2017).

13. El-Sayed, M. A., The Radiationless Processes Involving Change of Multiplicity in the Diazenes. *J. Chem. Phys.*, **36**, 573-574 (1962).

14. Chen, X. K., Zhang, S. F., Fan, J. X., Ren, A. M., Nature of Highly Efficient Thermally Activated Delayed Fluorescence in Organic Light-Emitting Diode Emitters: Nonadiabatic Effect between Excited states. *J. Phys. Chem. C*, **119**, 9728-9733 (2015).

15. Gibson, J., Monkman, A. P., Penfold, T. J., The Importance of Vibronic Coupling for Efficient Reverse Intersystem Crossing in Thermally Activated Delayed Fluorescence Molecules. *ChemPhysChem*, **17**, 2956-2961 (2016).

16. Dias, F. B., Santos, J., Graves, D. R., Data, P., Nobuyasu, R. S., Fox, M. A., Batsanov, A. S., Palmeira, T., Berberan-Santos, M. N., Bryce, M. R., Monkman, A. P., The Role of Local Triplet Excited states and D-A Relative Orientation in Thermally Activated Delayed Fluorescence: Photophysics and Devices. *Adv. Sci.*, **3**,1600080 (2016).

17. Marian, C. M., Mechanism of the Triplet-to-Singlet Upconversion in the Assistant Dopant ACRXTN. *J. Phys. Chem. C*, **120**, 3715-3721 (2016).

18. Hosokai, T., Matsuzaki, H., Nakanotani, H., Tokumaru, K., Tsutsui, T., Furube, A., Nasu, K., Nomura, H., Yahiro, M., Adachi, C., Evidence and Mechanism of Efficient Thermally Activated Delayed Fluorescence Promoted by Delocalized Excited states. *Sci. Adv.*, **3**, e1603282 (2017).

19. Gibson, J., Penfold, T. J., Nonadiabatic coupling reduces the activation energy in thermally activated delayed fluorescence. *Phys. Chem. Chem. Phys.*, **19**, 8248-8434 (2017).

20. Etherington, M. K., Gibson, J., Higginbotham, H. F., Penfold, T. J., Monkman, A. P., Revealing the spin–vibronic coupling mechanism of thermally activated delayed fluorescence. *Nat. Commun.*, **7**, 13680 (2016).

21. Hayashi, H., Nagakura, S., The E.S.R. and phosphorescence spectra of some dicyanobenzene complexes with methyl-substituted benzenes. *Mol. Phys.*, **19**, 45-53 (1970).

22. Olivier, Y., Yurash, B., Muccioli, L., D'Avino, G., Mikhnenko, O., Sancho-García, J. C., Adachi, C., Nguyen, T.-Q., Beljonne, D., Nature of the singlet and triplet excitations mediating thermally activated delayed fluorescence. *Phys. Rev. Materials*, **1**, 075602 (2017).

23. Kobayashi, T., Niwa, A., Takaki, K., Haseyama, S., Nagase, T., Goushi, K., Adachi, C., Naito, H., Contributions of a Higher Triplet Excited State to the Emission Properties of a Thermally Activated Delayed-Fluorescence Emitter. *Phys. Rev. Appl.*, **7**, 034002 (2017).

24. Evans, E. W., Olivier, Y., Puttisong, Y., Myers, W. K., Hele, T. J. H., Menke, S. M., Thomas, T. H., Credgington, D., Beljonne, D., Friend, R. H., Greenham, N. C., Vibrationally Assisted Intersystem Crossing in Benchmark Thermally Activated Delayed Fluorescence Molecules. *J. Phys. Chem. Lett.*, **9**, 4053-4058 (2018).

25. Cho, Y. J., Jeon, S. K., Lee, J. Y., Molecular Engineering of High Efficiency and Long Lifetime Blue Thermally Activated Delayed Fluorescent Emitters for Vacuum and Solution Processed Organic Light-Emitting Diodes. *Adv. Optical. Mater.*, **4**, 688-693 (2016).

26. Noda, H., Nakanotani, H., Adachi, C., Excited state engineering for efficient reverse intersystem crossing. *Sci. Adv.*, **4**, eaao6910 (2018).

27. Yanai, N., Kimizuka, N., New Triplet Sensitization Routes for Photon Upconversion: Thermally Activated Delayed Fluorescence Molecules, Inorganic Nanocrystals, and Singlet-to-Triplet Absorption. *Acc. Chem. Res.*, **10**, 2487-2495 (2017).

28. Mopsik, F. I., Dielectric Properties of Slightly Polar Organic Liquids as a Function of Pressure, Volume, and Temperature. *J. Chem. Phys.*, **50**, 2559-2569 (1969).

29. Samanta, P. K., Kim, D., Coropceanu, V., Brédas, J. L., Up-Conversion Intersystem Crossing Rates in Organic Emitters for Thermally Activated Delayed Fluorescence: Impact of the Nature of Singlet vs Triplet Excited states. *J. Am. Chem. Soc.*, **139**, 4042-4051 (2017).

30. Körzdörfer, T., Brédas, J. L., Organic Electronic Materials: Recent Advances in the DFT Description of the Ground and Excited States Using Tuned Range-Separated Hybrid Functionals. *ACC. Chem. Res.*, **47**, 3284-3291 (2014).

31. Yamamoto, M., Tsuji, Y., Tuchida, A., Near-infrared charge resonance band of intramolecular carbazole dimer radical cations studied by nanosecond laser photolysis. *Chem. Phys. Lett.*, **154**, 559-562 (1989).

32. Kaafarani, B. R., Risko, C., El-Assaad, T. H., El-Ballouli, A. O., Marder, S. R., Barlow, S., Mixed-Valence Cations of Di(carbazol-9-yl) Biphenyl, Tetrahydropyrene, and Pyrene Derivatives. *J. Phys. Chem. C*, **120**, 3156-3166 (2016).

33. Lawetz, V., Orlandi, G., Siebrand, W., Theory of Intersystem Crossing in Aromatic Hydrocarbons. *J. Chem. Phys.*, **56**, 4058−4072 (1972).

34. Robinson, G. W., Frosch, R. P., Electronic Excitation Transfer and Relaxation. *J. Chem. Phys.*, **38**, 1187−1203 (1963).

35. Wang, L., Nan, G., Yang, X., Peng, Q., Li, Q., Shuai, Z., Computational methods for design of organic materials with high charge mobility. *Chem. Soc. Rev.*, **39**, 423-434 (2010).

36. Bowen, E. J., Sahu, J., The Effect of Temperature on Fluorescence of Solutions. *J. Phys. Chem.*, **63**, 4-7 (1959).

37. Bennett, R. G., McCartin, P. J., Radiationless Deactivation of the Fluorescent State of Substituted Anthracenes. *J. Chem. Phys.*, **44**, 1966 (1969).

38. Katoh, R., Suzuki, K., Furube, A., Kotani, M., Tokumaru, K., Fluorescence Quantum Yield of Aromatic Hydrocarbon Crystals. *J. Phys. Chem. C*, **113**, 2961-2965 (2009).

39. Yoshihara, T., Murai, M., Tamaki, Y., Furube, A., Katoh, R., Trace analysis by transient absorption spectroscopy: estimation of the solubility of C60 in polar solvents. *Chem. Phys. Lett.*, **394**, 161–164 (2004).

40. Martin, R. L., Natural transition orbitals. *J. Chem. Phys.*, **118**, 4775-4777 (2003).

41. M. J. Frisch, G. W. Trucks, H. B. Schlegel, G. E. Scuseria, M. A. Robb, J. R. Cheeseman, G. Scalmani, V. Barone, B. Mennucci, G. A. Petersson, H. Nakatsuji, M. Caricato, X. Li, H. P. Hratchian, A. F. Izmaylov, J. Bloino, G. Zheng, J. L. Sonnenberg, M. Hada, M. Ehara, K. Toyota, R. Fukuda, J. Hasegawa, M. Ishida, T. Nakajima, Y. Honda, O. Kitao, H. Nakai, T. Vreven, J. A. Montgomery, Jr., J. E. Peralta, F. Ogliaro, M. Bearpark, J. J. Heyd, E. Brothers, K. N. Kudin, V. N. Staroverov, R. Kobayashi, J. Normand, K. Raghavachari, A. Rendell, J. C. Burant, S. S. Iyengar, J. Tomasi, M. Cossi, N. Rega, J. M. Millam, M. Klene, J. E. Knox, J. B. Cross, V. Bakken, C. Adamo, J. Jaramillo, R. Gomperts, R. E. Stratmann, O. Yazyev, A. J. Austin, R. Cammi, C. Pomelli, J. W. Ochterski, R. L. Martin, K. Morokuma, V. G. Zakrzewski, G. A. Voth, P. Salvador, J. J. Dannenberg, S. Dapprich, A. D. Daniels, Ö. Farkas, J. B. Foresman, J. V. Ortiz, J. Cioslowski, and D. J. Fox, Gaussian 09 (Gaussian, Inc., Wallingford CT, 2009)

42. Gao, X., Bai, S., Fazzi, D., Niehaus, T., Barbatti, M., Evaluation of Spin-Orbit Couplings with Linear-Response Time-Dependent Density Functional Methods. *J. Chem. Theory Comput.*, **13**, 515-524 (2017).

43. Cho, Y. J., Yook, K. S., Lee, J. Y., Cool and warm hybrid white organic light-emitting diode with blue delayed fluorescent emitter both as blue emitter and triplet host. *Sci. Rep.*, **5**, 7859 (2015).

44. Lee, Y. H., Park, S., Oh, J., Shin, J. W., Jung, J., Yoo, S., Lee, M. H., Rigidity-Induced Delayed Fluorescence by Ortho Donor-Appended Triarylboron Compounds: Record-High Efficiency in Pure Blue Fluorescent Organic Light-Emitting Diodes. *ACS Appl. Mater. Interfaces*, **9**, 24035-24042 (2017).

Chapter 5

Summary

In this thesis, I aimed to comprehensively understand spin-flip processes in purely organic aromatic CT type molecules and proposed a design guideline for TADF molecules to control both forward and reverse ISC processes.

In **chapter 2**, in order to investigate the effect of ^{3}LE states on the spin-flip processes in TADF molecules, I proposed new molecular design based on the introduction of hetero donors. Introduction of the D_2 units with a lower ^{3}LE level led to decrease $|\Delta E_{3LE\text{-}3CT}|$, producing the mixing between the ^{3}CT and ^{3}LE states and the spin-flip process becomes more allowed transition than the original D-A system having no hetero donors. Thus, the excited-state alignment of ^{1}CT, ^{3}CT and ^{3}LE levels can be achieved by the introduction of the D_2 units in an original D-A system while maintaining the ^{1}CT and ^{3}CT energy levels to those of the original D-A system. In particular, the designed molecule of 3Cz2DPhCzBN possesses a k_{RISC} (7.2×10^5 s^{-1}) that is more than 3 times larger than that of the template molecule of 5CzBN. In addition, thanks to the acceleration of the k_{RISC}, *i.e.*, short triplet lifetime, 3Cz2DPhCzBN-OLED showed higher EQE, suppression of efficiency rolloff and improvement of operational stability than that of 5CzBN. Thus, the proposed molecular design rule is useful for boosting OLED performance and will promote expansion of TADF molecules into future lighting and display applications.

In **chapter 3**, I designed TADF molecules showing highly efficient luminescence with remarkably slow k_{RISC} to demonstrate that controlling a spin-flip process based on the energy alignment between ^{1}CT, ^{3}CT and ^{3}LE states could expand another possibility. On the basis of the findings in **chapter 2**, I selected the appropriate D group and A group with a high LE level, leading to the stabilization of the CT state and the large $|\Delta E_{3LE\text{-}3CT}|$. Although *p*-2Cz2BMe showed the extremely slow k_{RISC} (2.1×10^3 s^{-1}), high PLQY of 89±2% and the reverse ISC efficiency close to 100% were realized. From these experimental results, I concluded that $|\Delta E_{3LE\text{-}3CT}|$ plays an important role in controlling the spin-flip rate and a rigid molecular structure allows a long DF lifetime without sacrificing PLQY. Thus, my molecular design provides a new path to obtain a long-lived emission lifetime with high PLQY in purely aromatic compounds exhibiting TADF.

In **chapter 4**, I investigated the spin-flip process of CzCN derivatives, which cannot be explained by the mechanism considering the LE state. As a result, in CT type molecules showing an efficient spin-flip process, I confirmed that a higher-lying triplet state acts as an intermediate state for the spin-flip process. From the theoretical and experimental aspects, I also clarified that the electronic structure of the higher-lying triplet state shows good agreement with that of the triplet state of the partial structure of the parent molecule. Thus, not only the ^{3}LE state but also the higher-lying triplet state with different electronic structure plays a critical role for the spin-flip process. The proposed mechanism is applicable to a wide variety of multi-D-A CT-type molecules that could not be explained by mechanisms of a higher LE level, and comprehensive understanding of the spin-flip process in purely organic CT-type molecules was obtained.

I summarize the spin-flip rate of the previously designed molecules in **Fig. 5-1**. Although some of designed molecules show almost same $\Delta E_{S1\text{-}T1}$ of 0.1-0.2 eV highlighted as yellow color, we can recognize a wide range of k_{RISC} depending on the molecular structures. For example, *p*-2DPA2BMe shows no TADF activity, while 3Cz2DPhCzBN has high k_{RISC}. Based on these results, to control the spin-flip process precisely, three factors are required; i) the energy splitting between S_1 and T_1, *i.e.*, $\Delta E_{S1\text{-}T1}$, ii) the energy gap between ^{3}CT and ^{3}LE, *i.e.*, $|\Delta E_{3LE\text{-}3CT}|$, iii) the energy level alignment between the higher-lying triplet state originated from a partial molecular structure and the parent S_1 and T_1 states.

Finally, I summarize the perspectives of advanced TADF molecules. First, based on the molecular design rules of i) and ii), we should accurately understand the electron-donating ability of a D unit and electron-withdrawing ability of an A unit and the LE state energy of both D and A groups. In addition, the basic strategy; introduction of D and A units and twisting between D and A units to separate HOMO and LUMO are required to control the spatial overlap between the HOMO and LUMO, *i.e.*, $\Delta E_{S1\text{-}T1}$ and $|\Delta E_{3LE\text{-}3CT}|$. As well as fundamental photophysical properties of D and A groups, quantum chemical calculation also helps us to design your desirable materials.

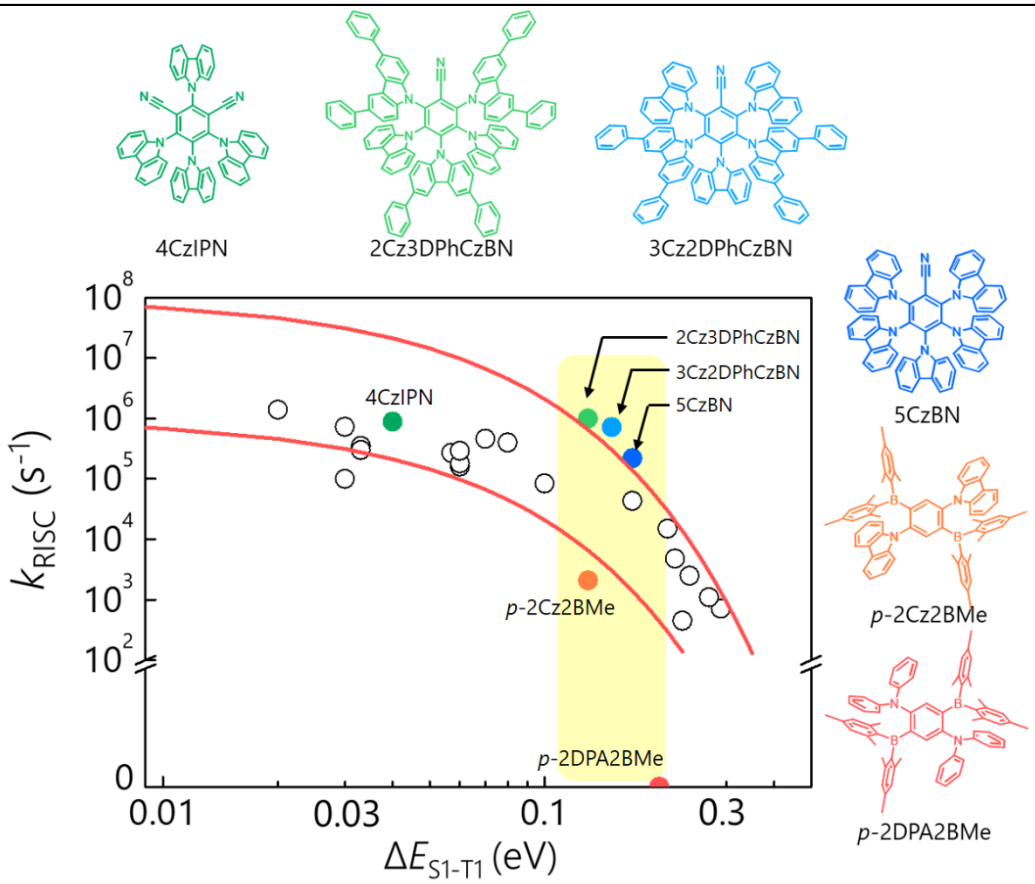

Figure 5-1 Relationship between k_{RISC} and ΔE_{S1-T1} in our designed TADF molecules.

Next, in order to control the molecular design rule of iii), we should consider not only ^{1}CT and ^{3}CT states but also higher-lying excited-states. To develop CT-type TADF molecules with an efficient spin-flip process ($k_{RISC} > 10^6$ s^{-1}), the formation of multiple CT states is required. Even in the CT state formed with single D and A pair, electronic structures and energy levels of the generated CT state are easily changed by the substituted position and the number of substituted units. From this viewpoint, I conclude that it is important to satisfy the molecular design rules of i) and ii) by selecting D and A units and form a large number of CT states with different electronic characters by using a plurality of D groups and A groups. To realize this molecular design, "hetero donor" molecular design strategy is one of the promising way because this can contribute to control the LE state energy levels and the formation of the multiple CT states. In a similar manner, I note that the formation of multiple excited-states by utilizing the stereoisomer is also useful (*1*).

I wish my molecular design will broaden the further possibility of TADF materials which

can be applied to OLEDs and triplet excitons based devices.

Reference

1. dos Santos, P. L., Ward, J. S., Congrave, D. G., Batsanov, A. S., Eng, J., Stacey, J. E., Penfold, T. J., Monkman, A. P., Bryce, M. R., *Adv. Sci.*, **5**, 1700989 (2018).

Publication lists

Original papers

1) **Hiroki Noda**, Ryota Kabe, Chihaya Adachi, *Chem. Lett.*, **45**, 1463-1466 (2016).
"Blue thermally activated delayed fluorescence molecules composed of acridan and cyanobenzene units"
*Not described in this thesis.

2) **Hiroki Noda**, Hajime Nakanotani, Chihaya Adachi, *Sci. Adv.*, **4**, eaao6910 (2018).
"Excited state engineering for efficient reverse intersystem crossing"

3) **Hiroki Noda**, Hajime Nakanotani, Chihaya Adachi, *Chem. Lett.* (DOI:10.1246/cl.180813).
"Highly efficient thermally activated delayed fluorescence with slow reverse intersystem crossing"

4) **Hiroki Noda**, Xian-Kai Chen, Hajime Nakanotani, Takuya Hosokai, Momoka Miyajima, Naoto Notsuka, Jean-Luc Brédas, Chihaya Adachi (submitted to *Nat. Mater.*).
"Critical role of intermediate electronic states for spin-flip processes in multi-donor-acceptor charge-transfer-type purely organic molecules"

Joint papers

1) Katsuyuki Shizu, **Hiroki Noda**, Hiroyuki Tanaka, Masatsugu Taneda, Motoyuki Uejima, Tohru Sato, Kazuyoshi Tanaka, Hironori Kaji, Chihaya Adachi, *J. Phys. Chem. C*, **119** 26283-26289 (2015).
"Highly Efficient Blue Electroluminescence Using Delayed-Fluorescence Emitters with Large Overlap Density between Luminescent and Ground States"

2) Takuya Hosokai, **Hiroki Noda**, Hajime Nakanotani, Takanori Niwata, Hiroyuki Matsuzaki, Chihaya Adachi, *J. Photon. Energy*, **8**, 032102 (2018).
"Solvent-dependent investigation of carbazole benzonitrile derivatives: Does the ^{3}LE-^{1}CT energy gap facilitate TADF?"

Acknowledgements

The studies in this thesis were carried out at Adachi laboratory, Department of Chemistry and Biochemistry, Graduate School of Kyushu University from 2014-2019.

I am deeply grateful to Professor Chihaya Adachi for supervising this thesis, excellent experimental environment, helpful discussion, and exact comments and advice for all of my works. I am also deeply grateful to Professor Takuma Yasuda and Professor Ken Onda for co-supervising of this thesis. I would also like to thank Associate Professor Hajime Nakanotani, Assistant Professor Kenichi Goushi, Assistant Professor Ryota Kabe, Assistant Professor Masashi Mamada. They also gave me useful advice and helped in preparing of my papers. Especially, I would like to express my gratitude to Associate Professor Hajime Nakanotani for discussion on spin-flip processes and help in preparing this thesis.

I would like to acknowledge Professor Jean-Luc Bredas and Dr. XianKai Chen (Georgia Institute of Technology) for quantum chemical calculation in chapter 4 and Dr. Takuya Hosokai (National Institute of Advanced Industrial Science and Technology) for discussion and TAS measurements.

I would like to thank the former member of Adachi laboratory, Dr. Hiroyuki Tanaka, Assistant Professor Katsuyuki Shizu, Associate Professor Masatsugu Taneda, Dr. Munetomo Inoue and Dr. Kou Yoshida whose comments and advices have helped me. I also acknowledge all the members of Adachi laboratory and all persons who I met through my works for their supports not only for my work but also my daily life. I would like to thank the Japan Society for the Promotion of Science for a grant and a fellowship that made it possible to complete this study. Finally, I would also like to express my gratitude to my family for their moral support and warm encouragements.

January, 2019 *Hiroki Noda*